
*C*ontents

Articles

A Radiometer for Precision Coherent Radiation Measurements	Douglas B. Thomas and Edward F. Zalewski	327
ITS-90 Density of Water Formulation for Volumetric Standards Calibration	Frank E. Jones and Georgia L. Harris	335
Heat Capacity and Thermodynamic Properties of Poly(chlorotrifluoroethylene) from 2.5 to 620 K	Shu-Sing Chang and James J. Weeks	341
Precipitation and Solubility of Calcium Hydrogenurate Hexahydrate	V. Babić-Ivančić, H. Füredi-Milhofer, N. Brničević, and M. Marković	365
The NIST SPIDER, A Robot Crane	James Albus, Roger Bostelman, and Nicholas Dagalakis	373

Conference Reports

Workshop on Characterizing Diamond Films	Albert Feldman, Charles P. Beetz, Michael Drory, and Sandor Holly	387
--	--	-----

News Briefs

GENERAL DEVELOPMENTS	393
New Ways Needed to Test Fire Safety of Wiring New "Freeware" Computes Signal Frequencies Report Offers Guidelines on FTAM Implications	
Do Irregular Pipes Affect Flow Measurements? Insulation Program Covers Entire Building Envelope Twenty-Seven Grants Announced for ATP's 2nd Year Program Announced for Precision Casting of Alloys 3-D Computer Model Predicts Oil Fire "Footprints"	394
Wood Products Industry Defines Federal Role Ninety Companies Vie for 1992 Baldrige Award Gunpowder "Fingerprints" Could Catch Crooks Quicker Two Mixtures Could Replace Banned Refrigerant	395
Comment Period Extended for Proposed CASE Program How Fast Does a Leak Leak? Ask NIST U.S., Italy Agree on Gas Pressure Standard Government Inventions Now Available for Licensing	396
NIST Trains USDA Quality Control Officials NIST Staff Demonstrates 800-Fold Improvement in Optical Fiber Current Sensor NIST Developments Provide Impetus for Two Start-Ups	397
Laser-Ablated High-Critical-Temperature Superconductor Films Studied Longest Range Scanning Tunneling Microscope Developed Workshop on Supercritical Fluid Extraction Held at NIST Automated Calibration System for Air Flow-Rate Calibrations	398
Magnetic Engineering of Thin Films NIST Holds Workshop on NVLAP Ionizing Radiation Personnel Dosimetry Program Gravity Attracts Federal Lab Consortium FLC Award	399
NIST Project Earns NASA Committee's Top Priority Patent on the "Sharpest" STM Tip Ever Expert System Modules for Chemical Process Industries Released NIST Expands Microelectronics Packaging Efforts	400
Animation Program for Process Simulation First Station for Cold Neutron Inelastic Scattering Operational at NIST NIST SQL Test Suite, Version 3.0, Released	401
Professional/Trade Organization Laboratory Accreditation/Designation Programs NIST Hosts and Sponsors 5th National Consortium for Specialized Secondary Schools of Mathematics, Science, and Technology Update of the NIST/EPA/NIH Mass Spectral Database Completed Update of Chemical Kinetics Database Released	402

New ITS-90 Based Data for Thermocouples Council on Ionizing Radiation Measurements and Standards (CIRMS) Is Established Initial Observations of IML-1 Triglycine Sulfate Crystal NIST Establishes Memorandum of Understanding (MOU) with the Communications Security Establishment of Canada	403
New Publication Describes Reference Model (RM) for Software Engineering Environment (SEE) Frameworks	404
STANDARD REFERENCE MATERIALS Standard Reference Materials 2534 and 2535 – Ellipsometric Parameters, Δ and Ψ , and Derived Thicknesses and Refractive Index for a Silicon Dioxide Layer on Silicon Standard Reference Material 473 – Optical Microscope Linewidth Measurement Standard Standard Reference Material 968a – Fat-Soluble Vitamins in Human Serum	404
STANDARD REFERENCE DATA 1992 SRD Products Catalog Available Eight Refrigerants Added to REFPROP Database New Gas Phase Infrared Database Available for PCs NIST Binary Images of Handwritten Segmented Characters	405
<i>Calendar</i>	407

A Radiometer for Precision Coherent Radiation Measurements

Volume 97

Number 3

May-June 1992

**Douglas B. Thomas and
Edward F. Zalewski¹**

National Institute of Standards
and Technology,
Gaithersburg, MD 20899

A radiometer has been designed for precision coherent radiation measurements and tested for long-term repeatability at wavelengths of 488 and 633 nm. The radiometer consists of a *pn* silicon photodiode maintained in a nitrogen atmosphere with a quartz window designed to eliminate interference problems. Ratio measurements between the radiometer and an absolute type detector were made over a period of 215 d. At 0.5 mW, the standard deviations were 0.008% and 0.009% at 488 and 633 nm, respectively. The maximum deviations from the mean were 0.016% and 0.015% at the respective

wavelengths. Measurements were also made on the radiometer with respect to angular and spatial uniformity and linearity. The high precision, simplicity, and portability of the radiometer suggest it for use as a transfer standard for radiometric measurements.

Key words: coherent radiation; laser; photocurrent; radiometer; silicon photodiode.

Accepted: April 28, 1992

1. Introduction

The need for high accuracy radiometric measurements has manifested itself in recent years in military and industrial research and in manufacturing applications. The recent development of high accuracy cryogenic radiometers [1] has made it possible to realize accuracies approaching the 0.01% level. In order to utilize this capability in routine laboratory measurements, a transfer standard is needed with the precision and long-term stability that is better than most portable radiometers currently available for coherent radiation measurements. We have constructed and tested a nitrogen filled, wedged-window radiometer (WWR) for coherent radiation measurements

using a Hamamatsu² SI337-1010B *pn* silicon photodiode of the type found to be most stable by Korde and Geist [2]. The superior stability and uniformity of this photodiode is a considerable improvement over previous generation photodiodes. The wedged window is designed to eliminate interference problems associated with detector windows of conventional design. The WWR is a device which can be used in conjunction with an appropriate absolute radiometer for fundamental calibration and does not in itself serve as an absolute device. Radiometers such as the QED-200 discussed below and

¹ Present address: Hughes Danbury Optical Systems, 100 Wooster Heights Rd., Danbury, CT 06810-7589.

² Certain commercial equipment, instruments, or materials are identified in this paper to specify adequately the experimental procedure. Such identification does not imply recommendation or endorsement by the National Institute of Standards and Technology, nor does it imply that the materials or equipment identified are necessarily the best available for the purpose.

cryogenically operated electrical substitution devices serve as the fundamental radiometric base with the WWR serving as a useful secondary radiometer for routine usage for some laboratory circumstances. A preliminary version of this paper was reported at an SPIE conference in 1989 [3].

2. Description of the Experiment

The basic components of the WWR include a windowless Hamamatsu S1337-1010B *pn* type silicon photodiode, a quartz wedged-window, a heavy wall black plastic tube, and stop-cock valves. The photodiode was specially selected by the manufacturer for spatial uniformity of response and high shunt resistance. Figure 1 is a cross-section drawing of the WWR. The wedged window and the photodiode are sealed at opposite ends of the plastic tube with epoxy cement. The hermetically sealed tube is filled with nitrogen of 99.998% minimum purity (including water vapor) as certified by the manufacturer and then sealed by using two glass stop-cock valves. The nitrogen gas pressure in the tube is slightly above $1.0 \times 10^5 \text{ N/m}^2$ (1 atm). The window is 25 mm in diameter with a minimum thickness of 3 mm and a wedge angle of 3.8° . Also, the end of the plastic tube to which the window is sealed is cut at an angle of 3.8° (ϕ in Fig. 1). The window is sealed to the end of the plastic tube at an orientation such that the wedged plane of the window is rotated 90° from the 3.8° cut on the plastic tube and thus neither plane of the window is parallel to the surface of the photodiode. This minimizes interference effects.

Measurements on the wedged-window radiometer were made using the laser-based detector

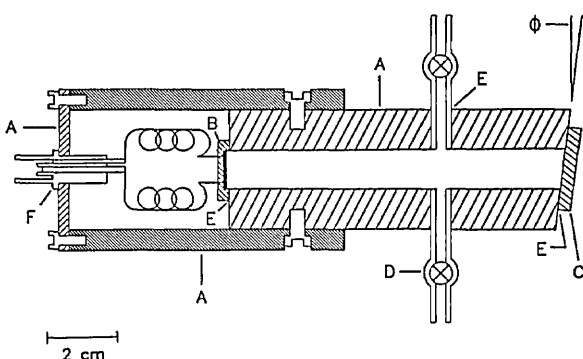


Fig. 1. Cross-section of the wedged window radiometer. A, black opaque plastic; B, silicon photodiode; C, quartz wedged window; D, glass stop-cock valve; E, epoxy cement; F, BNC connector; ϕ , 3.8° angle (not to scale).

calibration facility shown in Fig. 2. This facility has been carefully constructed to allow for precision measurements on detectors using laser sources. The detectors were tested in a light-tight enclosure and a number of precision positioning devices were used to insure the repeatability of the settings necessary to carry out the high precision measurements discussed here.

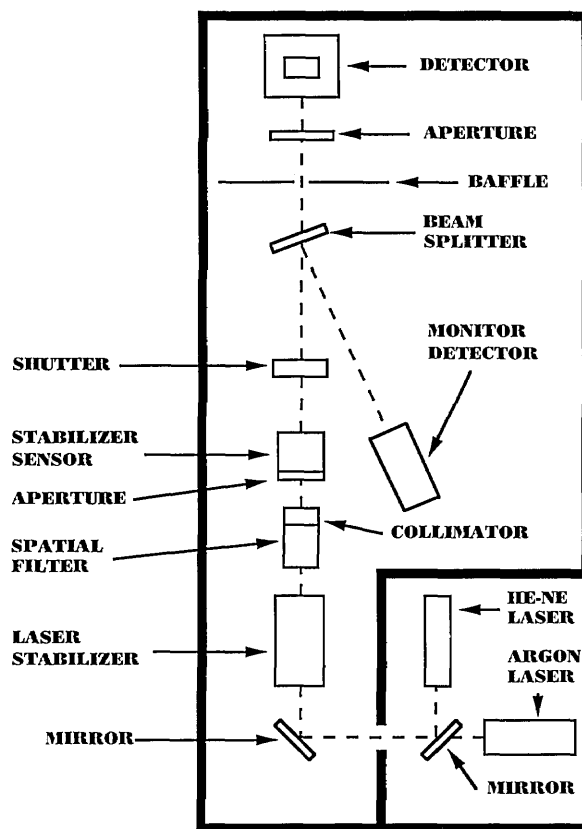


Fig. 2. Laser-based detector calibration facility for 488 and 633 nm wavelengths.

The basic components in the facility include two laser sources—a 9 mW helium-neon laser and a 15 mW air-cooled argon laser, a laser power stabilizer, spatial filter, beam expanding telescope, wedged beam-splitter, and a monitor detector. The monitor detector was a Hamamatsu *pn* silicon photodiode similar to the type used in the WWR. Although the monitor diode was not protected by a window, its short-term ($< 2 \text{ h}$) stability when measured against a QED-200 absolute radiometer (see below) was $< 0.02\%$. All measurements of the QED-200 and WWR photocurrents were made as ratios to the monitor detector photocurrent. Thus, the monitor detector needed to be stable only during the short

period when the respective photocurrents were measured. If the monitor detector had exhibited significant instabilities during the photocurrent measurements, these instabilities would have been reflected in the final WWR and QED ratios.

The laser power stabilizer was a Cambridge Research and Instrument Company model LS-100, a commercial version of the stabilizer described by Fowler et al. [4]. The internal beam-splitter/sensor of the stabilizer was disconnected and replaced by an external beam-splitter/sensor located after the spatial filter and beam expanding telescope. In this way, the stabilizer controls only that portion of the laser beam selected by the pinhole in the spatial filter. Since the laser beam was vertically polarized, the best stabilizer performance was obtained by mounting the beam-splitter/sensor so that the radiation is reflected horizontally. The variable internal reference voltage of the stabilizer was used to vary laser power over the 0.08 to 0.9 mW range.

The spatial filter was used in a somewhat unconventional way. The filter's objective lens focused the laser beam slightly in front of the 25 μm pinhole so as to overfill the pinhole. This produces a circular diffraction pattern on the iris diaphragm just before the beam-splitter. The iris diaphragm was adjusted to intercept the first dark ring in the diffraction pattern and a collimator was used to collimate the diffracted laser beam. This eliminated most of the diffraction and scattering effects arising from the iris diaphragm. The final iris diaphragm, in front of the detector comparator position, was adjusted to eliminate any scattered light arising from the first iris diaphragm and the two beam-splitters. The maximum peak-to-peak variation of the laser power over a 30 min period was 0.05%. This was determined using a 100% quantum efficient Model QED-200 absolute radiometer.

An absolute standard generally used in the laser based detector calibration facility is the commercially available 100% quantum efficient detector device [5], Model QED-200, manufactured by the United Detector Technology Company. Ratio measurements between the WWR and a QED-200 were made to determine the long-term stability of the WWR and to determine the linearity of both devices. The acquisition of data was facilitated by the use of a computer programmed to measure the QED or WWR photocurrent followed by a measurement of the monitor detector photocurrent. The ratio of the two photocurrents was then computed. A measurement sequence consisted of 150 repeats of the measurement of the ratio over a

time span of about 30 min. The 150 measurement sequence of the QED to monitor detector ratio was followed immediately by a 150 measurement sequence of the WWR to monitor detector ratio. The ratio of the average of these two measurement sequences represents one data point in the long-term stability discussion in Sec. 4. The integration time for a single photocurrent measurement was 167 ms. All of the long-term stability measurements on the WWR were made (a) at an ambient temperature of $24 \pm 0.5^\circ\text{C}$, (b) with a laser beam diameter of approximately 4 mm, and (c) with the laser beam normal to and centered on the WWR wedged-window.

3. Interference Effects Using Conventional Windows

The magnitude of interference effects which can occur when photodiodes with conventional windows are irradiated with coherent radiation was demonstrated using the laser-based detector calibration facility. A 0.5° quartz wedged-window approximately 10 mm in diameter and 1 mm thick was mounted on an EG&G UV444B silicon photodiode. The window was mounted such that one surface of the window was parallel to the surface of the photodiode with a separation between the two surfaces of approximately 2 mm. The photodiode (with window) was irradiated with a 4 mm diameter laser beam at 633 nm and 0.5 mW while the photocurrent was measured over a period of 17 min. The laser beam was normal to the photodiode surface. The window was then removed and the photocurrent was measured again. Figure 3 shows the relative response of the photodiode with and without the window. The maximum peak-to-peak change in response with the window was 0.95% and without the window was 0.08%. The response data shown in Fig. 3 raises a question concerning the causes of the larger fluctuations in response with the window in place when compared to the fluctuations without the window. Since measurements were made with both the photodiode and the laser in a fixed position, it would seem that the resulting interference pattern would also be fixed and thus produce a relatively constant photodiode response. However, many He-Ne lasers have beam spatial profiles that change slightly in intensity over short periods of time. Also, these lasers can have spectral mode fluctuations over short periods of time. These phenomena can cause changes in an interference pattern and thus produce response changes in the photodiode.

It was also found that the window introduced a spatial nonuniformity. Figure 4 shows the spatial variation in response of the photodiode when the laser beam was moved across the diameter of the photodiode in 0.5 mm increments. With the window, the maximum peak-to-peak change in response was 1.21% and without the window the maximum was 0.14%. This clearly unsatisfactory performance is attributed to an interference effect between the window and the reflective surface of the photodiode. If one surface of the window and the surface of the photodiode are approximately

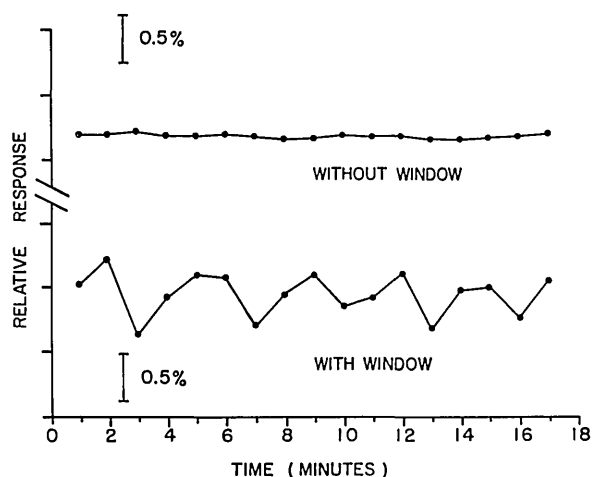


Fig. 3. Relative response of a silicon photodiode with and without a window. A 4 mm diameter laser beam at 633 nm and 0.5 mW was positioned normal to and centered on the photodiode surface. The precision of the measurements is 0.016% (1σ).

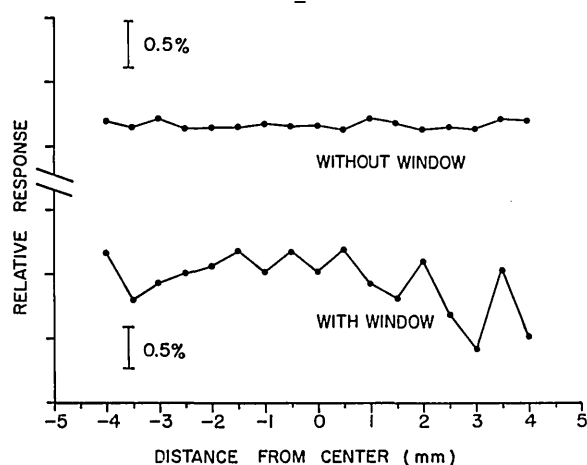


Fig. 4. Relative response of a silicon photodiode with and without a window. A 4 mm diameter laser beam at 633 nm and 0.5 mW was translated across the diameter of the photodiode with the beam normal to the photodiode surface. The precision of the measurements is 0.016% (1σ).

parallel, interference fluctuations (resulting in response fluctuations) can occur. In order to eliminate these effects, the wedged-window radiometer (WWR) discussed above and depicted in Fig. 1 was constructed and tested.

4. Stability of the Wedged Window Radiometer

Measurements of the long-term stability of the WWR were made over a period of 215 d at 633 nm and 40 d at 488 nm. Figure 5 is a plot of the deviations of all WWR to QED measurement-sequence ratios at 0.5 mW from their respective mean at 488 and 633 nm. The maximum deviations from the mean were -0.016% and $+0.015\%$ at the two wavelengths, respectively. Each data point in Fig. 5 represents a ratio of the average of 150 measurements of the WWR photocurrent to the average of 150 measurements of the QED photocurrent. The precision in each ratio value presented in Fig. 5 is the quadrature sum of the standard deviations of the WWR to monitor and QED to monitor ratios. This precision is 0.020%. The long-term repeatability of the WWR to QED ratios, i.e., the standard deviation of the ratio values in Fig. 5, is 0.008% at 488 nm and 0.009% at 633 nm. For power levels above and below 0.5 mW, the WWR and QED ratios deviated from the ratio mean at 0.5 mW by a maximum of $+0.115\%$ and $+0.155\%$ at 488 and 633 nm respectively. A discussion of these larger deviations is presented in Sec. 6.

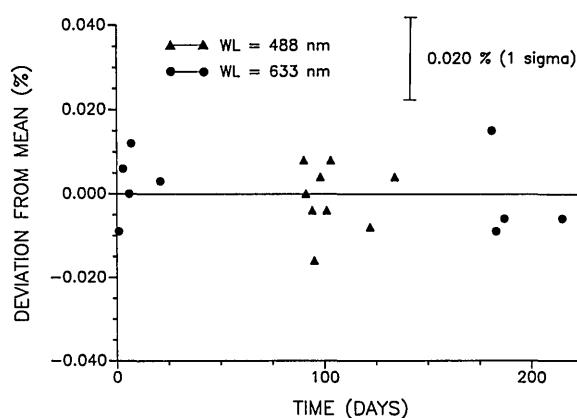


Fig. 5. Deviation of all WWR to QED ratios at 0.5 mW from their respective mean at 488 and 633 nm. Each data point represents the average of a 150 measurement sequence. The standard deviations of the ratios are 0.008% and 0.009% at 488 and 633 nm, respectively. The uncertainty in each ratio value is $\pm 0.020\%$ (1σ) which is the quadrature sum of the standard deviations of the WWR to monitor and QED to monitor ratios.

5. Spatial and Angular Uniformity Measurements

Spatial and angular uniformity measurements were made on the WWR at 0.5 mW at both 488 and 633 nm. The result of the spatial uniformity scan across one diameter of the WWR is plotted in Fig. 6. The maximum deviation of the spatial measurements from the detector center position mean response was 0.034% or about twice the measurement precision of 0.016% (1σ). The angular uniformity measurements are plotted in Fig. 7. The angles listed represent the angular deviations of

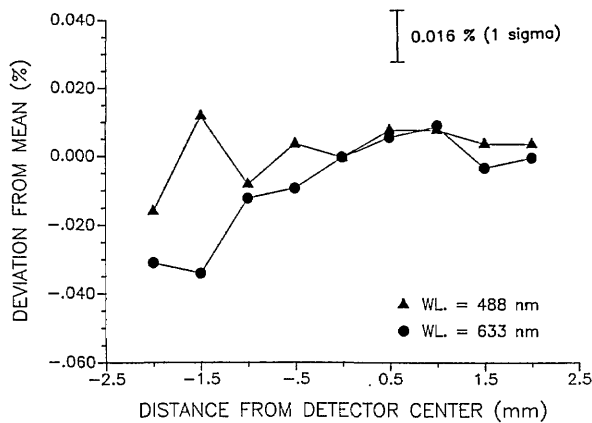


Fig. 6. Spatial uniformity of the WWR showing response deviations from the mean response at the photodiode center. The laser beam (4 mm in diameter and 0.5 mW at both 488 and 633 nm) was translated across the diameter of the WWR photodiode with the beam normal to the photodiode surface. The precision of the measurements is 0.016% (1σ).

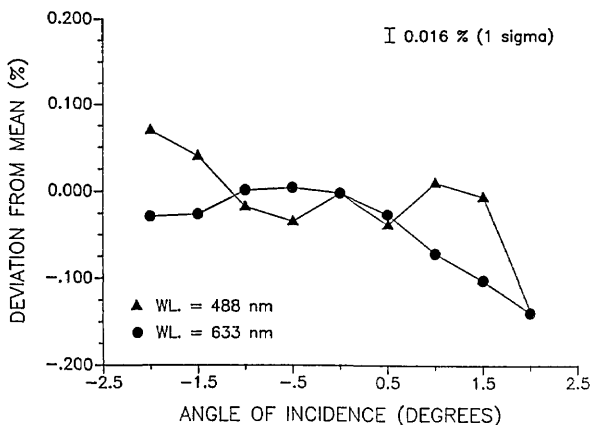


Fig. 7. Angular uniformity of the WWR showing response deviations from the mean response when the laser beam is normal to the photodiode. The angle of incidence of the laser beam on the photodiode was changed in 0.5° increments from a beam position normal to and centered on the photodiode surface. The laser beam was 4 mm in diameter and 0.5 mW at both wavelengths. The precision of the measurements is 0.016% (1σ).

the laser beam from a line normal to the photodiode surface. Within a 2° range, the maximum deviation from the normal response (response with the beam normal to the diode surface) was 0.139%. Both the spatial and angular uniformity measurements were obtained with a 4 mm diameter beam. Thus, the spatial uniformity of the response of WWR is within a distance of ± 1.5 mm from the center of the WWR photodiode. Furthermore, the response of the WWR is constant within 0.060% over an angular displacement of $\pm 1^\circ$.

6. Comparison of the QED and WWR at Different Power Levels

From some of our earlier, less precise experiments with the QED-200, we had an indication that these devices might be nonlinear under reverse voltage bias at power levels above 0.5 mW. In conversations with L. P. Boivin of the National Research Council of Canada and with C. R. Duda of the United Detector Technology Company, we learned that they also observed what appeared to be small nonlinearities under similar measurement conditions. Since the QED-200 is now being applied in many high accuracy radiometric measurements, we have decided to report our limited observations in order to encourage further studies. Kohler, Pello, and Bonhoure report similar nonlinearity for the QED in this study of temperature effects on the device [6].

Measurements were made of QED/monitor ratios and WWR/monitor ratios at various radiant power levels from 0.08 to 0.9 mW. The WWR/monitor ratios over this power range were constant (within the precision of the measurements) while the QED/monitor ratios showed a general increase above 0.5 mW. Figure 8 shows the deviation of the QED/WWR ratios at various radiant power levels from the QED/WWR ratio at 0.5 mW. The figure shows the ratios to be generally increasing at both wavelengths with increasing power. However, between 0.08 and 0.5 mW at 633 nm and between 0.2 and 0.5 mW at 488 nm, the ratios appear to be constant within the limits of the measurement uncertainty. No measurements were made above 0.9 mW since this was the maximum power attainable with the system. It should be noted that the measurements were made with reverse bias voltages on the QED of 30 and 10 V at 633 and 488 nm, respectively.

Although the QED/monitor and WWR/monitor measurements indicated the QED to be nonlinear, we felt it necessary to conduct an experiment to

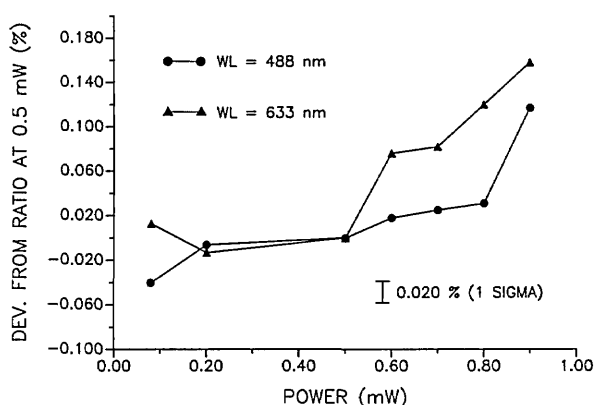


Fig. 8. Deviations of the QED/WWR ratios at various radiant power levels from the QED/WWR ratio at 0.5 mW at both 488 and 633 nm. The uncertainty in each ratio value is $\pm 0.020\%$ (1σ) which is the quadrature sum of the standard deviations of the WWR to monitor and QED to monitor ratios.

show that the nonlinearity could not be attributed to polarization changes in the laser beam at the various power levels.

During the course of the described experiments, the laser power was varied by changing the voltage applied to a birefringent crystal in the laser stabilizer. This causes a change in the polarization of the laser beam and a subsequent change in the amount of power transmitted by the polarizer located in the exit port of the laser stabilizer. If this polarizer was not perfect, the resulting beam polarization may not be 100% linearly polarized as expected. The QED consists of three detectors, two of which are oriented at a 45° angle to the laser beam. The WWR has a window with both surfaces oriented slightly off normal to the laser beam. The differences in the polarization sensitivity of these two devices might account for the differences in their response.

To check the degree of polarization of the laser beam exiting the stabilizer, a prism polarizer was placed in the beam and its vertical-to-horizontal transmission was measured at 633 nm. The detector chosen for the polarization variation measurement was a Hamamatsu S1227-1010B without a window. The uniformity of this detector was measured and found to vary less than 0.1% over the central 6 mm diameter area. It was aligned normal to the laser beam and checked for possible polarization sensitivity by rotating it around the laser beam axis. The variations were within the 0.016% precision of the measurement.

At 633 nm the vertical-to-horizontal polarization ratios of the laser beam were found to change

slightly at different power levels. At 0.08 mW, the ratio was 7,300 to 1; at 0.5 mW, 9,400 to 1; and at 0.9 mW, 10,800 to 1. Thus, there is a change in the polarization of the laser beam, but the horizontal component is never greater than 0.014% of the vertical component of the beam. Therefore, the change in the polarization of the beam cannot account for the power dependent differences between the QED and the WWR.

The Hamamatsu S1227-1010B detector was also used in comparisons with the WWR and the QED at 633 nm and power levels of 0.08 mW, 0.5 mW, and 0.9 mW. The ratios of the WWR to the Hamamatsu detector were constant to within the precision of the measurements for the three power levels. For the QED versus the Hamamatsu detector measurements, an increase of 0.133% was observed for the QED between the 0.5 and 0.9 mW power levels. This value agrees quite well with the increase of 0.155% for the QED versus the WWR as indicated in Fig. 8 at the same power levels.

Since small ambient temperature changes can affect the spectral response of photodiodes, this phenomenon was considered as a possible source of instability in the three types of diodes used in this study. The maximum ambient temperature fluctuations in the measurement facility during one measurement cycle (1 h) was $\pm 0.5^\circ\text{C}$. The ambient temperature of the laboratory was 24°C . Using temperature coefficient data we measured on Hamamatsu S1226-1010B and S1337-1010B photodiodes, the response change in these diodes at 488 and 633 nm is less than $0.01\%/^\circ\text{C}$. Information received from the manufacturer of the QED-200 radiometer lists a temperature coefficient of less than $0.1\%/^\circ\text{C}$ for the diodes in this radiometer. Thus, the effects of temperature on the diodes used in this study are too small to explain the observed nonlinearity of the QED-200 radiometer.

7. Conclusion

Ratio measurements between the WWR and the QED over a period of 40 days at 488 nm show the repeatability (1σ) of the differences between the ratios and their mean to be 0.008%. At 633 nm over a period of 215 d, the repeatability (1σ) of the ratio differences was 0.009%. This repeatability was determined at 0.5 mW. The maximum deviations of the ratios from the mean of all ratios at the respective wavelengths were -0.016% and $+0.015\%$ at 488 and 633 nm respectively. At power levels between 0.08 and 0.9 mW, the response of

the WWR appears to be linear with power. However, the QED appears to exhibit some nonlinear behavior at power levels above 0.5 mW.

Measurements on the spatial and angular uniformity of the WWR at 488 and 633 nm showed that the WWR is uniform to within the $\pm 0.016\%$ measurement precision for translations within ± 1.5 mm from the detector center. This indicates that with a careful selection of photodiodes, good uniformity can be obtained for precision measurement purposes. Also, the WWR exhibited angular uniformity within $\pm 0.060\%$ for angle deviations from the normal up to $\pm 1^\circ$. These measurements indicate that the highest precision is achieved with the WWR when it is calibrated and used with (a) a 6 mm diameter or smaller laser beam, (b) the beam located in the same position on the photodiode surface, and (c) the beam optical axis normal to the photodiode surface. This implies that care must be taken in performing measurements with this device to achieve the precision reported here. This care not only requires selection of the photodiode but the maintenance of a precision optical measurement facility.

Since the WWR is not an absolute radiometer, it must be calibrated using an absolute standard. Such standards include (a) the 100% quantum efficient detector radiometer (QED), (b) a self-calibrated silicon photodiode [6] [8], (c) a cryogenic absolute radiometer [9], (d) a cavity-type electrically calibrated radiometer [10] and (e) an electrically calibrated pyroelectric radiometer (ECPR) [11]. The reported absolute accuracies of these standards range from 0.01% for the cryogenic radiometer to 0.7% for the ECPR.

It should be emphasized that the repeatability of the WWR reported in this paper represents the performance of one specific device in a measurement facility where variables were carefully controlled. If another sample of the device were calibrated and used in a facility where parameters such as temperature, beam size, and beam uniformity vary, the repeatability of measurements made with the device could be significantly different.

The manufacturer of the photodiode used in the WWR reports a "worst-case" temperature coefficient for the diode of 0.2 %/°C as compared to the very small temperature coefficient measured for the device used in the present measurements.

If the size of a beam used to irradiate the WWR varies from one measurement to another, this would affect the measurement repeatability. Using the uniformity values reported in Fig. 6, it can be seen that a beam diameter change from 1.0 to 3.0

mm could result in a "worst-case" response change of 0.035% at 633 nm.

The effects of beam uniformity on the repeatability of the WWR would be similar to the effects discussed for beam size. For example, if the spectral response of the WWR were determined with a laser beam which had a "hot-spot" (a portion of the beam with higher intensity than the average intensity of the beam) in the first quadrant of the beam cross-section and again determined with a "hot-spot" in the third quadrant, the two response values could be different due to diode non-uniformity. If the uniformity values reported in Fig. 6 can be considered as typical, the "worst-case" effect due to beam nonuniformity would be a response change of 0.035% at 633 nm.

Although it is unlikely that all of the above "worst-case" situations would occur during a specific WWR measurement sequence, a quadrature summation of these effects reveals a total possible error of 0.21%, assuming a one degree variation in temperature. Thus, the above analysis shows that special care must be taken to control measurement variables and the temperature coefficient of the specific device must be measured in order to realize the measurement precision capabilities of the WWR.

If the WWR were calibrated to the accuracy attainable using the cryogenic absolute radiometer and if measurement variables are carefully controlled, it is not unreasonable to expect the calibration to have an absolute uncertainty of 0.02% to 0.03%. If this is achievable, the WWR would provide a low-cost, portable and stable radiometer for a variety of radiometric purposes, particularly in circumstance where the ambient air was subject to humidity and temperature variation.

8. References

- [1] J. E. Martin, N. P. Fox, and P. J. Key, A Cryogenic Radiometer for Absolute Radiometric Measurements, *Metrologia* **21**, 147 (1985).
- [2] R. Korde and J. Geist, Quantum Efficiency Stability of Silicon Photodiodes, *Appl. Opt.* **26**, 5284 (1987).
- [3] D. B. Thomas and E. F. Zalewski, A Radiometer for Precision Coherent Radiation Measurements, *SPIE* **1109**, 70 (1989).
- [4] J. B. Fowler, M. A. Lind, and E. F. Zalewski, A Servo Controlled Electro-Optic Modulator for CW Laser Power Stabilization and Control, *Natl. Bur. Stand. (U.S.) Tech. Note* **987**, Washington, DC 20402 (1979).
- [5] E. F. Zalewski and C. R. Duda, Silicon Photodiode Device With 100% External Quantum Efficiency, *Appl. Opt.* **22**, 2867 (1983).

- [6] R. Kohler, P. Pello, and J. Bonhoure, *Appl. Opt.* **29**, 4217 (1990).
- [7] E. F. Zalewski and J. Geist, Silicon Photodiode Absolute Spectral Response Self-Calibration, *Appl. Opt.* **19** (8), 1214 (1980).
- [8] J. Geist, E. F. Zalewski, and A. R. Schaefer, Spectral Response Self-Calibration and Interpolation of Silicon Photodiodes, *Appl. Opt.* **19**, 3795 (1980).
- [9] N. P. Fox, Uses of a Cryogenic Radiometer in Absolute Radiometry, *Proc. Adv. Abs. Radiometry Conf.*, Cambridge, MA, June 1985.
- [10] Gao Zhizhong et al., Realization of the Candela by Electrically Calibrated Radiometers, *Metrologia* **19**, 85-92, (1983).
- [11] W. Doyle, B. McIntosh, and J. Geist, Implementation of a System of Optical Calibration Based on Pyroelectric Radiometry, *Opt. Eng.* **IS**, No. 6, Nov.-Dec. (1976).

About the authors: *Douglas B. Thomas is a physicist in the Radiometric Physics Division in the Center for Radiation Research at NIST. Edward F. Zalewski is a Senior Staff Engineer in the Advanced Developments Laboratory of Hughes Danbury Optical Systems. The National Institute of Standards and Technology is an agency of the Technology Administration, U.S. Department of Commerce.*

ITS-90 Density of Water Formulation for Volumetric Standards Calibration

Volume 97

Number 3

May–June 1992

Frank E. Jones
32 Orchard Way South,
Potomac, MD 20854

and

Georgia L. Harris
National Institute of Standards
and Technology,
Gaithersburg, MD 20899

A new formulation of the density of air-saturated water as a function of temperature on the 1990 International Temperature Scale (ITS-90) is presented. Also, a new equation for calculating isothermal compressibility as a function of temperature on ITS-90 was developed. The equations are to be used to calculate the density of water, in the temperature range 5 to 40 °C on ITS-90, used in the gravimetric determination of the volume of volumetric standards.

Key words: air-saturated water; calibration; density of water; isothermal compressibility; ITS-90; volumetric standards.

Accepted: April 27, 1992

1. Introduction

In the gravimetric determination of the volume (calibration) of volumetric standards, water is used as the calibrating fluid. The volume is calculated from the mass and density of the water. In many quarters, the formulation of Wagenbreth and Blanke [1] is used to calculate the density of water. In this paper, a new formulation of the density of water (based primarily on the work of Kell [2]) as a function of temperature on the 1990 International Temperature Scale is presented.

2. Kell's Formulations

2.1 Density of Water

In 1975, Kell [2] published a new formulation for the density of *air-free* water at a pressure of 101.325 kPa (1 atmosphere) valid from 0 to 150 °C "that is in improved agreement with most data sets." The Kell formulation is

$$\rho \text{ (kg m}^{-3}\text{)} = (999.83952 + 16.945176 t - 7.9870401 \times 10^{-3} t^2 - 46.170461 \times 10^{-6} t^3 + 105.56302 \times 10^{-9} t^4 - 280.54253 \times 10^{-12} t^5) / (1 + 16.897850 \times 10^{-3} t), \quad (1)$$

where t is temperature in °C on the 1968 International Practical Temperature Scale (IPTS-68).

2.2 Isothermal Compressibility

Kell also developed equations for calculation of the isothermal compressibility, κ_T , of air-free water [2]. In the temperature range 0 to 100 °C on IPTS-68, the equation can be expressed as

$$\kappa_T = (50.88496 \times 10^{-8} + 6.163813 \times 10^{-9} t + 1.459187 \times 10^{-11} t^2 + 20.08438 \times 10^{-14} t^3 - 58.47727 \times 10^{-17} t^4 + 410.4110 \times 10^{-20} t^5) / (1 + 19.67348 \times 10^{-3} t), \quad (2)$$

where κ_T is isothermal compressibility in (kPa)⁻¹.

3. New Formulations

3.1 Density of Air-Free Water

In the present work, the Kell calculated values of ρ were fitted over the temperature range 5 to 40 °C on the new 1990 International Temperature Scale (ITS-90) [3] to an equation quartic in temperature. The equation is

$$\rho \text{ (kg m}^{-3}\text{)} = 999.85308 + 6.32693 \times 10^{-2} t - 8.523829 \times 10^{-3} t^2 + 6.943248 \times 10^{-5} t^3 - 3.821216 \times 10^{-7} t^4. \quad (3)$$

In contrast with the Kell equation, a term in t^5 is not necessary due at least in part to the fact that the 0 to 4 °C region, in which ρ increases with increasing temperature, has been excluded. Equation (3) applies to *air-free* water.

Values of the density of air-free water were calculated for temperatures (ITS-90, t_{90}) between 4.999 and 39.990 °C using Eq. (3) and compared with corresponding Kell values. The estimate of the standard deviation (SD) of the difference was 0.00034 kg m⁻³. The ratio of SD to the mean value of density was 3.4×10^{-7} , which is negligible.

3.2 Conversion of IPTS-68 to ITS-90

A very simple equation relating ITS-90 temperature, t_{90} , to IPTS-68 temperature, t_{68} , has been used in the present work to generate values of t_{90} for the development of Eq. (3). The equation for the temperature range 0 to 40 °C is

$$t_{90} = 0.0002 + 0.99975 t_{68}. \quad (4a)$$

In the temperature range 0 to 100 °C the equation is

$$t_{90} = 0.0005 + 0.9997333 t_{68}. \quad (4b)$$

3.3 Change in Density of Water with Air Saturation

Bignell [4] measured the change in the density of water with air saturation for 80 points in the range of 4 to 20 °C. He fitted the points to develop the equation

$$\Delta\rho = -0.004612 + 0.000106 t, \quad (5)$$

where $\Delta\rho$ is in kg m⁻³. There is no need to adjust for temperature scale. Bignell concluded that “there is probably not much need to extend the work to higher temperatures because the effect diminishes and the accuracy of density metrology at these temperatures would not warrant a more accurately known correction.”

3.4 Density of Air-Saturated Water on ITS-90

Equation (5) was added to Eq. (3) to produce an equation to be used to calculate the density, ρ_{as} , of *air-saturated* water in the temperature range 5 to 40 °C on ITS-90:

$$\rho_{as} = 999.84847 + 6.337563 \times 10^{-2} t - 8.523829 \times 10^{-3} t^2 + 6.943248 \times 10^{-5} t^3 - 3.821216 \times 10^{-7} t^4 \quad (6)$$

The uncertainty in the density of air-saturated water for an uncertainty in temperature of 1 °C is approximately 210 ppm or 0.21 kg m⁻³ at 20 °C.

3.5 Isothermal Compressibility

The thermal compressibility data used by Kell have been fitted against temperature on ITS-90 for the temperature range 5 to 40 °C. The resulting equation is

$$\kappa_T = 50.83101 \times 10^{-8} - 3.68293 \times 10^{-9} t + 7.263725 \times 10^{-11} t^2 - 6.597702 \times 10^{-13} t^3 + 2.87767 \times 10^{-15} t^4, \quad (7)$$

where κ_T is thermal compressibility in (kPa)⁻¹.

The estimate of standard deviation (SD) of the residual, calculated κ_T - data κ_T , is 2.1×10^{-11} (kPa)⁻¹; the ratio of SD to the midrange value of κ_T is 4.6×10^{-5} , which is negligible for present purposes. It is not necessary to make a correction to κ_T for air saturation.

The value of the isothermal compressibility of water is approximately 46.5 parts per million (ppm)/atmosphere at 20 °C. At locations where the atmospheric pressure is significantly different from 1 atmosphere (101.325 kPa), a correction for compressibility calculated using Eq. (7) should be made. For example, at Boulder, CO, the correction for compressibility is approximately -8 ppm at 20 °C.

3.6 Compressibility-Corrected Water Density Equation

The expression for the density of air-saturated water, ρ_{asc} , at an ambient pressure of P kPa is

$$\rho_{asc} = \rho_{as} [1 + \kappa_T (P - 101.325)], \quad (8)$$

where ρ_{as} is calculated using Eq. (6) and κ_T is calculated using Eq. (7).

4. Tables

Table 1 is a tabulation of values of the density of air-saturated water using Eq. (6). Table 2 is a tabulation of the values of the density of air-free water calculated using Eq. (3). Table 3 is a tabulation of values of air-free water calculated using the formulation of Wagenbreth and Blanke [1], this

table has been included in this paper for purposes of comparison.

The units for water density in these tables are g/cm^3 , as a convenience to those who routinely use these units.

Table 1. Density of air-saturated water (g/cm^3) from Eq. (6) using Kell [2] data

t (°C)	0.0	0.1	0.2	0.3	0.4	0.5	0.6	0.7	0.8	0.9
5	0.999961	0.999959	0.999957	0.999955	0.999953	0.999950	0.999948	0.999945	0.999942	0.999939
6	0.999936	0.999933	0.999930	0.999926	0.999922	0.999919	0.999915	0.999911	0.999906	0.999902
7	0.999897	0.999893	0.999888	0.999883	0.999878	0.999872	0.999867	0.999861	0.999856	0.999850
8	0.999844	0.999838	0.999832	0.999825	0.999819	0.999812	0.999805	0.999798	0.999791	0.999784
9	0.999777	0.999769	0.999761	0.999754	0.999746	0.999738	0.999730	0.999721	0.999713	0.999704
10	0.999695	0.999687	0.999678	0.999669	0.999659	0.999650	0.999640	0.999631	0.999621	0.999611
11	0.999601	0.999591	0.999581	0.999570	0.999560	0.999549	0.999538	0.999527	0.999516	0.999505
12	0.999494	0.999482	0.999471	0.999459	0.999447	0.999435	0.999423	0.999411	0.999398	0.999386
13	0.999373	0.999361	0.999348	0.999335	0.999322	0.999309	0.999295	0.999282	0.999268	0.999255
14	0.999241	0.999227	0.999213	0.999199	0.999184	0.999170	0.999156	0.999141	0.999126	0.999111
15	0.999096	0.999081	0.999066	0.999051	0.999035	0.999019	0.999004	0.998988	0.998972	0.998956
16	0.998940	0.998923	0.998907	0.998891	0.998874	0.998857	0.998840	0.998823	0.998806	0.998789
17	0.998772	0.998754	0.998737	0.998719	0.998701	0.998683	0.998665	0.998647	0.998629	0.998611
18	0.998592	0.998574	0.998555	0.998536	0.998517	0.998499	0.998479	0.998460	0.998441	0.998421
19	0.998402	0.998382	0.998363	0.998343	0.998323	0.998303	0.998283	0.998262	0.998242	0.998221
20	0.998201	0.998180	0.998159	0.998138	0.998117	0.998096	0.998075	0.998054	0.998032	0.998011
21	0.997989	0.997967	0.997945	0.997924	0.997901	0.997879	0.997857	0.997835	0.997812	0.997790
22	0.997767	0.997744	0.997721	0.997698	0.997675	0.997652	0.997629	0.997606	0.997582	0.997559
23	0.997535	0.997511	0.997487	0.997463	0.997439	0.997415	0.997391	0.997366	0.997342	0.997317
24	0.997293	0.997268	0.997243	0.997218	0.997193	0.997168	0.997143	0.997118	0.997092	0.997067
25	0.997041	0.997015	0.996990	0.996964	0.996938	0.996912	0.996885	0.996859	0.996833	0.996806
26	0.996780	0.996753	0.996726	0.996700	0.996673	0.996646	0.996619	0.996591	0.996564	0.996537
27	0.996509	0.996482	0.996454	0.996426	0.996399	0.996371	0.996343	0.996314	0.996286	0.996258
28	0.996230	0.996201	0.996173	0.996144	0.996115	0.996086	0.996057	0.996028	0.995999	0.995970
29	0.995941	0.995912	0.995882	0.995853	0.995823	0.995793	0.995764	0.995734	0.995704	0.995674
30	0.995643	0.995613	0.995583	0.995553	0.995522	0.995491	0.995461	0.995430	0.995399	0.995368
31	0.995337	0.995306	0.995275	0.995244	0.995212	0.995181	0.995149	0.995118	0.995086	0.995054
32	0.995023	0.994991	0.994959	0.994927	0.994894	0.994862	0.994830	0.994797	0.994765	0.994732
33	0.994699	0.994667	0.994634	0.994601	0.994568	0.994535	0.994502	0.994468	0.994435	0.994402
34	0.994368	0.994334	0.994301	0.994267	0.994233	0.994199	0.994165	0.994131	0.994097	0.994063
35	0.994028	0.993994	0.993960	0.993925	0.993890	0.993856	0.993821	0.993786	0.993751	0.993716
36	0.993681	0.993646	0.993610	0.993575	0.993539	0.993504	0.993468	0.993433	0.993397	0.993361
37	0.993325	0.993289	0.993253	0.993217	0.993181	0.993144	0.993108	0.993071	0.993035	0.992998
38	0.992962	0.992925	0.992888	0.992851	0.992814	0.992777	0.992740	0.992702	0.992665	0.992628
39	0.992590	0.992553	0.992515	0.992477	0.992439	0.992401	0.992363	0.992325	0.992287	0.992249

Table 2. Density of *air-free* water (g/cm³) from Eq. (3) using Kell [2] data

<i>t</i> (°C)	0.0	0.1	0.2	0.3	0.4	0.5	0.6	0.7	0.8	0.9
5	0.999965	0.999963	0.999961	0.999959	0.999957	0.999954	0.999952	0.999949	0.999946	0.999943
6	0.999940	0.999937	0.999934	0.999930	0.999926	0.999923	0.999919	0.999914	0.999910	0.999906
7	0.999901	0.999896	0.999892	0.999887	0.999881	0.999876	0.999871	0.999865	0.999860	0.999854
8	0.999848	0.999842	0.999835	0.999829	0.999822	0.999816	0.999809	0.999802	0.999795	0.999788
9	0.999780	0.999773	0.999765	0.999757	0.999749	0.999741	0.999733	0.999725	0.999716	0.999708
10	0.999699	0.999690	0.999681	0.999672	0.999663	0.999653	0.999644	0.999634	0.999624	0.999615
11	0.999604	0.999594	0.999584	0.999574	0.999563	0.999552	0.999541	0.999531	0.999519	0.999508
12	0.999497	0.999485	0.999474	0.999462	0.999450	0.999438	0.999426	0.999414	0.999402	0.999389
13	0.999377	0.999364	0.999351	0.999338	0.999325	0.999312	0.999299	0.999285	0.999272	0.999258
14	0.999244	0.999230	0.999216	0.999202	0.999188	0.999173	0.999159	0.999144	0.999129	0.999114
15	0.999099	0.999084	0.999069	0.999053	0.999038	0.999022	0.999007	0.998991	0.998975	0.998959
16	0.998943	0.998926	0.998910	0.998893	0.998877	0.998860	0.998843	0.998826	0.998809	0.998792
17	0.998774	0.998757	0.998739	0.998722	0.998704	0.998686	0.998668	0.998650	0.998632	0.998613
18	0.998595	0.998576	0.998558	0.998539	0.998520	0.998501	0.998482	0.998463	0.998444	0.998424
19	0.998405	0.998385	0.998365	0.998345	0.998325	0.998305	0.998285	0.998265	0.998244	0.998224
20	0.998203	0.998183	0.998162	0.998141	0.998120	0.998099	0.998077	0.998056	0.998035	0.998013
21	0.997991	0.997970	0.997948	0.997926	0.997904	0.997882	0.997859	0.997837	0.997815	0.997792
22	0.997769	0.997746	0.997724	0.997701	0.997678	0.997654	0.997631	0.997608	0.997584	0.997561
23	0.997537	0.997513	0.997489	0.997465	0.997441	0.997417	0.997393	0.997369	0.997344	0.997320
24	0.997295	0.997270	0.997245	0.997220	0.997195	0.997170	0.997145	0.997120	0.997094	0.997069
25	0.997043	0.997017	0.996992	0.996966	0.996940	0.996914	0.996887	0.996861	0.996835	0.996808
26	0.996782	0.996755	0.996728	0.996701	0.996675	0.996648	0.996620	0.996593	0.996566	0.996539
27	0.996511	0.996483	0.996456	0.996428	0.996400	0.996372	0.996344	0.996316	0.996288	0.996260
28	0.996231	0.996203	0.996174	0.996146	0.996117	0.996088	0.996059	0.996030	0.996001	0.995972
29	0.995942	0.995913	0.995884	0.995854	0.995824	0.995795	0.995765	0.995735	0.995705	0.995675
30	0.995645	0.995615	0.995584	0.995554	0.995523	0.995493	0.995462	0.995431	0.995401	0.995370
31	0.995339	0.995307	0.995276	0.995245	0.995214	0.995182	0.995151	0.995119	0.995087	0.995056
32	0.995024	0.994992	0.994960	0.994928	0.994895	0.994863	0.994831	0.994798	0.994766	0.994733
33	0.994701	0.994668	0.994635	0.994602	0.994569	0.994536	0.994503	0.994469	0.994436	0.994403
34	0.994369	0.994335	0.994302	0.994268	0.994234	0.994200	0.994166	0.994132	0.994098	0.994064
35	0.994029	0.993995	0.993960	0.993926	0.993891	0.993856	0.993822	0.993787	0.993752	0.993717
36	0.993682	0.993646	0.993611	0.993576	0.993540	0.993505	0.993469	0.993433	0.993398	0.993362
37	0.993326	0.993290	0.993254	0.993217	0.993181	0.993145	0.993108	0.993072	0.993035	0.992999
38	0.992962	0.992925	0.992888	0.992851	0.992814	0.992777	0.992740	0.992703	0.992665	0.992628
39	0.992590	0.992553	0.992515	0.992478	0.992440	0.992402	0.992364	0.992326	0.992288	0.992249

Table 3. Density of *air-free* water (g/cm³) from formulation of Wagenbreth and Blanke [1]

<i>t</i> (°C)	0.0	0.1	0.2	0.3	0.4	0.5	0.6	0.7	0.8	0.9
5	0.999964	0.999962	0.999960	0.999958	0.999956	0.999954	0.999951	0.999949	0.999946	0.999943
6	0.999940	0.999937	0.999933	0.999930	0.999926	0.999922	0.999918	0.999914	0.999910	0.999906
7	0.999901	0.999896	0.999892	0.999887	0.999881	0.999876	0.999871	0.999865	0.999860	0.999854
8	0.999848	0.999842	0.999835	0.999829	0.999822	0.999816	0.999809	0.999802	0.999795	0.999787
9	0.999780	0.999773	0.999765	0.999757	0.999749	0.999741	0.999733	0.999725	0.999716	0.999707
10	0.999699	0.999690	0.999681	0.999672	0.999662	0.999653	0.999643	0.999634	0.999624	0.999614
11	0.999604	0.999594	0.999583	0.999573	0.999562	0.999552	0.999541	0.999530	0.999519	0.999507
12	0.999496	0.999485	0.999473	0.999461	0.999449	0.999437	0.999425	0.999413	0.999401	0.999388
13	0.999376	0.999363	0.999350	0.999337	0.999324	0.999311	0.999297	0.999284	0.999270	0.999256
14	0.999243	0.999229	0.999215	0.999200	0.999186	0.999172	0.999157	0.999142	0.999128	0.999113
15	0.999098	0.999083	0.999067	0.999052	0.999036	0.999021	0.999005	0.998989	0.998973	0.998957
16	0.998941	0.998925	0.998908	0.998892	0.998875	0.998858	0.998841	0.998824	0.998807	0.998790
17	0.998773	0.998755	0.998738	0.998720	0.998702	0.998684	0.998666	0.998648	0.998630	0.998612
18	0.998593	0.998575	0.998556	0.998537	0.998519	0.998500	0.998480	0.998461	0.998442	0.998422
19	0.998403	0.998383	0.998364	0.998344	0.998324	0.998304	0.998284	0.998263	0.998243	0.998222
20	0.998202	0.998181	0.998160	0.998139	0.998118	0.998097	0.998076	0.998055	0.998033	0.998012
21	0.997990	0.997968	0.997947	0.997925	0.997903	0.997881	0.997858	0.997836	0.997814	0.997791
22	0.997768	0.997746	0.997723	0.997700	0.997677	0.997654	0.997630	0.997607	0.997584	0.997560
23	0.997536	0.997513	0.997489	0.997465	0.997441	0.997417	0.997392	0.997368	0.997344	0.997319
24	0.997294	0.997270	0.997245	0.997220	0.997195	0.997170	0.997145	0.997119	0.997094	0.997068
25	0.997043	0.997017	0.996991	0.996966	0.996940	0.996913	0.996887	0.996861	0.996835	0.996808
26	0.996782	0.996755	0.996723	0.996702	0.996675	0.996648	0.996621	0.996593	0.996566	0.996539
27	0.996511	0.996484	0.996456	0.996428	0.996401	0.996373	0.996345	0.996316	0.996288	0.996260
28	0.996232	0.996203	0.996175	0.996146	0.996117	0.996088	0.996060	0.996031	0.996001	0.995972
29	0.996943	0.995914	0.995884	0.995855	0.995825	0.995795	0.995765	0.995736	0.995706	0.995676
30	0.995645	0.995615	0.995585	0.995554	0.995524	0.995493	0.995463	0.995432	0.995401	0.995370
31	0.995339	0.995308	0.995277	0.995246	0.995214	0.995183	0.995151	0.995120	0.995088	0.995056
32	0.995024	0.994992	0.994960	0.994928	0.994896	0.994864	0.994831	0.994799	0.994766	0.994734
33	0.994701	0.994668	0.994635	0.994602	0.994569	0.994536	0.994503	0.994470	0.994436	0.994403
34	0.994369	0.994336	0.994302	0.994268	0.994234	0.994201	0.994167	0.994132	0.994098	0.994064
35	0.994030	0.993995	0.993961	0.993926	0.993891	0.993857	0.993822	0.993787	0.993752	0.993717
36	0.993682	0.993647	0.993611	0.993576	0.993541	0.993505	0.993469	0.993434	0.993398	0.993362
37	0.993326	0.993290	0.993254	0.993218	0.993182	0.993146	0.993109	0.993073	0.993036	0.993000
38	0.992963	0.992926	0.992889	0.992852	0.992815	0.992778	0.992741	0.992704	0.992667	0.992629
39	0.992592	0.992554	0.992517	0.992479	0.992442	0.992404	0.992366	0.992328	0.992290	0.992252

5. Summary

Equation (3) can be used to calculate the density of *air-free* water in the temperature range of 5 to 40 °C in ITS-90 at one atmosphere.

Equation (6) can be used to calculate the density of *air-saturated* water in the same temperature range at one atmosphere.

Equation (8) can be used to calculate the density of air-saturated water in the same temperature range at an ambient pressure of P kPa.

The use of Eq. (6) for air-saturated water, and Eq. (8) where appropriate, is recommended for calculation of water density.

6. References

- [1] H. Wagenbreth, and W. Blanke, PTB Mitt. **81**, 412 (1971).
- [2] G. S. Kell, J. Chem. Eng. Data **20**, 97 (1975).
- [3] B. W. Mangum, and G. T. Furukawa, Natl. Inst. Stand. Technol. Technical Note 1265 (1990).
- [4] N. Bignell, Metrologia **19**, 57 (1983).

About the authors: Frank E. Jones is a physicist and an independent consultant who retired from the National Bureau of Standards (now NIST) in 1987. Georgia L. Harris is a physical scientist with the Office of Weights and Measures at NIST. The National Institute of Standards and Technology is an agency of the Technology Administration, U.S. Department of Commerce.

Heat Capacity and Thermodynamic Properties of Poly(chlorotrifluoroethylene) from 2.5 to 620 K

Volume 97

Number 3

May-June 1992

Shu-Sing Chang and James J. Weeks¹

National Institute of Standards and Technology,
Gaithersburg, MD 20899

Heat capacities and thermodynamic properties of a number of poly(chlorotrifluoroethylene) samples subjected to various thermal treatments, to achieve crystallinities ranging from approximately 10 to 90%, have been studied from 2.5 to 370 K by automated adiabatic calorimetry and from 250 to 620 K by differential scanning calorimetry. Small heat capacity discontinuities in the temperature range from 320 to 350 K were observed in all samples with crystallinities greater than 40%. Spontaneous adiabatic temperature drifts associated with these anomalies were positive (exothermic) for quenched samples and negative (endothermic) for annealed samples. Therefore these anomalies were believed to be associated with a relaxation phenomenon similar to that of a glass transition. For highly quenched low crystallinity films, a

much larger heat capacity discontinuity of greater than 15% was observed, amidst a crystallization exotherm. In addition to the above phenomena, annealing of the sample at any temperature between 240 to 400 K would produce a shift in the population distribution of crystallites from reorganization or melting and recrystallization. As a result, the apparent heat capacity became somewhat lowered at the annealing temperature and somewhat raised at about 20 K above the annealing temperature.

Key words: automated adiabatic calorimetry; crystallite distribution; differential scanning calorimetry; glass transition; heat capacity; poly(chlorotrifluoroethylene); residual entropy; thermodynamic properties.

Accepted: October 28, 1991

1. Introduction

Although poly(chlorotrifluoroethylene), PCTFE, is a fairly well-studied polymer in its physical and mechanical properties, its heat capacity and associated thermodynamic properties are only reported in a few publications [1-4] covering the temperature ranges: 2.5 to 20 K [2,4], 80 to 340 K [3] and 273 to 515 K [1]. There are also thermal analytical studies concerned mainly with the melting and crystallization phenomena near the fusion region.

Glass transition phenomena were not observed by thermal means in the above mentioned publications. Dilatometric studies [5,6], however, have indicated the occurrence of a glass transition near 325 K. Dielectric [7,8] and mechanical relaxation [9] studies have also indicated a glass transition-like relaxation together with crystalline relaxations.

Since the crystallinity of PCTFE can be changed over a wide range [6], the heat capacity behavior of three PCTFE samples of varied crystallinity and thermal treatments was studied in this work with a

¹ Present address: Route 1, Box 121, Mathias, WV 26812.

fully automated, high precision, adiabatic calorimeter [10], for the temperature range from 2.5 to 370 K, and by a commercial differential scanning calorimeter from 250 to 620 K. The precision of the adiabatic calorimeter, except at temperatures below 50 K, was of the order of 0.02%. The high sensitivity in the detection of spontaneous temperature changes, on the order of 10^{-5} K, enabled the detection of the occurrence of broad relaxation phenomena, such as that occurring in polyethylene [11]. Techniques used in the adiabatic calorimetry enabled the separation of the underlying heat capacity contributed by lattice vibrations from that contributed by spontaneous thermal events occurring in the sample. The present work confirmed the existence of a glass-like relaxation in PCTFE, occurring in the temperature region from 320 to 350 K. In the transition region, the spontaneous adiabatic temperature drifts were positive (exothermic) for quenched samples and negative (endothermic) for annealed samples.

Data from differential scanning calorimetry, covering a temperature range from 250 to 620 K, were used to supplement the adiabatic calorimetry at temperatures above 370 K. The fast thermal analysis operation enabled the study of a large number of samples with various thermal histories. In addition to the confirmation of the existence of the glass transition discontinuities in most samples studied, crystallization and melting were also studied. The glass transition occurs amidst a complicated crystalline reorganization phenomenon over a wide temperature range from 240 to 400 K. By following rigorous calibration procedures, heat capacities and heats of fusion were obtained with reasonable precision using scanning calorimetry.

Combining the results from both adiabatic and scanning calorimetry, thermodynamic functions of the crystalline and the amorphous phases may be estimated. The amorphous phase contains a residual entropy at 0 K.

2. Experimental Detail

2.1 Materials

The adiabatic calorimetric samples of poly(chlorotrifluoroethylene), PCTFE, were composed of typical factory production KEL-F 81 brand plastics, KF-6060 pellet and KF-6061 powder, from Minnesota Mining and Manufacturing

Company.² Both batches were of Grade 3 quality with the degree of polymerization of about 1600, or a molecular weight of near 190,000. The molecular weight of the repeating monomeric unit, $-\text{CClF}-\text{CF}_2-$, is $116.47 \text{ g mol}^{-1}$. Three samples were loaded into the adiabatic calorimeter: (1) KF-6060 pellets as received, (2) high crystallinity sample prepared by slow crystallization from molten KF-6061 powder, and (3) quenched films made from KF-6061 powder. Table 1 lists loading conditions for the three adiabatic calorimetric samples, along with their initial densities ρ_i and crystallinities X_i . After the evacuation, a small amount of helium gas at a room temperature of about 296 K was sealed with the sample to aid the thermal conductivity. The amount of helium gas was equal to the weight of helium used when the empty sample container was measured.

In order to achieve a maximum degree of crystallinity, a slow melt-crystallized sample was prepared by heating KF-6061 powder in vacuum above the melting point to 525–535 K, until all bubbles collapsed into a clear liquid. A motorized voltage source was used to slowly decrease the power to the heating mantle. The melt was cooled at a rate of 1–2 K per d, from 500 to about 400 K.

To achieve the lowest degree of crystallinity, thin films of PCTFE of about 0.15 mm thickness were prepared by pressing the melt of KF-6061 powder between two aluminum plates at about 575–590 K. The plates and the molten film were then quenched in icy water. In most of the films, the center portion of the film showed effects of air pockets and some anisotropic characteristics as the samples were viewed between crossed polarizers. Although the ranges of the densities of the clear

Table 1. Adiabatic calorimeter loading of PCTFE samples

Designation	Mass (vacuo) g	ρ_i g cm ⁻³	X_i	He kPa
X (Slow crystallized)	124.617	2.170	0.87	4.2
P (Pellet, as received)	145.147	2.133	0.54	5.3
F (Film)	63.396	2.095	0.13	3.3

² Certain commercial equipment, instruments, or materials are identified in this paper to specify adequately the experimental procedure. Such identification does not imply recommendation or endorsement by the National Institute of Standards and Technology, nor does it imply that the materials or equipment identified are necessarily the best available for the purpose.

region and the anisotropic region were about the same at $2.095 \pm 0.005 \text{ g cm}^{-3}$, in order for the calorimetric sample to retain as high an amorphous character as possible, the optically anisotropic regions were cut off and not used.

Initial crystallinities of the three samples were estimated from their densities as 0.13, 0.54, and 0.87 for the film, pellet, and melt-crystallized samples, respectively. The densities [6] of 2.076 and 2.186 g cm^{-3} for the amorphous and the crystalline phases, respectively, were used for the crystallinity estimation. For DSC measurements, besides the samples described above, the KF-6061 powder as received, quenched films made from KF-6060 pellets, a manufactured PCTFE tubing of 0.11 mm thickness, and a low molecular weight PCTFE KEL-F 200 Wax were also used.

If the quenched films had not been exposed to 325 K or higher temperatures, the x-ray ($\text{CuK}\alpha$) diffraction patterns of these highly amorphous samples all showed an intense halo centered around a 2θ value of 15.5° or around a spacing of 5.7 \AA plus two fainter broad halos at around 32° and 39° or around 2.8 and 2.3 \AA , similar to that found in commercial PCTFE films [12,13]. A faint halo at 8° or about 11 \AA was always observed. For crystalline PCTFE, regardless of thermal treatments and degrees of crystallinity, the most intense lines are located at 5.5 , 5.4 , 5.2 , and 4.9 \AA , which are followed by two groups of fainter rings starting at 3.2 and 2.8 \AA , as observed previously [14]. However, in all crystalline samples, there appeared also the halos at 11 and 2.3 \AA . In addition, there was also a diffused ring at 14.8° or 6.0 \AA .

The x-ray pattern of the low molecular weight KEL-F 200 wax, above its melting point at 373 K , appeared just like the amorphous film. At 409 K , the major halo shifted to 15° or the spacing increased to 5.9 \AA . At room temperature, crystallized wax showed rings similar to that of the crystalline high molecular weight PCTFE, except the rings are more diffuse and somewhat difficult to resolve.

2.2 Adiabatic Calorimetry

A fully automated vacuum adiabatic calorimeter operating in the temperature range from 2 to 370 K [10] was used in this investigation. The calorimetric system included an automated analog adiabatic shield control system as improved from an earlier description [15], and a digital system for data acquisition and experimental control [10]. The analog control system was capable of maintaining the shield temperature and following the temperature

changes of the sample container to within 1 mK . The principal measuring instruments in the digital system included a high resolution, self-balancing potentiometer [16] as modified from a commercially available manual potentiometer of a Diesselhorst ring [17] design, highly stable constant current sources, and a commercially available nanovolt amplifier with a linearity of 0.01% . This system was capable of measuring 0.1 V at full-scale with a resolution of less than 10 nV . Therefore this system provided a temperature resolution of near 10^{-5} K at temperatures above 50 K , from a nominal 25Ω platinum resistance thermometer operating at a current of $1\text{--}2 \text{ mA}$.

Above 14 K , the temperature scale used was IPTS-1968 [18]. At lower temperatures, the platinum resistance thermometer was calibrated against a germanium thermometer which was in turn calibrated against the NBS provisional temperature scale 2-20 (1965) [19]. The temperature scale below 14 K may either be interpolated directly from the calibration data or by following a three point calibration procedure [20]. At temperatures below 273 K , the scale IPTS-1968 differs from ITS-90 [21] by a maximum of 14 mK in the temperature region of 130 to 160 K . Between 273 and 373 K , the size of the temperature unit changes by 0.025% . The greatest change of 0.1% in the size of the temperature unit occurs at temperature regions of between $15\text{--}20 \text{ K}$ and $50\text{--}60 \text{ K}$. The changes in the size of the temperature unit directly affects the heat capacity value calculation. Since the changes were 0.1% or less, no corrections were made to change the temperature scale from IPTS-1968 to ITS-90.

The heat capacity, C_p , of the sample container assembly, including the sample, the container, the thermometer and the heater, was determined by the equilibrium temperature rise produced by an electrical energy input. The decay time constant toward the establishment of a temperature equilibrium after a disturbance was in the order of 100 s for this assembly [22]. Approximately 15 min were required after each energy input to reestablish a temperature equilibrium, or to reach a temperature drift on the order of or less than 0.1 mK min^{-1} . The small drift arises from heat exchanges between the calorimeter and its surroundings due to a residual deviation in the control of a strict adiabatic condition. The time constant is much shorter at low temperatures due to the increase in the thermal conductivity of most materials. Much longer decay time constants with temperature drifts greater than that expected from the non-adiabatic

conditions of the shield control system indicated the presence of a spontaneous thermal effect originating in the sample. Even under these adverse conditions, the instantaneous or short term heat capacities, contributed mainly from lattice vibrations, could still be estimated by extrapolating the drifts to obtain the temperature rise at the middle of an energy input. The energy of the spontaneous thermal event over a temperature range is obtainable by summing all energy inputs under adiabatic conditions and then subtracting from it the enthalpy increments as integrated from the lattice vibration heat capacity curve.

2.3 Differential Scanning Calorimetry

Some of the early heats of fusion and melting points were observed with a Perkin-Elmer DSC-1B differential scanning calorimeter. Most of the thermal analyses were performed with a Perkin-Elmer DSC-2 differential scanning calorimeter. The accuracy of the DSC measurements depended strongly on calibrations and the correctness of the assigned baseline for each scan. Meltings of indium and benzoic acid were used to calibrate the scales for the temperature and the power. Although scans of different rates were sometimes used, most of the runs were performed at a heating rate of 10 K min^{-1} . Due to the thermal conductivity of the system, the temperature of the sample capsule lags behind the temperature of the thermometer/sample holder assembly as a function of heating rates by about $0.06 \text{ K (K min}^{-1})^{-1}$. For better precision in heat capacity determinations, calibration scans of sapphire discs were frequently performed and the results compared against standard values [23,24]. For even better precision in heat capacity determinations, short scans with scanning temperature ranges of 5 to 10 K were used. Under these conditions, the uncertainty in the baseline is minimized. The average heat capacity for the 5 to 10 K interval may also be calculated by integrating the scan curve for the enthalpy and dividing the latter by the temperature interval, as in the intermittent heating method used in the adiabatic calorimetry. Heat capacities obtained by the short range method were found in agreement with adiabatic values to better than 0.5%.

Although DSC scans were performed at much lower temperatures, only the data above 250 K, where C_p of PCTFE began to vary significantly with crystallinity, were used to supplement the adiabatic data.

One peculiar result was observed when heat capacities were calculated from continuous scans at temperatures above 500 K. The heat capacity values from continuous scans became progressively higher than that from short scans by about 20% at 600 K. Similar results were observed when the heat capacities of copper and teflon were measured. The reason for the occurrence of this discrepancy is unknown. It may be of instrumental nature or due to contamination or chemical reactions. Therefore long scans at high temperatures were used only for the observation of the melting points and the heat of fusion. The short scans were used for the heat capacity of the liquid at high temperatures.

3. Results and Discussion

3.1 Adiabatic Calorimetry

The conditions and thermal histories before each series of adiabatic calorimetric measurements on the three samples are listed chronologically in Table 2. The results of the heat capacity measurements are listed in Table 3 and shown in different regions in Figs. 1 and 2. For clarity, not all series of measurements are shown in Fig. 1, as the results are close to each other below 250 K. As mentioned previously, the heat capacity reported here from adiabatic calorimetry represents mainly the vibrational contribution, free from the influence of long term spontaneous drifts due to crystallization and glassy relaxation.

3.1.1 Heat Capacity At low temperatures, a Debye T^3 region was not observed in this investigation. The values of C_p/T^3 were still increasing rapidly for all samples even at 2.5 K as the temperature was lowered, see Fig. 3. This is characteristic of the presence of a large amount of disorder and soft mode of vibration in all PCTFE samples, regardless of their crystallinities as estimated by the density. The rise of C_p/T^3 to a peak, before a possible Debye region occurs at a lower temperature, has been observed generally in the temperature range of 2–5 K for almost all glassy materials. This peak occurs at 4 K for *cis*-1,4-polyisoprene [25], 3 K for amorphous selenium [26,27], 3–7 K for a number of thermoset resins as summarized in Ref. [28], and 3 K for polystyrene [29–31]. Similar to this investigation, the C_p/T^3 values have not yet reached a peak even at 2 K for glassy *o*-terphenyl [32] and poly(vinylchloride) [33]. Weaker peaks also exist in highly crystalline polyethylene [34],

Table 2. Conditions and thermal histories of PCTFE

Designation	Sample Run	Range		Conditions
		T_i , K	T_f , K	
P	P1	300	350	As received, No liquid nitrogen refrigeration
	PQ1	65	205	Cooled from 350 K at -5 K/min
	PQ2	3	125	Cooled from 350 K at -5 K/min
	PA	3	370	Annealed at 320 K and cooled at -5 K/h
	PQ3	200	370	Cooled from 370 K at -6 K/min
	PSC	300	370	Slow cooled from 370 K at -0.5 K/h
X	X1	310	370	First run as prepared
	XQ1	150	355	Cooled from 370 K at -5 K/min
	XSC	8	175	Slow cooled from 340 K at -0.33 K/h
	XQ2	3	370	Cooled from 370 K at -5 K/min
F	F1	10	16	Run as prepared
	F2	190	215	Run as prepared
	F3	5	365	First run as prepared
	FQ	65	370	Cooled from 370 K at -5 K/min
	FSC	265	370	Slow cooled from 370 K at -0.5 K/h
	FRT	295	365	1 month at room temperature

Table 3. Heat capacities of PCTFE (1 mol = 116.47 g)

T K	C_p $J K^{-1} mol^{-1}$	T K	C_p $J K^{-1} mol^{-1}$	T K	C_p $J K^{-1} mol^{-1}$
Pellet					
P1					
305.01	101.33	320.07	105.88	335.24	110.91
309.98	102.81	325.08	107.39	340.28	112.80
315.01	104.23	330.14	109.01	345.35	114.39
PQ1					
65.40	26.66	112.28	45.49	161.94	62.24
69.25	28.24	115.77	46.77	165.63	63.38
71.68	29.21	119.28	48.06	169.27	64.48
75.05	30.63	122.82	49.34	172.87	65.54
78.44	32.03	126.29	50.56	176.52	66.63
81.86	33.43	129.81	51.79	180.23	67.71
85.17	34.80	133.36	53.02	183.90	68.78
88.53	36.17	136.85	54.21	187.52	69.81
91.88	37.53	140.39	55.39	191.21	70.85
95.24	38.88	143.98	56.67	194.95	71.91
98.61	40.21	147.51	57.70	198.65	72.94
102.00	41.54	151.09	58.85	202.32	73.95
105.41	42.87	154.72	60.00		
108.83	44.19	158.31	61.12		

Table 3. Heat capacities of PCTFE (1 mol = 116.47 g)—Continued

T K	C_p $\text{J K}^{-1} \text{mol}^{-1}$	T K	C_p $\text{J K}^{-1} \text{mol}^{-1}$	T K	C_p $\text{J K}^{-1} \text{mol}^{-1}$
Pellet					
PQ2					
2.56	0.13	13.67	4.55	67.72	27.64
2.60	0.15	14.98	5.21	72.11	29.44
2.78	0.15	16.46	5.96	76.43	31.25
3.15	0.22	18.18	6.83	80.80	33.15
3.66	0.33	20.14	7.79	85.23	34.88
4.24	0.46	22.46	8.91	89.64	36.70
4.86	0.63	24.95	10.07	94.04	38.46
5.52	0.83	27.63	11.27	98.45	40.23
6.23	1.10	30.87	12.67	102.88	41.95
6.99	1.40	34.60	14.23	107.32	43.70
7.71	1.69	38.81	15.94	111.80	45.36
8.43	2.02	43.86	17.96	116.32	47.08
9.34	2.43	49.18	20.10	120.89	48.68
10.42	2.94	54.07	22.08	125.51	50.48
11.48	3.45	58.68	23.93		
12.50	3.97	63.21	25.80		
PA					
2.77	0.18	83.24	34.08	230.24	81.30
2.97	0.18	87.56	35.84	235.19	82.56
3.47	0.28	91.95	37.63	240.07	83.87
4.17	0.44	96.44	39.44	244.91	85.08
4.97	0.67	100.94	41.19	249.80	86.28
5.84	0.96	105.46	42.94	254.74	87.66
6.82	1.33	110.00	44.71	259.63	88.87
7.86	1.76	114.57	46.42	264.58	90.17
8.90	2.23	119.10	48.07	255.46	87.54
10.08	2.78	123.59	49.67	261.90	89.20
11.31	3.37	128.14	51.28	266.53	90.57
12.48	3.96	132.75	52.85	271.41	91.97
13.77	4.60	137.42	54.48	276.34	93.37
15.18	5.30	142.07	56.00	281.31	94.77
16.69	6.08	146.71	57.52	286.34	96.01
18.34	6.93	151.42	59.03	291.31	97.49
21.02	8.22	156.14	60.46	296.24	98.88
23.94	9.61	163.18	62.66	301.22	100.28
26.66	10.85	168.93	64.32	306.24	101.59
29.79	12.21	172.40	65.38	311.21	103.02
33.07	13.60	177.21	66.79	316.24	104.26
36.76	15.11	181.95	68.22	321.31	105.76
41.08	16.86	186.73	69.56	326.33	107.12
46.36	18.99	191.55	70.92	331.39	109.19
51.76	21.18	196.32	72.23	336.47	111.28
56.61	23.12	201.12	73.60	341.50	113.18
61.22	24.98	205.98	74.90	346.56	114.76
65.65	26.79	210.77	76.20	351.68	116.09
70.08	28.64	215.62	77.48	356.75	117.35
74.53	30.45	220.51	78.70	361.88	118.58
78.91	32.31	225.35	80.03	367.07	119.75

Table 3. Heat capacities of PCTFE (1 mol = 116.47 g)—Continued

T K	C_p $J K^{-1} mol^{-1}$	T K	C_p $J K^{-1} mol^{-1}$	T K	C_p $J K^{-1} mol^{-1}$
Pellet					
PQ3					
204.46	74.50	267.39	90.91	322.93	106.77
208.76	75.64	272.36	92.29	325.90	107.75
213.62	76.98	277.28	93.59	328.85	108.57
218.54	78.24	282.25	94.95	331.78	109.61
223.39	79.58	287.27	96.42	334.69	110.75
228.20	80.83	292.24	97.83	337.59	111.74
233.05	82.08	297.25	99.25	340.46	112.94
237.96	83.35	302.31	100.72	343.38	114.00
242.82	84.66	307.32	102.19	346.36	114.62
247.73	85.80	311.26	103.31	350.50	115.66
252.70	87.10	314.15	104.19	355.70	116.70
257.61	88.34	317.02	104.99	360.94	118.23
262.47	89.63	319.94	106.01	366.33	119.50
PSC					
302.13	100.43	328.07	107.62	351.37	115.91
306.04	101.42	331.96	108.92	335.30	116.83
309.92	102.54	335.80	110.66	359.29	117.85
316.73	104.28	339.68	112.56	363.26	118.78
320.46	105.50	343.60	113.89	367.20	119.72
324.16	106.47	347.50	114.97		
Slow melt-crystallized					
X1					
313.68	100.48	334.31	105.03	354.66	109.02
319.20	101.78	339.45	105.98	359.76	109.98
324.23	103.02	344.55	107.03	364.93	111.03
329.24	104.00	349.62	107.95	370.06	112.10
XQ1					
154.40	60.16	219.90	79.19	288.89	95.25
157.77	61.24	224.72	80.49	293.97	96.24
162.51	62.70	229.62	81.73	299.01	97.33
167.18	64.18	234.57	82.92	304.00	98.39
171.89	65.56	239.46	84.12	308.97	99.45
176.65	67.03	244.31	85.38	313.99	100.54
181.34	68.38	249.22	86.47	319.08	101.67
186.08	69.82	254.19	87.61	324.23	102.85
190.86	71.18	259.11	88.73	329.35	103.97
195.59	72.56	264.00	89.81	334.42	104.99
200.36	73.87	268.95	90.94	339.57	105.97
205.21	75.23	273.97	91.99	344.67	107.03
210.09	76.68	278.95	93.11	349.74	107.94
215.02	77.98	283.89	94.14	354.78	108.95

Table 3. Heat capacities of PCTFE (1 mol = 116.47 g)—Continued

T K	C_p J K ⁻¹ mol ⁻¹	T K	C_p J K ⁻¹ mol ⁻¹	T K	C_p J K ⁻¹ mol ⁻¹
Slow melt-crystallized					
XSC					
8.09	1.83	37.63	15.71	117.00	47.45
8.96	2.22	41.53	17.26	121.49	49.10
10.28	2.86	60.86	25.04	125.99	50.73
11.49	3.46	64.76	26.59	130.50	52.30
12.70	4.07	68.71	28.20	135.04	53.88
14.00	4.74	73.02	30.00	139.60	55.40
15.41	5.49	77.35	31.78	144.19	56.93
16.95	6.29	81.73	33.58	148.81	58.41
18.63	7.16	86.17	35.40	153.47	59.90
20.48	8.09	90.54	37.18	158.16	61.38
22.53	9.10	94.58	38.91	162.90	62.86
24.81	10.20	99.27	40.66	167.56	64.28
27.39	11.37	103.66	42.39	172.26	65.73
30.33	12.66	108.03	44.07		
33.72	14.11	112.52	45.78		
XQ2					
3.02	0.19	92.59	38.08	247.92	86.21
3.69	0.31	97.01	39.83	252.90	87.41
4.55	0.52	101.45	41.60	257.83	88.51
5.57	0.83	105.92	43.30	262.72	89.49
6.70	1.24	110.43	45.06	267.68	90.61
7.92	1.75	114.98	46.77	272.71	91.65
9.19	2.33	119.58	48.45	277.70	92.76
10.46	2.94	124.15	50.11	282.64	93.80
11.68	3.54	128.59	51.58	287.56	94.81
12.88	4.17	133.18	53.19	292.44	95.84
14.19	4.83	137.90	54.81	297.38	96.87
15.62	5.59	142.53	56.36	302.39	97.91
17.18	6.40	147.18	57.89	306.36	98.74
18.88	7.29	151.86	59.40	309.39	99.48
20.69	8.19	156.58	60.95	312.32	100.10
22.62	9.14	166.01	63.90	315.16	100.67
24.84	10.20	170.73	65.38	318.06	101.41
27.40	11.37	175.49	66.77	320.95	102.29
30.23	12.61	180.18	68.22	323.82	102.73
33.43	13.98	184.93	69.58	326.68	103.38
37.24	15.55	189.72	70.98	329.54	103.95
41.71	17.32	194.45	72.30	332.45	104.55
47.01	19.44	199.23	73.65	335.44	105.12
52.32	21.56	204.07	74.96	338.41	105.79
57.09	23.51	208.85	76.27	341.37	106.44
61.76	25.41	213.68	77.59	347.49	107.42
66.26	27.24	218.57	78.96	350.99	108.23
70.64	29.04	223.41	80.17	354.89	108.97
74.95	30.82	228.31	81.40	358.77	109.75
79.32	32.68	233.26	82.66	362.63	110.52
83.76	34.47	238.16	83.84	366.06	111.22
88.18	36.25	243.01	85.16	369.93	112.08

Table 3. Heat capacities of PCTFE (1 mol = 116.47 g)—Continued

T K	C_p J K ⁻¹ mol ⁻¹	T K	C_p J K ⁻¹ mol ⁻¹	T K	C_p J K ⁻¹ mol ⁻¹
Quenched film					
F1					
9.95	2.72	12.25	3.83	14.86	5.12
11.00	3.22	13.50	4.45	16.34	5.84
F2					
190.74	70.46	200.22	73.07	209.90	75.73
195.51	71.80	205.02	74.40	214.74	77.02
F3					
4.79	0.62	109.73	44.52	275.89	93.98
5.72	0.93	114.20	46.18	280.78	95.65
6.86	1.36	118.75	47.86	285.75	97.17
8.09	1.87	123.29	49.50	290.68	98.75
9.36	2.44	127.82	51.09	295.57	100.46
10.63	3.03	132.46	52.71	299.45	101.93
11.84	3.61	137.11	54.26	302.34	103.34
13.06	4.21	141.76	55.73	304.94	104.92
14.37	4.84	146.43	57.29	307.25	106.62
15.80	5.56	151.12	58.72	309.65	107.40
17.36	6.32	155.84	60.26	312.05	108.33
19.06	7.15	165.25	63.10	314.45	109.72
20.92	8.03	169.91	64.51	316.92	110.87
22.99	9.01	174.64	65.86	319.37	112.15
27.86	11.19	179.32	67.26	321.83	113.52
30.57	12.34	184.07	68.62	324.27	114.73
33.64	13.64	188.91	69.98	326.71	116.28
37.30	15.15	193.69	71.29	329.14	117.82
41.61	16.87	198.41	72.61	331.58	119.69
46.77	18.98	203.10	73.86	334.02	122.34
51.99	21.10	207.86	75.16	336.51	122.43
56.65	23.01	212.71	76.51	338.94	122.52
61.09	24.81	217.51	77.78	341.29	122.99
65.52	26.66	222.27	79.09	343.69	123.22
69.98	28.49	227.11	80.43	346.16	123.88
74.38	30.34	232.04	81.73	348.69	123.51
78.73	32.18	236.93	82.97	351.19	124.13
83.08	34.00	241.77	84.21	353.60	124.84
87.44	35.74	246.56	85.90	355.99	124.99
91.82	37.53	251.44	86.94	358.37	125.34
96.24	39.29	256.41	88.31	360.73	125.86
100.71	41.06	261.34	89.69	363.60	126.71
105.24	42.89	266.23	91.15		

Table 3. Heat capacities of PCTFE (1 mol = 116.47 g)—Continued

T K	C_p $J K^{-1} mol^{-1}$	T K	C_p $J K^{-1} mol^{-1}$	T K	C_p $J K^{-1} mol^{-1}$
Quenched film					
FQ					
66.73	27.16	160.29	61.64	266.24	91.06
70.56	28.72	165.02	63.09	274.10	92.39
74.84	30.51	169.83	64.53	276.03	93.89
78.99	35.25	174.57	65.93	281.06	95.46
83.25	33.99	183.88	68.60	286.04	97.01
87.62	35.77	188.59	69.99	290.98	98.61
91.95	37.54	193.37	71.32	295.87	100.21
96.26	39.27	198.11	72.61	300.85	101.87
100.71	41.02	202.92	73.92	305.90	103.60
105.16	42.75	207.82	75.23	310.91	105.22
109.62	44.45	212.68	76.54	315.88	106.98
114.09	46.13	217.48	77.86	320.93	108.37
118.59	47.79	222.24	79.09	326.07	110.15
123.13	49.41	227.09	80.41	331.15	111.83
127.68	51.01	232.03	81.60	336.20	113.57
132.28	52.60	236.92	82.96	341.21	115.42
136.91	54.18	241.76	84.39	346.29	117.49
141.61	55.73	246.56	85.65	351.44	119.65
146.22	57.23	251.44	86.92	356.53	121.85
150.89	58.71	256.42	88.26	361.57	123.83
155.63	60.18	261.35	89.59	366.69	125.52
FSC					
267.79	90.94	301.99	101.85	337.06	112.99
272.40	92.70	307.03	103.54	342.05	114.98
277.34	94.01	312.03	105.09	347.12	117.55
282.23	95.54	316.99	106.74	352.35	120.70
287.20	97.03	322.04	108.22	357.66	122.66
292.13	98.71	327.04	109.75	362.79	124.53
297.02	100.22	332.01	111.30	367.89	125.98
FRT					
296.81	100.06	319.78	107.85	343.70	116.07
298.74	100.81	321.79	108.46	346.53	117.38
300.63	101.43	323.73	109.10	349.45	119.00
302.51	102.15	325.66	109.69	351.51	119.86
304.46	102.96	327.59	110.23	335.46	120.86
306.39	103.51	329.46	110.72	355.45	122.06
308.38	104.22	331.43	111.42	357.43	122.91
310.30	104.66	333.45	112.07	359.46	123.61
312.17	105.41	335.41	112.70	361.48	124.05
314.08	106.10	337.41	113.47	363.49	124.72
315.99	106.64	339.67	113.50		
317.89	107.17	341.77	114.87		

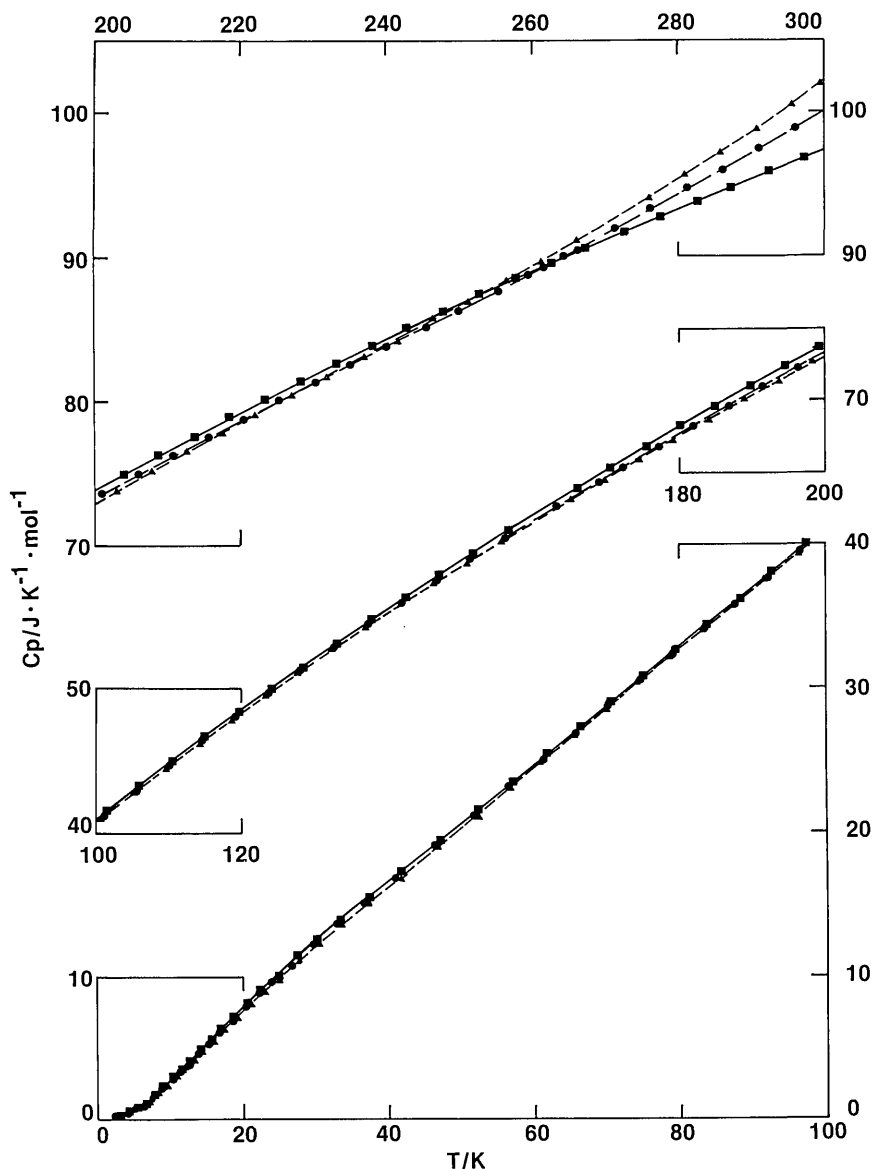


Fig. 1. Heat capacity of PCTFE.

Film: ▲. Pellet: ●. Slow crystallized: ■.

crystalline *o*- and *p*-terphenyl [32,35] and even in a hard crystalline material such as sapphire [23].

There are two publications [2,4] reporting the cryogenic behavior of PCTFE. From thermal conductivity measurements of a sample of PCTFE with a density of 2.114 g cm^{-3} from 1 to 4.5 K [2], an average value for C/T^3 of $0.123 \text{ mJ K}^{-4} \text{ cm}^{-3}$ or about $6.8 \text{ mJ K}^{-4} \text{ mol}^{-1}$ was given. This value is approximately the average of the values observed in the present study, see Fig. 3.

The results of specific heat measurements for a sample of PCTFE without detailed description from 2.5 to 20 K are reported in several ways [4], which are also shown in Fig. 3 for comparison. The

graphical data were estimated from a $\log(C)$ - $\log(T)$ plot for $T < 10 \text{ K}$ and from a C/T^2 plot for $T > 10 \text{ K}$ from their publication. The data at 20 K was also obtained from the log-log plot, as the T^2 plot only extended to 18 K. Only in the region between 6 to 14 K, do the graphical data agree reasonably well with our data. Below 5 K, the graphical data indicate a lowering of C/T^3 from $4.6 \text{ mJ K}^{-4} \text{ mol}^{-1}$ at 5 K to $3.7 \text{ mJ K}^{-4} \text{ mol}^{-1}$ at 2.5 K. The value at 2.5 K was nearly one-half of that from this study and that from a thermal conductivity study [2]. The authors, however, assigned a much higher Debye constant of $5.6 \text{ mJ K}^{-4} \text{ mol}^{-1}$, which is much higher than their graphical data, but is still

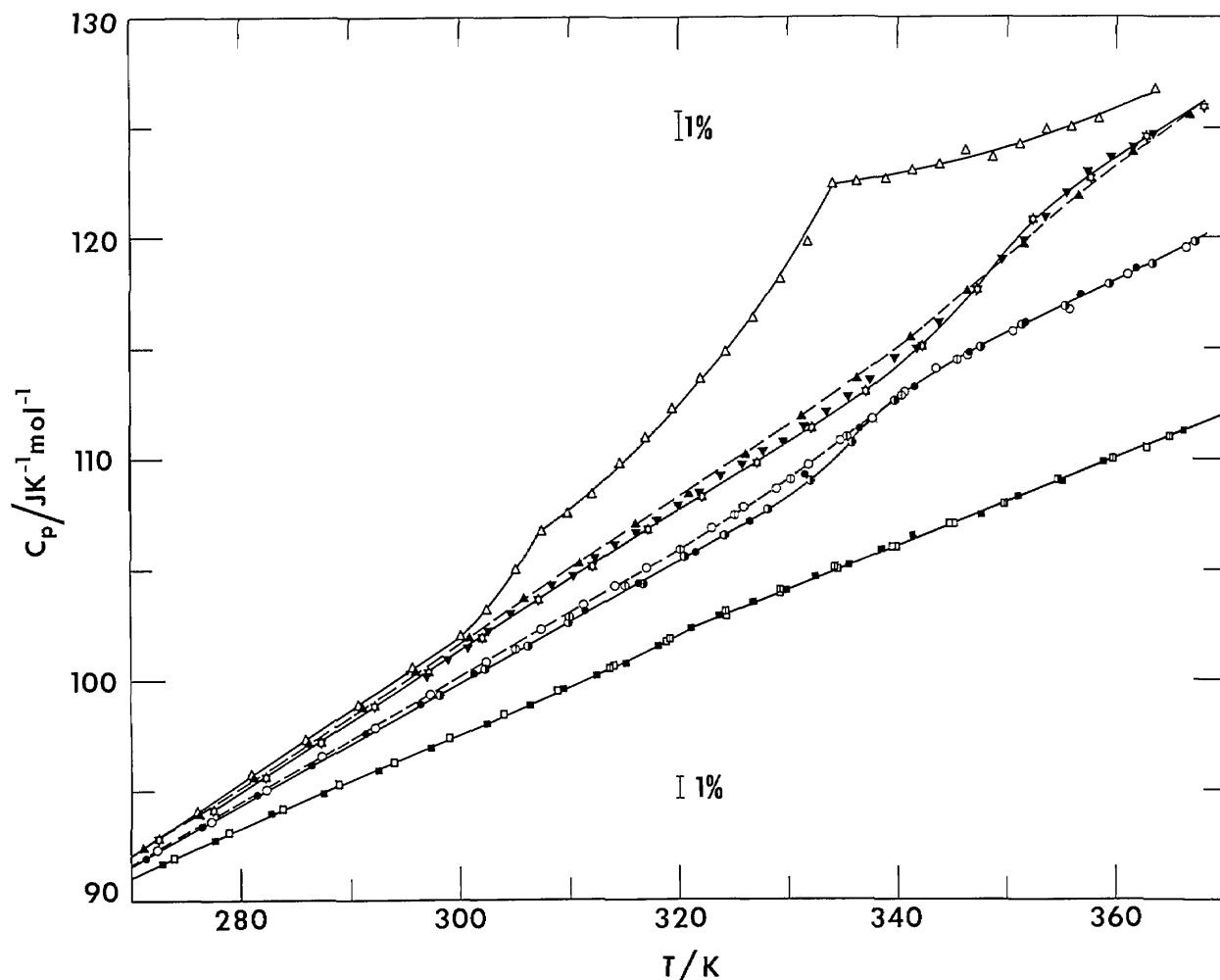


Fig. 2. Heat capacity of PCTFE and glass transition.

Film: Δ -F3, \blacktriangle -FQ, \blacktriangledown -FSC, \boxtimes -FRT.

Pellet: \circ -P1, \oplus -PQ3, \bullet -PA, \bullet -PSC.

Slow crystallized: \square -X1, \boxplus -XQ1, \blacksquare -XQ2.

lower than that in the present study. The authors also assigned a constant for a $C/T^{2.5}$ dependency for the range 4.3 to 6.7 K, which yielded values much closer to the values of the present study. The reasons for the different representations and the discrepancies among their graphical data and assigned constants are unknown.

It may also be noted that a mixture of PCTFE grease in silica gel was reported [36] to have heat capacities almost five times higher than the values reported by us and in Ref. [2] for PCTFE alone, in the temperature range from 1.8 to 4.5 K.

A region of C_p proportionality to T exists between 30 and 100 K, as seen in Figs. 1 and 4. The heat capacity function, C_p/T , curves in Fig. 4 also included a few DSC scans as discussed in later sections. Above 100 K, C_p of PCTFE still assumes a

relatively linear dependency on temperature, as seen by slowly varying C_p/T values. The linear dependency and proportionality may be a result of a relatively uniform distribution of vibrational frequencies from 100 to 1000 cm^{-1} , as estimated by Guttman [37].

From 100 to 260 K, heat capacities of all samples studied are surprisingly close to each other, within a spread of about 1%, regardless of a large variation in sample densities or crystallinities. The spread is greatest, about 3%, around 30 K. However, over the wide temperature region from 10 to 250 K, the heat capacity is higher for samples of higher crystallinity. Generally the C_p of most glassy materials is higher than the C_p of their crystalline counterpart. Although examples have been cited [38] to show that the C_p of the crystalline state is

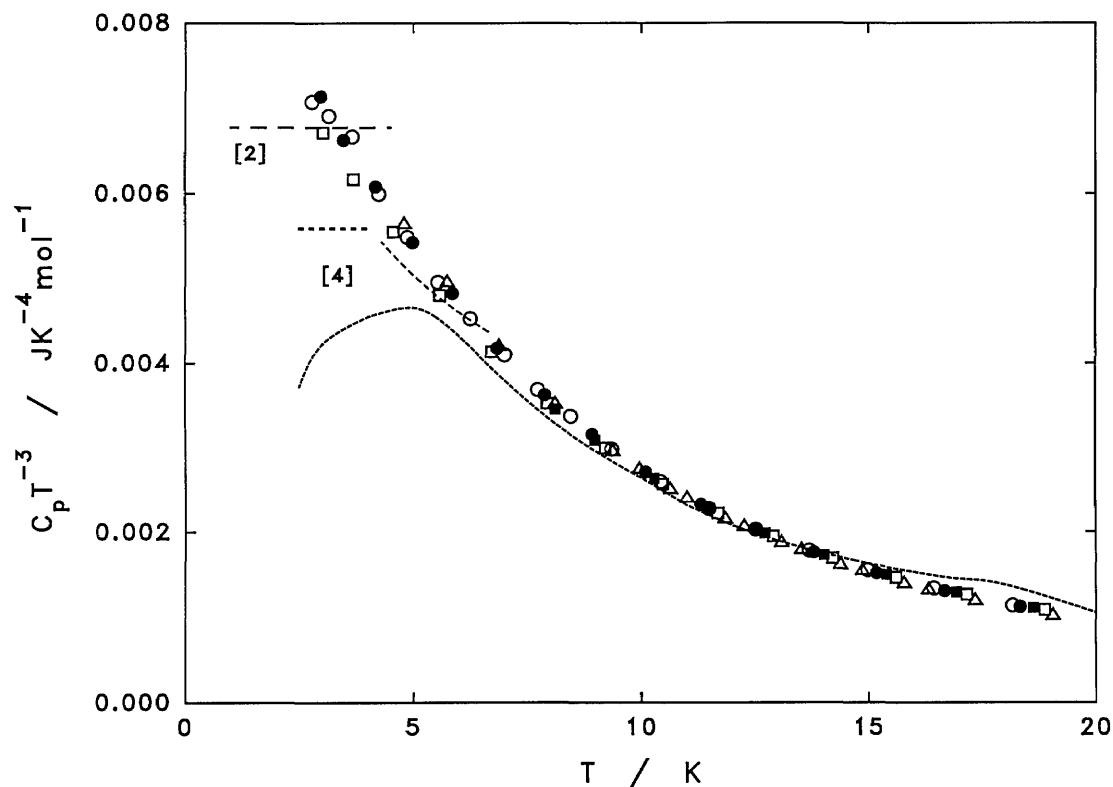


Fig. 3. Low temperature heat capacity of PCTFE.

Film: \triangle —F1, F3.

Pellet: \circ —PQ2, \bullet —PA.

Slow crystallized: \square —XQ2, \blacksquare —XSC.

Long dashes—Ref. [2]. Short dashes—Ref. [4].

higher than that of the vitreous state in certain ranges of temperature, the occurrence of this phenomenon over such a wide temperature range is rather unusual.

Above 260 K, the heat capacity depends strongly on the crystallinity or the complementary amorphous content. The lower the amorphous content, the lower the heat capacity, as normally expected of most semicrystalline materials.

Heat capacities of PCTFE above the cryogenic temperatures were only reported in two publications [1,3]. C_p values between 80 and 340 K of two PCTFE samples with crystallinities of 0.46 and 0.65, as determined by densities, were studied and smoothed data on the high density sample reported [3]. The reported values agree very well with that for our pellet sample series P1 and PQ. Similar to our findings, the authors found that the heat capacities for the two samples were the same within their experimental error of 0.3% at temperatures below 325 K. Their highest temperature measurement stops in the glass transition region, just as the transition is about to be completed. The authors

failed to detect or report a glass transition, except to note an indication of a positive d^2C_p/dT^2 . At 340 K, the heat capacity of the low density sample was about 0.8% higher than that of the denser sample.

Two samples of PCTFE, with crystallinities of 0.35 and 0.82 as determined from the heat of fusion, were studied with a differential calorimeter in a continuous heating mode for the temperature region from 0 to 250 °C [1]. No glass transition was reported for either of the two samples. The results from these two samples will be compared with DSC studies of the present work in later sections of this paper.

3.1.2 Glass Transition and Tacticity A glass-like transition was observed in all adiabatic calorimetric samples in the region from 320 to 350 K, as shown in Fig. 2. The intensity, as viewed by the magnitude of the sudden heat capacity rise, ΔC_p , is a function of the amorphous content. In the transition region, the spontaneous adiabatic temperature drifts were positive (exothermic) for quenched samples and negative (endothermic) for annealed samples. Although there appeared a small C_p dis-

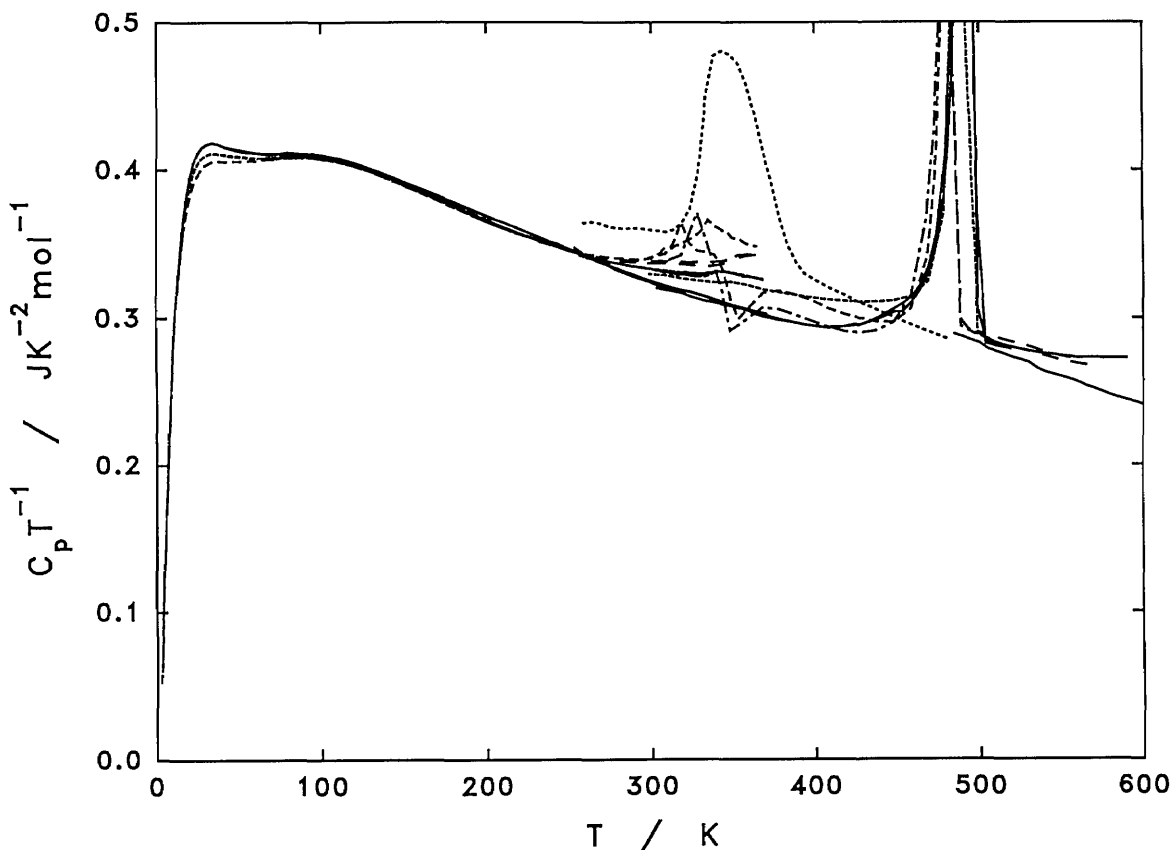


Fig. 4. Heat capacity function of PCTFE (adiabatic calorimetry and DSC).
 Solid lines—slow crystallized. Short dashes—pellet.
 Medium dashes—film (F1-F3). Long dashes—film (FAQ, FAS, FRT).
 Dots—wax.

continuity at just below 320 K for the highly crystalline sample X, the drifts were all within $1 \mu\text{K s}^{-1}$ after 15–20 min following the termination of energy input. Figure 5 shows the spontaneous drifts for the pellet sample P, with the annealing peak occurring at a higher temperature than the quenched peak.

Figure 6 shows the drift behavior for the film sample F. For the first heating of highly amorphous films, there appeared an endothermic dip in the drift at about 307 K. This may be a result of being left standing at the room temperature of 296 K for some time, after the films were quenched from the melt in ice water. The true drift peak for the glass transition probably was masked by the larger exothermic drifts due to crystallization occurring at temperatures above 310 K. Subsequent to the crystallization and stabilization of the films for a long time at 370 K, normal drifts for the glass transition phenomenon appeared in the temperature range of 340–350 K, see Fig. 6. The heat capacity behavior of the film after the stabilization process lay in be-

tween that of the pellet and the first heating of the films, see Fig. 2.

The variation of the glass transition of PCTFE as a function of crystallinity contradicts the commonly perceived idea that the glass transition temperature increases with crystallinity. Except for the highly amorphous quenched film, where the glass transition may be very wide and the true center of the glass transition was not observed, T_g appears to be lower for lower amorphous content. One plausible explanation for this phenomenon is that in the highly crystalline sample X, the remaining 10% (approximately) of amorphous content consists of mainly uncrystallizable low tactic or atactic portions of the polymer, and therefore the glass transition temperature appears near the low end of the glass transition range, as observed in the highly amorphous quenched film F.

The variation of the glass transition temperature as a function of crystallinity is shown in Fig. 7, where results from dilatometric [7,39] and dielectric [7] studies are also included. Earlier dilatomet-

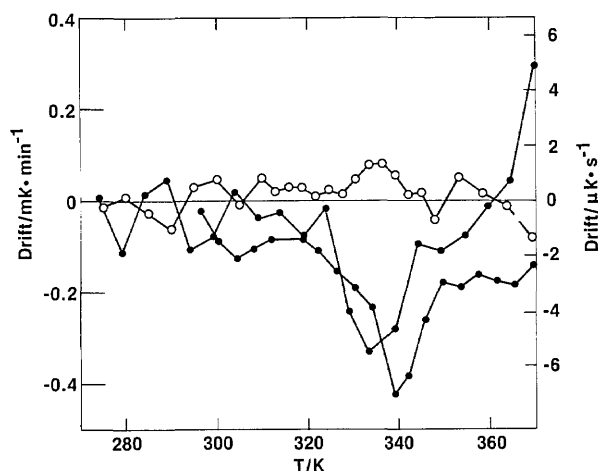


Fig. 5. Adiabatic temperature drift of pellet.
○—quenched. ●—annealed.

ric studies [6] of samples with densities of 2.116 and 2.165 g cm⁻³ suggested a glass transition temperature of 325 K which was relatively invariant with crystallinity.

3.2 Differential Scanning Calorimetry

About fifty DSC samples were taken from PCTFE samples of the same batches as the samples for adiabatic calorimetry, plus the original powder, films made from pellets, a manufactured tubing, and a low molecular weight wax. These DSC samples were subjected to various thermal treatments to show the dependency on the thermal history, such as annealing, quenching, and slow cooling. The influence of mechanical deformation was also studied. It is not feasible to show all the results of some 300 DSC runs in any detail except to make a summary here. A few of the typical runs, especially the first heatings of quenched samples, are shown as heat capacity functions in Fig. 4, as well as heat capacity curves in Fig. 11 in a later section. Except for the low molecular weight wax, the results on all other PCTFE samples, whether they were composed of pellet, powder or manufactured tubing, showed nearly identical behaviors as dictated by the thermal history after melting.

The low molecular weight Kel-F 200 Wax, showed a broad melting region from 305 to 400 K, with a peak at 350 K and a heat of fusion of 15 ± 1 J g⁻¹. The units of per gram instead of per mole are used here for convenience. The liquid heat capacity appeared to connect reasonably well (within 1%) to the adiabatic data for quenched film above its T_g and is slightly lower than the DSC liquid heat

capacity above the T_m of the high molecular weight PCTFE. Upon cooling, crystallization starts around 375 K with a exothermic maximum at about 352–355 K. The wax showed some instability at temperatures above 510 K.

The following summarizes the DSC observations on various forms of pellet, powder and film samples with different thermal histories. The observations included glass transition, crystallization, crystalline reorganization and fusion.

3.2.1 Glass Transition Temperature Except for the highly crystalline sample X where the small ΔC_p is difficult to observe by DSC, glass transition temperatures as depicted by a C_p discontinuity were also observed by DSC in the temperature range of 330–360 K, in similar magnitudes of ΔC_p as that observed by adiabatic calorimetry. The observation on the sample P was shown in Fig. 4 as an example. The slight increase in the observed glass transition temperature is due to the kinetic nature of the glass transition and the dynamic nature of the DSC measurement.

In order to improve the thermal conductivity and thus the consistency of sample temperature with the indicated DSC temperature, film samples were scanned as they were immersed in silicone oil. The T_g of films held overnight at 370 K was found to be in the range of 355 to 360 K. Only if the cooling rate was below 0.1 K/min or if the sample was annealed at 340 K for some time, did the transition range become narrower with a small relaxation peak at 360 to 375 K. Samples cooled at higher rates show a broader transition range of about 30 K.

For high amorphous content samples, apparent endothermic peaks occurred at about 320 K for the first heating of film sample F and films quenched from molten pellets KF-6060. A manufactured thin tubing of 0.11 mm thickness, left at room temperature for about 18 years, was scanned to reveal an even larger endothermic peak at 329 K, see Figs. 4 and 11. The onset of these endothermic peaks were the result of the rapid rise of C_p in the glass transition region, as seen by the adiabatic calorimetry, where spontaneous effects and crystallization effects were largely eliminated to reveal the underlying instantaneous lattice heat capacities.

However the nature of these peaks was rather complicated. The complexity could arise from a variety of origins, such as the glassy relaxation peak, the crystalline reorganization peak as described in a later section, or the termination of the C_p rise by the onset of the crystallization exotherm.

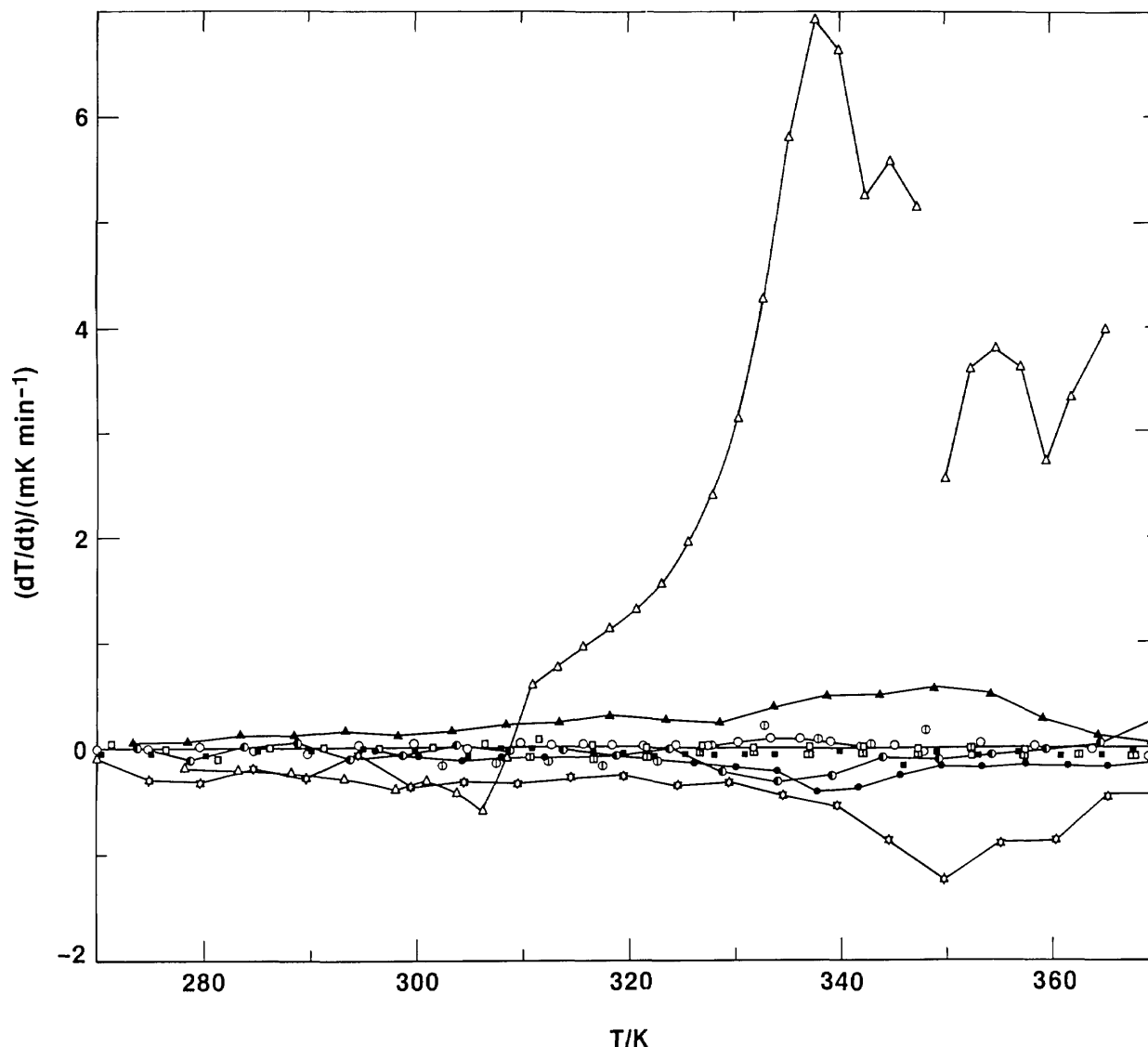


Fig. 6. Adiabatic temperature drift of film.

Film: Δ -F3, \blacktriangle -FQ, \blacktriangledown -FSC, \star -FRT.

Pellet: \circ -P1, \oplus -PQ3, \odot -PA, \bullet -PSC.

Slow crystallized: \square -X1, \boxplus -XQ1, \blacksquare -XQ2.

3.2.2 Crystallization Crystallization of quenched films observed at a scan rate of 10 K min^{-1} started near 335 K with an exothermic maximum at about 355 K , Figs. 4 and 11, regardless of whether the film was quenched from the melt to room temperature water, icy water, or an acetone-dry ice mixture at 195 K . The crystallization exotherm for the films was on the order of 3 J g^{-1} . Upon further heating, melting points for the first heating of quenched films were observed at 481 – 482.5 K with heats of fusion of 10.5 – 12.7 J g^{-1} . The slower adiabatic calorimetry indicated the onset of crystallization for the quenched films near 310 K

with a maximum rate near 340 K by the observations of adiabatic temperature drifts, Fig. 6.

A manufactured PCTFE tubing of 0.11 mm wall thickness, left at room temperature for 18 years, showed a crystallization onset at about 325 K and a maximum at about 350 K with a heat of crystallization of about 5 J g^{-1} during the first heating. Further heating produced a melting point at 484 K with a heat of fusion of 16.3 J g^{-1} . After cooling at -10 K min^{-1} from the melt with a heat of crystallization of 19 J g^{-1} , the melting point is increased to 488 K with a heat of fusion of 19.3 J g^{-1} . Although during the first heating of the tubing, it

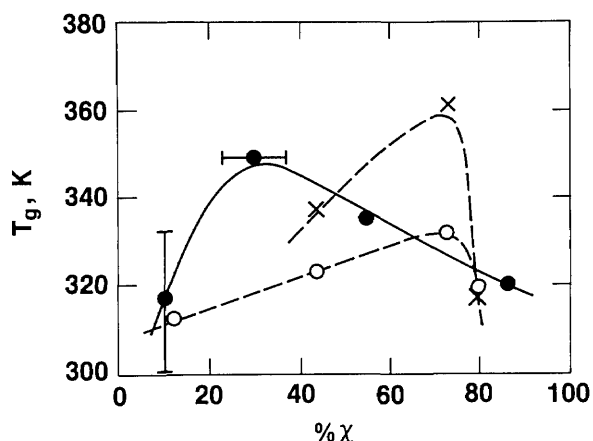


Fig. 7. Glass transition temperature as a function of crystallinity. ●—this work. ○—dilatometric [7,36]. ×—dielectric [7].

indicated a greater extent of crystallization than the films that we prepared, after the melting, the tubing behaved rather similarly to the samples made from either the pellets or from the powder.

The heat of crystallization of highly quenched films was much less than the subsequent heat of fusion. Therefore these highly amorphous films and the thin tubing were not completely amorphous but initially contained a certain crystallinity.

A film made from the powder, heated to 633 K and then quenched in water at room temperature, was studied for any stress-induced crystallization. It however behaved similar to films without any mechanical treatment. A strip of the film was drawn to break at about 50% elongation at room temperature. The 6 mm strip formed a neck of about 4 mm in width. A DSC scan of the neck area indicated a relatively large peak at 311 K, followed by a crystallization exotherm with a maximum at 352 K. The crystallization continued at temperatures above 410 K. The sample was cooled at 440 K. Upon reheating the sample, crystallization started again at 465 K. This sample also showed reorganizational peaks at 316 and 354 K, for annealing at room temperature and 335 K, respectively. The melting point of this sample was at 487 K. The untreated film from the same batch showed reorganizational peaks of 310 and 345 K for room temperature and 345 K annealing, a crystallization exotherm maximum at 356 K and a melting point of 483 K.

3.2.3 Reorganization of Crystallites The melting range for PCTFE is very wide, indicating a wide distribution of crystallite sizes and perfection. If a partially crystalline sample, obtained by a smooth

continuous cooling procedure, was left standing at any temperature above 240 K for some time, the DSC thermogram would show a small dip at the annealing temperature and a small endothermic peak at about 20 K above the annealing temperature, Fig. 8. The dip in the DSC curve was not an exothermic phenomenon, but was caused by a slight depletion of the crystallite population that might be melting in the temperature region of concern. The small peak just above the annealing temperature was the result of the melting of the additional crystallite population from a previously existing smooth distribution. The small humps from annealing at temperatures above 400 K are more difficult to detect due to the superimposition onto the rapid rise of the thermogram of the main melting peak.

A more dramatic demonstration of this phenomenon was to create a sample with multiple small melting peaks. A film sample was first annealed at 400 K overnight and then cooled to lower temperatures at a rate of 10 K/min. The smooth cooling procedure was successively interrupted and the sample was annealed at 360, 320, and 280 K for 2.5 h, and finally at 240 K overnight. Upon heating of this sample, small humps were observed at 268, 298, 341, 377, and 430 K, e.g., at about 20 to 30 K above the annealing temperatures. Figure 8 shows the results from this demonstration, as well as from many observations with a single annealing temper-

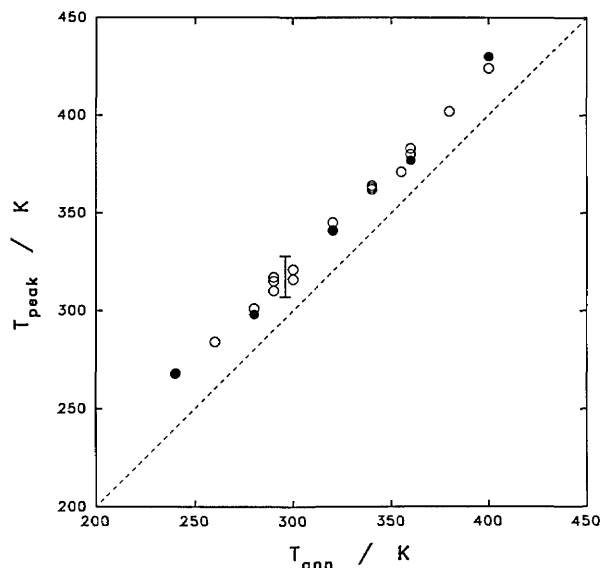


Fig. 8. Reorganization peak temperature as a function of annealing temperature.

●—multiple peaks. ○—individual peaks.
I—room temperature annealing.

ature. Non-smooth distributions of crystallite population in partially crystalline polymers with a wide (over 100 K) range of melting leading to multiple melting peaks have been observed in other polymers [40,41].

Both the position and the intensity of this reorganization peak were also functions of annealing time, Fig. 9. The reorganizational peak disappears if the sample is re-scanned immediately after a smooth cooling process. For samples crystallized at 400 K and then annealed at a room temperature of 296 K, the peak temperature varied from 307 to 320 K by annealing for a few minutes to several months. The peak height, as judged from the re-scan, rose quickly with annealing time and then apparently leveled off after about 10 h at a level near $0.02 \text{ J K}^{-1} \text{ g}^{-1}$ or $2 \text{ J K}^{-1} \text{ mol}^{-1}$.

The increase of the peak temperature of the original film (including the manufactured tubing) appeared to have the same functionality as the increase of the peak temperature of the film after crystallization at 400 K. The commercially produced PCTFE tubing of 0.11 mm thickness yielded a peak at 328 K after standing at room temperature for 18 years. However, the growth of the much larger peak by annealing the originally quenched film at room temperature was rather different from that of the crystallized film. The peak height varied from $0.05 \text{ J K}^{-1} \text{ g}^{-1}$ for annealing overnight at room temperature and to about 0.2 J g^{-1} after

room temperature storage for 18 yr. It is possible that some of the peak height is contributed by the relaxation phenomena of the glass transition.

3.2.4 Melting Point and Heat of Fusion The melting temperature of PCTFE was not well defined and the major portion of the melting occurred over a wide temperature region of over 50 K. The usual practice for the determination of a sharp melting point in power-compensated type of DSC, such as the instrument used here, is to estimate the onset temperature. The temperature difference between the peak and the onset for a sharp first order transition is a function of the sample size. However, the peak temperature for the broad melting of PCTFE was found to be relatively insensitive to the heating rate and the amount of sample used in the sample capsule. Therefore the peak temperature is chosen as the representative melting point, T_m , for the sample.

For low crystallinity samples consisting of quenched films or manufactured tubing, additional crystallization occurred above 335 K as the samples were scanned for the first time to their melting points. Melting points and heats of fusion for the first heating of quenched film were observed at 481–482.5 K with heats of fusion of $10.5\text{--}12.7 \text{ J g}^{-1}$. The tubing gave a T_m of 484 K with ΔH_m of 16.3 J g^{-1} . As the energy release during the crystallization was about $3\text{--}5 \text{ J g}^{-1}$, the original film or tubing before the additional crystallization would have yielded a heat of fusion of $7\text{--}11 \text{ J g}^{-1}$.

Cooling the melt, regardless of the sample origin, at a rate of $5\text{--}40 \text{ K min}^{-1}$ produces T_m of around 486–489 K and a heat of fusion around $15\text{--}20 \text{ J g}^{-1}$, similar to most of the pellet or powder PCTFE samples measured in as-received condition. Samples fast-cooled in DSC at an indicated rate of 320 K min^{-1} also yielded T_m around 487 K, without the 315 K peak and the subsequent recrystallization at around 355 K. Thus the true cooling rate in the DSC was far less than that indicated.

For slow-crystallized samples, the melting points observed were about $494 \pm 1 \text{ K}$ with a heat of fusion on the order of $29\text{--}30 \text{ J g}^{-1}$. A sample held at 470 K overnight also gave a T_m of 492 K. The heat of fusion from DSC, as estimated by integrating the peak area above a baseline drawn from the solidus heat capacity at about 430 K to the liquidus heat capacity at about 500 K, is a lower bound of the value. The results for the heat of fusion and melting point measurements for various PCTFE samples are shown in Fig. 10.

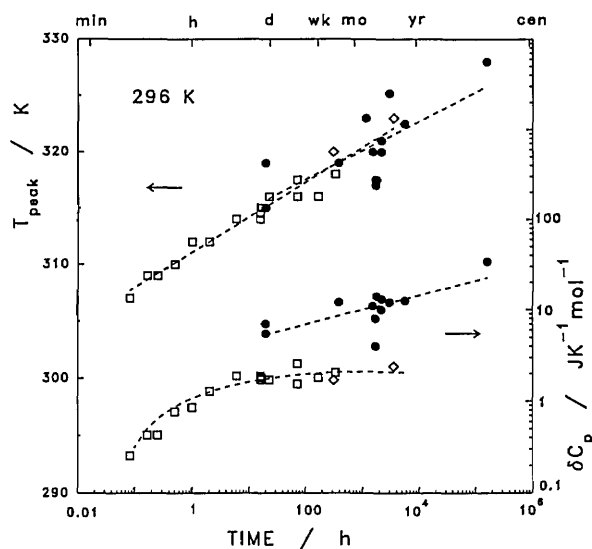


Fig. 9. Reorganization peak temperature and intensity as functions of annealing time.

- , ◇—quenched films after crystallized at 400 K.
- original films and tubing before heating to 400 K.

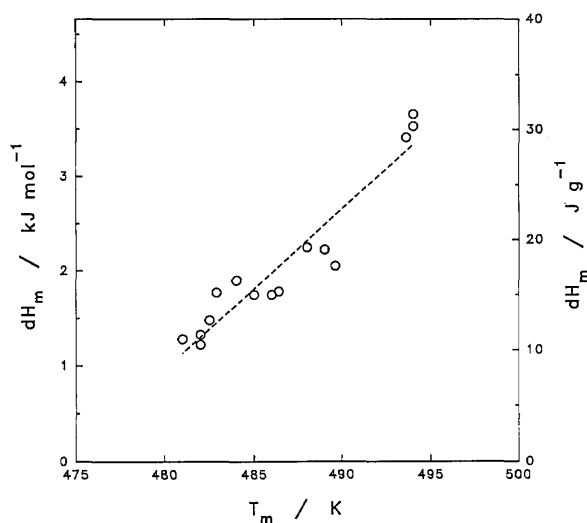


Fig. 10. Heat of fusion and melting point of PCTFE.

Based on the densities, the results of DSC measurements could only be extrapolated to about 35 J g^{-1} for the heat of fusion for the pure crystalline phase. A correction to the peak area, as based on the heat capacities of the crystalline and liquid phases as described in a later section and Fig. 11, would increase the heat of fusion value of the pure crystalline phase by 5 J g^{-1} . The observed value for heat of fusion may be a lower bound for bulk crystals, due to the surface energy contributions from small crystallite sizes in these samples. We believe that a heat of fusion of about $40 \pm 5 \text{ J g}^{-1}$ for the pure crystalline phase at an equilibrium melting point of 497 K [42] is perhaps a reasonable estimate.

Reference [1] reported heat of fusion values of $15.1 \pm 0.4 \text{ J g}^{-1}$ for air-quenched PCTFE and $35.1 \pm 0.8 \text{ J g}^{-1}$ for a slow-cooled sample. The degrees of crystallinity for the two samples were esti-

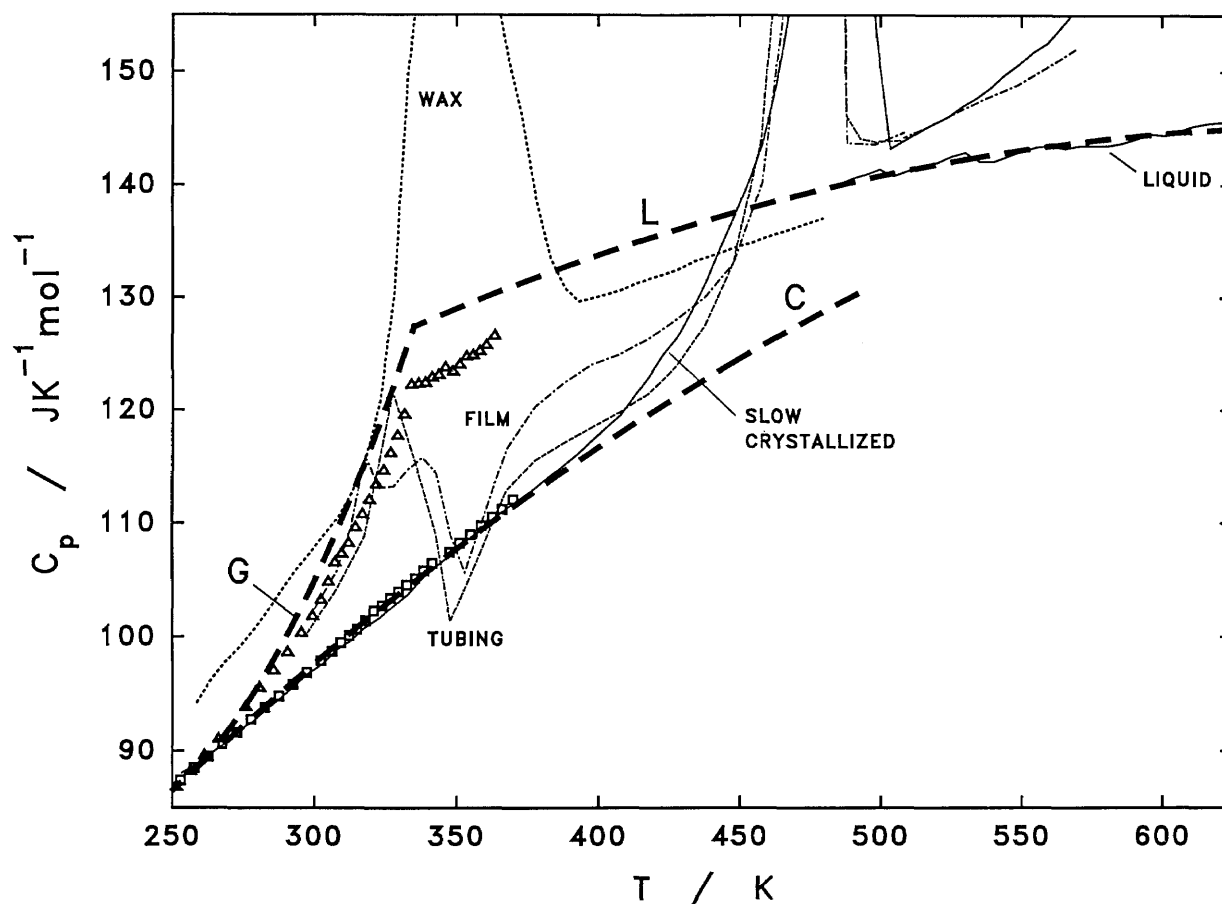


Fig. 11. Estimated heat capacity behavior of PCTFE crystal, glass, and liquid.

Heavy dashes—estimated heat capacity for PCTFE crystal (C), glass (G), and liquid (L).

Adiabatic measurements: Δ —F3, \square —XQ2.

DSC measurements: wax, film (first heating), tubing (first heating), slow-crystallized and liquid (short scan) as labeled.

mated as 0.35 and 0.82, respectively, by using a value of $43.1 \pm 2.5 \text{ J g}^{-1}$ as the heat of fusion of "pure" crystalline PCTFE from solubility studies [43]. Reference [1] also gave a value of $46.9 \pm 4.2 \text{ J g}^{-1}$ as the heat of fusion for the pure crystals estimated by a method briefly described as volumetric [44]. A value of 75.7 J g^{-1} was reported for the heat of fusion by another solubility study [45], which we judged to be too high in comparison to all other studies.

Using the heat of fusion of the pure crystalline phase as the basis, the quenched film or the tubing would have a crystalline content of about 25% before any additional crystallization set in at temperatures above 350 K. These residual crystallinities were small crystallites which were not detected by optical means and only gave a broad halo in x-ray powder patterns.

3.3 Thermodynamic Properties

3.3.1 Heat Capacity of PCTFE Crystal, Glass, and Liquid In the determination of the high temperature heat capacity of PCTFE by DSC, a peculiar behavior was found. At temperatures above 500 K, heat capacities estimated from continuous scanning runs as calibrated with similar runs with sapphire discs became progressively higher than that obtainable by the short interval (5–10 K) scan or integration. This peculiar behavior was observed not only with the current PCTFE samples but also on heat capacity estimations of samples of teflon and copper, when compared with literature values. All results indicated deviations between the continuous scan and short interval scan of less than 0.5% at 430 K that increased to about 5% at 550 K. The values measured by the short interval integration method on copper or teflon were however near 0.2% of the literature values throughout the entire temperature range. Therefore the short interval integration values are considered to be close to the true heat capacity values, and the long or continuous scans are to be used only for the estimation of heats of fusion and melting points. The reason for this discrepancy is unknown. It may be due to instrumental artifacts or due to the deterioration or contamination of the sample holder assembly, and/or chemical reactions at high temperatures.

The heat capacity of crystalline PCTFE below 300 K is considered to be the same as that measured for the highly crystalline sample X, Table 4. As the differences between the glassy and crystalline phases are rather small below 300 K, no adjustment is applied to adjust for the near 10%

amorphous content. Above 300 K, C_p of the crystalline phase is represented by a curve as shown in Fig. 11, which is a smooth extension of the heat capacity behavior below 300 K. There is a slight reduction in the C_p corresponding to the contribution from approximately 10% amorphous phase to the ΔC_p for the glass transition.

The heat capacity of amorphous PCTFE in the glassy state below 250 K is considered to be the same as the quenched film before heating to temperatures above the room temperature. As the differences between the glassy and crystalline phases are rather small below 300 K, no adjustment is applied for any crystalline content in the quenched films. Above 250 K and extending to the supercooled liquid state, the heat capacity of the amorphous PCTFE is obtained by adding 25% of the ΔC_p to the measured heat capacity of the quenched

Table 4. Thermodynamic functions of crystalline PCTFE (units in J, K, and mol. 1 mol = 116.47 g)

T K	C_p $\text{J K}^{-1} \text{ mol}^{-1}$	$H - H_{0,r}$ J mol^{-1}	S $\text{J K}^{-1} \text{ mol}^{-1}$	$-(G - H_{0,r})$ J mol^{-1}
5	0.65	0.92	0.25	0.33
10	2.71	8.96	1.28	3.88
15	5.26	28.83	2.86	14.07
20	7.84	61.64	4.73	32.97
30	12.43	163.95	8.82	100.50
40	16.46	308.19	12.94	209.26
50	20.48	492.90	17.04	359.17
60	24.51	717.79	21.13	550.03
70	28.60	983.28	25.22	781.76
80	32.72	1289.8	29.30	1054.3
90	36.82	1637.6	33.39	1367.8
100	40.84	2026.0	37.48	1722.2
120	48.43	2919.9	45.61	2553.3
140	55.51	3961.8	53.63	3546.0
160	61.96	5137.2	61.47	4697.2
180	68.05	6437.9	69.12	6003.3
200	73.82	7857.2	76.59	7460.7
220	79.24	9388.4	83.88	9065.7
240	84.27	11024	91.00	10815
260	88.91	12757	97.93	12704
273.15	91.78	13945	102.72	14113
280	93.31	14579	105.01	14825
298.15	97.22	16310	111.00	16785
300	97.64	16489	111.60	16991
320	101.81	18485	118.04	19288
340	105.79	20561	124.33	21712
360	109.61	22716	130.49	24260
380	113.24	24945	136.52	26931
400	116.71	27246	142.41	29720
420	119.99	29613	148.19	32626
440	123.11	32045	153.85	35647
460	126.05	34537	159.38	38780
480	128.81	37087	164.81	42022
497	131.03	39262	169.33	44895

films, as shown in Fig. 11. As based on DSC measurements of heats of fusion, the quenched films may originally contain a crystallinity of about 0.25, before additional crystallization starts at temperatures just above the glass transition temperature.

The liquidus heat capacity, from 335 K in the supercooled liquid state to 620 K in the melt, was obtained by combining the adiabatic measurement of the quenched film from 335 to 370 K adjusted for the ΔC_p due to a residual crystalline content in the original film and the DSC measurements of molten PCTFE above 495 K using the short interval scan as mentioned earlier. The trend of the liquidus C_p behavior of a low molecular weight wax as observed with DSC was used as a guide to the functionality between the two measurements. The assigned liquidus heat capacity is also shown in Fig. 11.

3.3.2 Thermodynamic Functions and Residual Entropy The thermodynamic functions for the crystalline PCTFE are listed in Table 4. The functions are calculated based on the estimated crystalline heat capacity as mentioned above, with the assumption that there is no residual entropy at 0 K for the crystalline phase. If there is any residual entropy for the crystal, the free energy term should be corrected by an amount equal to TS_0 .

The thermodynamic functions of the amorphous phase and the liquid are listed in Table 5. These functions are calculated based on the estimated amorphous and liquid heat capacity as mentioned above. The integration for the enthalpy and entropy are based on the zero-point enthalpy and entropy of the glass rather than the crystal. As the amorphous phase is expected to have a residual entropy at 0 K, the free energy is not calculated.

The heat of fusion of the crystalline state is considered to be about 40 J g^{-1} or 4.7 kJ mol^{-1} at 497 K. The corresponding entropy of fusion is $9.3 \text{ J K}^{-1} \text{ mol}^{-1}$. These values will yield $(H_{\text{liq}} - H_x)_{497}$ of 44.0 kJ mol^{-1} and $S_{497, \text{liq}}$ of $179.5 \text{ J K}^{-1} \text{ mol}^{-1}$. Then $(H_{\text{gl}} - H_x)_0$ will be about 1.6 kJ mol^{-1} and the residual entropy for the amorphous PCTFE at 0 K, $S_{0, \text{gl}}$, will be about $2.0 \text{ J K}^{-1} \text{ mol}^{-1}$. This $S_{0, \text{gl}}$ value, although reasonable, is smaller than the usual observation mentioned for a collection of reliable residual entropies [26,32] of around $(R \ln 2)/2$ or 3 J K^{-1} per each chain atom or bead. The smaller residual entropy may be the result of the disorder existing in the crystalline PCTFE or a low estimation of the heat of fusion of the PCTFE crystal.

Table 5. Thermodynamic functions of amorphous and liquidus PCTFE (Units in J, K, and mol. 1 mol = 116.47 g)

T K	C_p $\text{J K}^{-1} \text{ mol}^{-1}$	$H - H_{0, \text{gl}}$ J mol^{-1}	$S - S_{0, \text{gl}}$ $\text{J K}^{-1} \text{ mol}^{-1}$
5	0.69	0.95	0.26
10	2.74	9.20	1.32
15	5.16	28.90	2.88
20	7.59	60.82	4.70
30	12.09	159.65	8.65
40	16.24	301.47	12.70
50	20.30	484.16	16.60
60	24.39	707.57	20.82
70	28.54	972.18	24.89
80	32.71	1278.4	28.98
90	36.83	1626.2	33.07
100	40.84	2014.7	37.16
120	48.39	2908.0	45.28
140	55.04	3943.5	53.25
160	61.34	5107.8	61.01
180	67.37	6395.3	68.59
200	73.14	7800.9	75.99
220	78.65	9319.2	83.22
240	83.90	10945	90.29
260	88.89	12673	97.20
273.15	93.00	13869	101.68
280	95.59	14514	104.02
298.15	103.93	16323	110.27
300	104.90	16515	110.92
320	116.81	18729	118.06
335	127.43	20559	123.65
340	127.97	21198	125.54
360	130.04	23778	132.91
380	131.98	26399	139.99
400	133.79	29056	146.81
420	135.46	31749	153.38
440	137.01	34474	159.72
460	138.42	37229	165.84
480	139.70	40010	171.76
497	140.68	42393	176.64
500	140.84	42816	177.48
520	141.86	45643	183.03
540	142.74	48489	188.40
560	143.49	51352	193.60
580	144.10	54228	198.65
600	144.59	57115	203.54
620	144.94	60010	208.29

4. Conclusion

One advantage of adiabatic calorimetry over DSC is the ability to detect the direction and to separate the effects of relatively long term spontaneous thermal events originating in the sample. The DSC measurement provides only a single overall heat-flow thermogram as a function of time during a scan. The adiabatic calorimetry allows the extraction of short term equilibrium heat capacities such

as contributions from lattice vibrations from long term spontaneous thermal events such as relaxation and crystallization, by observing the adiabatic temperature drifts as a function of time. Magnitudes, directions, and locations of the spontaneous event may also be measured by adiabatic calorimetry. Differential scanning calorimetry is however more advantageous if large numbers of small-size samples need to be tested at a lower precision.

The lattice heat capacities of PCTFE samples of different crystallinities clearly show a glass transition in the region from 320 to 350 K, heretofore undetected by other thermal measurements. The spontaneous drifts observed in adiabatic calorimetry have also confirmed the glass-like relaxation phenomenon, which give rise to a positive temperature drift for quenched glasses and negative drift for annealed glasses.

The glass transition temperature is, however, lowered for samples of higher crystallinity. This may be caused by the rejection of the uncrystallizable portion of a polymer chain, which itself may have a lower glass transition temperature than the overall glass transition temperature as contributed by all different structures.

Although a few approximations were applied to derive the thermodynamic functions for PCTFE crystal, glass, and liquid, the small residual entropy of the glass may be the result of a disorder in the crystalline structure. Heat capacities of the highly crystalline sample behaved almost identically to that of a low crystallinity sample in the cryogenic temperature region down to 2.5 K, where a region for the Debye T^3 law was not yet reached.

The melting range of PCTFE is very wide, with the majority of the melting occurring in a range of 60 K. For ordinary samples with a smooth cooling history and having a crystallinity around 0.5, annealing at any temperature above 240 K may cause a reorganization into a non-smooth distribution of crystallite sizes. By successively annealing at lower temperatures, a sample with more than five melting peaks was prepared.

5. References

- [1] J. D. Hoffman, *J. Am. Chem. Soc.* **74**, 1696 (1952).
- [2] W. Reese and J. E. Tucker, *J. Chem. Phys.* **43**, 105 (1965).
- [3] W. K. Lee, P. C. Lau, and C. L. Choy, *Polymer* **15**, 487 (1974).
- [4] B. Terziiska, H. Madge, and V. Lovtchinov, *J. Thermal Anal.* **20**, 33 (1981).
- [5] L. Mandelkern, G. M. Martin, and F. A. Quinn, *J. Res. Natl. Bur. Stand. (U.S.)* **58**, 137 (1957).
- [6] J. D. Hoffman and J. J. Weeks, *J. Res. Natl. Bur. Stand. (U.S.)* **60**, 465 (1958).
- [7] J. D. Hoffman, G. Williams, and E. Passaglia, *J. Polym. Sci.* **C14**, 173 (1966).
- [8] E. Sacher, *J. Polym. Sci., Polym. Lett. Ed.* **18**, 333 (1980).
- [9] J. M. Crissman and E. Passaglia, *J. Polym. Sci.* **C14**, 237 (1966).
- [10] S. S. Chang, *Proc. 7th Symp. Thermophys. Prop., ASME*, **75** (1977).
- [11] S. S. Chang, *J. Polym. Sci.* **C43**, 43 (1973).
- [12] H. S. Kaufman, *J. Am. Chem. Soc.* **75**, 1477 (1953).
- [13] L. G. Roldan and H. S. Kaufman, *Norelco Reporter* **10**, No. 1, 11 (1963).
- [14] Z. Mencik, *J. Polym. Sci., Polym. Phys. Ed.* **11**, 1589 (1973).
- [15] K. F. Sterrett, D. H. Blackburn, A. B. Bestul, S. S. Chang, and J. Horman, *J. Res. Natl. Bur. Stand. (U.S.)* **69C**, 19 (1965).
- [16] S. S. Chang, *J. Res. Natl. Bur. Stand. (U.S.)* **80A**, 669 (1976).
- [17] H. Diesselhorst, *Z. Instrumentkunde* **26**, 297 (1906).
- [18] S. S. Chang, *Rev. Sci. Instrum.* **40**, 822 (1966).
- [19] R. E. Bedford, M. Durieux, R. Muijwijk, and C. R. Barber, *Metrologia* **5**, 47 (1969).
- [20] H. Plumb and G. Cataland, *Metrologia* **2**, 127 (1966).
- [21] F. L. McCrackin and S. S. Chang, *Rev. Sci. Instrum.* **46**, 550 (1975).
- [22] H. Preston-Thomas, *Metrologia* **27**, 3 (1990).
- [23] S. S. Chang, *Proc. 7th Intl. Symp. Thermophys. Prop., ASME*, 83 (1977).
- [24] D. A. Ditmars, S. Ishihara, S. S. Chang, G. Bernstein, and E. D. West, *J. Res. Natl. Bur. Stand. (U.S.)* **87**, 159 (1982).
- [25] S. S. Chang and A. B. Bestul, *J. Res. Natl. Bur. Stand. (U.S.)* **75A**, 113 (1971).
- [26] S. S. Chang and A. B. Bestul, *J. Chem. Thermodyn.* **6**, 325 (1974).
- [27] J. C. Lasjaunias, *C. R. Acad. Sci. Ser. B* **269**, 763 (1969).
- [28] S. S. Chang, *Thermal Anal. Polym. Characterization*, E. A. Turi, ed., Heyden & Sons (1981) p. 98.
- [29] S. S. Chang, *J. Polym. Sci., Polym. Symp.* **71**, 59 (1984).
- [30] C. L. Choy, R. G. Hunt, and G. L. Salinger, *J. Chem. Phys.* **52**, 3629 (1972).
- [31] P. Zoller, D. L. Fehl, and J. R. Dillinger, *J. Polym. Sci., Polym. Phys. Ed.* **11**, 1441 (1973).
- [32] S. S. Chang and A. B. Bestul, *J. Chem. Phys.* **56**, 503 (1972).
- [33] S. S. Chang, *J. Res. Natl. Bur. Stand. (U.S.)* **82**, 9 (1977).
- [34] S. S. Chang, *J. Res. Natl. Bur. Stand. (U.S.)* **78a**, 387 (1974).
- [35] S. S. Chang, *J. Chem. Phys.* **79**, 6229 (1983).
- [36] R. J. Graves and H. W. White, *Cryogenics* **20**, 525 (1980).
- [37] C. M. Guttman, to be published.
- [38] S. S. Chang, J. A. Horman, and A. B. Bestul, *J. Res. Natl. Bur. Stand. (U.S.)* **71A**, 293 (1967).
- [39] A. H. Scott, D. J. Scheiber, A. J. Curtis, J. I. Lauritzen, Jr., and J. D. Hoffman, *J. Res. Natl. Bur. Stand. (U.S.)* **66a**, 269 (1962).
- [40] A. P. Gray and K. Casey, *J. Polym. Sci., Polym. Lett. Ed.* **2**, 381 (1964).
- [41] S. S. Chang, *Polym. Comm.* **29**, 138 (1988).
- [42] A. M. Bueche, *J. Am. Chem. Soc.* **74**, 65 (1952).
- [43] F. P. Price, *J. Chem. Phys.* **19**, 973 (1951).
- [44] J. D. Hoffman and J. J. Weeks, *J. Res. Natl. Bur. Stand. (U.S.)* **66A**, 13 (1962).
- [45] H. T. Hall, *J. Am. Chem. Soc.* **74**, 68 (1952).

About the authors: Shu-Sing Chang is a Research Chemist in the Polymers Division at NIST. James J. Weeks is a Research Chemist who retired from the National Bureau of Standards (now NIST). The National Institute of Standards and Technology is an agency of the Technology Administration, U.S. Department of Commerce.

Precipitation and Solubility of Calcium Hydrogenurate Hexahydrate

Volume 97

Number 3

May–June 1992

V. Babić-Ivančić,
H. Füredi-Milhofer, and
N. Brničević

Rudjer Bošković Institute,
Zagreb, Croatia

and

M. Marković¹

Rudjer Bošković Institute
and Faculty of Science,
University of Zagreb,
Zagreb, Croatia and
American Dental Association
Health Foundation,
National Institute of Standards
and Technology,
Gaithersburg, MD 20899

Solid phases formed in the quaternary system: uric acid–calcium hydroxide–hydrochloric acid–water aged for 2 months at 310 K were studied to determine conditions for calcium hydrogenurate hexahydrate, $\text{Ca}(\text{C}_5\text{H}_3\text{N}_4\text{O}_3)_2 \cdot 6\text{H}_2\text{O}$, precipitation. The precipitates were identified by chemical and thermogravimetric analyses, x-ray powder diffraction, infrared spectroscopy, light microscopy, and scanning electron microscopy. In the precipitation diagram the concentration region in which calcium hydrogenurate hexahydrate precipitated as a single solid phase was established.

The solubility of calcium hydrogenurate hexahydrate was investigated in the pH range from 6.2 to 10.1 at different temperatures. The total soluble and ionic concentration of calcium (atomic absorption spectroscopy and Ca-selective electrode), total urate concentration (spectrophotometry), and pH were determined in equilibrated solutions.

The data are presented in the form of tables and chemical potential diagrams. By using these data the thermodynamic solubility products of calcium hydrogenurate hexahydrate, $K_s = a(\text{Ca}^{2+}) \cdot a^2(\text{C}_5\text{H}_3\text{N}_4\text{O}_3^-)$, were determined:

$\text{p}K_s = 10.12 \pm 0.07$ at 288 K,
 $\text{p}K_s = 9.81 \pm 0.09$ at 298 K,
 $\text{p}K_s = 9.28 \pm 0.04$ at 310 K, and
 $\text{p}K_s = 9.01 \pm 0.03$ at 318 K.

The formation of calcium hydrogenurate hexahydrate crystals in urinary tract of patients with pathologically high concentrations of calcium and urates (hypercalciuria and hyperuricosuria) is possible.

Key words: calcium hydrogenurate hexahydrate; identification; precipitation; solubility; solubility product; urinary stone formation.

Accepted: April 2, 1992

1. Introduction

The formation of urinary stones of various composition (urolithiasis) is a painful and crippling pathological process in the urinary tract. The occurrence of stones containing pure uric acid, $\text{C}_5\text{H}_4\text{N}_4\text{O}_3$, H_2U , has been reported [1] but usually

urate calculi have a layer-like composition consisting of additional crystalline compounds, i.e., calcium oxalates, calcium phosphates, cystine, etc. [1,2]. It has been proposed that uric acid and/or sodium hydrogenurate may serve as templates for formation of calcium salts in renal stones [3-6]. Calcium urates have also been considered as possible constituents of urinary stones [7-9] but there is no evidence about them as separate solid phases. Gouty arthritis is another disease in which urates form pathological deposits [10].

¹ Author to whom correspondence should be addressed at Department of Physical Chemistry, Rudjer Bošković Institute, P.O. Box 1016, 41001 Zagreb, Croatia or American Dental Association Health Foundation, Paffenbarger Research Center, National Institute of Standards and Technology, Gaithersburg, MD 20899.

Because of their physiological relevance, the precipitation, dissolution, and solubility of anhydrous uric acid [11-14], uric acid dihydrate [14,15] and sodium hydrogenurate monohydrate [11,16-18] have been studied in detail. There is, however, a limited number of investigations on calcium urates. Only the thermodynamically stable calcium hydrogenurate hexahydrate, $\text{Ca}(\text{C}_5\text{H}_3\text{N}_4\text{O}_3)_2 \cdot 6\text{H}_2\text{O}$, $\text{Ca}(\text{HU})_2 \cdot 6\text{H}_2\text{O}$, has been prepared and characterized [19, 20] but no solubility data of this compound have as yet been reported.

In this paper we describe the formation of $\text{Ca}(\text{HU})_2 \cdot 6\text{H}_2\text{O}$ in the four component system: uric acid—calcium hydroxide—hydrochloric acid—water at physiological temperature (310 K). The solubility products of $\text{Ca}(\text{HU})_2 \cdot 6\text{H}_2\text{O}$ at 288, 298, 310, and 318 K are reported. These results should facilitate understanding of the possible precipitation of $\text{Ca}(\text{HU})_2 \cdot 6\text{H}_2\text{O}$ in a physiological environment.

2. Methods

2.1 Preparation and Identification

Calcium hydrogenurate hexahydrate was prepared by equilibrating commercial uric acid (Sigma Chemical²) with aqueous solutions of calcium hydroxide to which hydrochloric acid was added when necessary to adjust the pH. To ensure slow crystallization and recrystallization the samples were kept without agitation for several weeks in a nitrogen atmosphere. After completion of the reaction, crystals were examined in solution by an inverted light microscope (Leitz, Wetzlar), subsequently filtered and characterized by physicochemical and analytical methods. X-ray diffraction (XRD) patterns (Phillips x-ray diffractometer with proportional counter, using graphite monochromated $\text{CuK}\alpha$ radiation) were taken from moist precipitates and after extended air-drying. Infrared spectra ($4000-200\text{ cm}^{-1}$) were recorded as nujol mulls (Perkin Elmer, Model 580B spectrophotometer). Scanning electron micrographs (Cambridge Stereo Scan 600) were obtained from dried crystals. In some samples the chemical composition

² Certain commercial materials and equipment are identified in this paper to specify the experimental procedure. In no instance does such identification imply recommendation or endorsement by the National Institute of Standards and Technology or the ADA Health Foundation or that the material or equipment identified is necessarily the best available for the purpose.

was confirmed. Calcium was determined by atomic absorption spectroscopy (Jarel Ash) and gravimetry; carbon, hydrogen, and nitrogen by microanalysis, and content of water and purine by thermogravimetric analysis (Cahn RG electromicroanalytical balance, heating rate $2\text{ }^\circ\text{C}/\text{min}$ in air).

2.2 Solubility Determinations

Solubility determinations of $\text{Ca}(\text{HU})_2 \cdot 6\text{H}_2\text{O}$ were carried out (a) in the original supernatant after sample preparation and (b) in water and aqueous solutions of uric acid or calcium chloride.

(a) Freshly prepared $\text{Ca}(\text{HU})_2 \cdot 6\text{H}_2\text{O}$ crystals were reequilibrated with their respective supernatants by shaking them for 24 h at 310 K.

(b) Dried crystals were equilibrated at different temperatures (288, 298, 310, and 318 K) in triply distilled water and in uric acid or calcium chloride solutions by shaking them in a thermostated water bath for 24 h (at 288 and 298 K) or 3 h (at 310 and 318 K).

After equilibration, the concentration of total calcium (atomic absorption), ionic calcium (Ca-selective electrode), total urate (direct spectrophotometric determination at 285 nm [14]), and pH were determined in all supernatants and the solid phase was identified by XRD.

2.3 Processing of Solubility Data

Computation of ion activities and solubility product of $\text{Ca}(\text{HU})_2 \cdot 6\text{H}_2\text{O}$,

$$K_s = a(\text{Ca}^{2+}) \cdot a^2(\text{HU}^-) \quad (1)$$

was made by an iterative procedure using the experimentally determined concentrations of all species in equilibrated solutions and literature values of uric acid [13,15,21] and water [22,23] dissociation constants for different temperatures (Table 1).

Table 1. Dissociation constants of uric acid and water at different temperatures

Equilibria	pK				Ref.
	(288 K)	(298 K)	(310 K)	(318 K)	
1. $\text{H}_2\text{U} \rightleftharpoons \text{H}^+ + \text{HU}^-$	5.65	5.61	5.44	5.34	[13,15]
2. $\text{HU}^- \rightleftharpoons \text{H}^+ + \text{U}^{2-}$	9.15	9.15	10.51	10.51	[21]
3. $\text{H}_2\text{O} \rightleftharpoons \text{H}^+ + \text{OH}^-$	14.35	13.99	13.61	13.39	[22,23]

For calculating the activity coefficients, γ , the Davies modification of the extended Debye-Hückel equation was used:

$$\log \gamma = -Az^2(\sqrt{I}/(1+\sqrt{I}) - 0.2I) \quad (2)$$

where z is valence charge of the ion and A is the Debye constant having the values of 0.5002, 0.5115, 0.5242, and 0.5296 for 288, 298, 310, and 318 K, respectively [23,24]. Ionic strength, I , was defined as $I = 0.5 \sum cz^2$ where c is the concentration of corresponding ionic species.

The solubility data were recalculated in terms of the ion activity products $a(\text{Ca}^{2+}) \cdot a^2(\text{OH}^-)$ and $a(\text{H}^+) \cdot a(\text{HU}^-)$. The following treatment, based on considerations of the chemical potentials of the components in equilibrium with the solid phase [25,26] was then applied:

Multiplying both sides of Eq. (1) by $a^2(\text{H}^+) \cdot a^2(\text{OH}^-)$ yields

$$\begin{aligned} & [a(\text{H}^+) \cdot a(\text{HU}^-)]^2 \cdot [a(\text{Ca}^{2+}) \cdot a^2(\text{OH}^-)] \\ & = K_s \cdot K_w^2. \end{aligned} \quad (3)$$

Taking logarithms and rearranging gives

$$\begin{aligned} & \log a(\text{H}^+) \cdot a(\text{HU}^-) \\ & = 0.5 \log a(\text{Ca}^{2+}) \cdot a^2(\text{OH}^-) + 0.5 \log K_s \cdot K_w^2. \end{aligned} \quad (4)$$

Equation (4) describes a straight line whose slope is 0.5 if the composition of the solid phase is $\text{Ca}(\text{HU})_2 \cdot 6\text{H}_2\text{O}$.

3. Results and Discussion

3.1 Precipitation and Characterization of $\text{Ca}(\text{HU})_2 \cdot 6\text{H}_2\text{O}$

When calcium hydroxide solution was added to crystalline uric acid the latter dissolved but simultaneously $\text{Ca}(\text{HU})_2 \cdot 6\text{H}_2\text{O}$ crystals started forming. After completion of the reaction the solid phase consisted of layered aggregates of large, elongated crystals as shown in Fig. 1. The XRD powder pattern of moist precipitates suggested the presence of some amorphous material in addition to the crystalline matter. During prolonged air-drying, however, further recrystallization occurred resulting in $\text{Ca}(\text{HU})_2 \cdot 6\text{H}_2\text{O}$ crystals with a well resolved XRD powder pattern. The d -values and relative intensities obtained were in very good agreement with those already reported [19]. Infrared spectra confirmed the presence of HU^- and water

molecules but comparison of the position of $\nu(\text{CO})$ in the spectrum of $\text{Ca}(\text{HU})_2 \cdot 6\text{H}_2\text{O}$ with the position of the same absorption in the spectra of $\text{Ca}(\text{HU})_2\text{L}_3$ ($\text{L} = \text{dimethylsulphoxide}$ or $\text{N,N-dimethylformamide}$) indicated that calcium atoms in the former compound could be coordinated by water molecules rather than by hydrogenurate ions; the presence of aquo cation $[\text{Ca}(\text{H}_2\text{O})_6]^{2+}$ in the structure of $\text{Ca}(\text{HU})_2 \cdot 6\text{H}_2\text{O}$ is anticipated [27]. Chemical and thermogravimetric analyses (TGA) revealed the presence of two purine rings and six water molecules per calcium atom (Table 2). TGA showed the loss of 22.2 ± 0.5 mass % in the temperature range from 387 to 640 K corresponding to six water molecules and an additional 56.6 ± 1.1 mass % loss up to 870 K, due to the decomposition of purine.

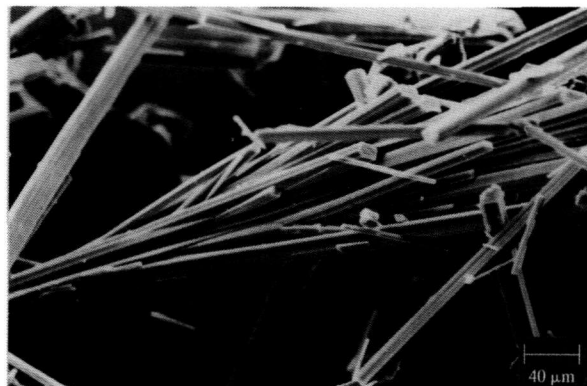


Fig. 1. Scanning electron micrograph of calcium hydrogenurate hexahydrate crystals.

The precipitation diagram of $\text{H}_2\text{U}-\text{Ca}(\text{OH})_2-\text{HCl}-\text{H}_2\text{O}$ systems aged for 2 months at 310 K shows the composition of the prevailing solid phases in a wide range of equilibrium pH and total uric acid concentration (Fig. 2). In all samples the molar ratio $c(\text{Ca})/c(\text{H}_2\text{U})$ was 1.5. $\text{Ca}(\text{HU})_2 \cdot 6\text{H}_2\text{O}$ crystallized as a single solid phase at $c(\text{H}_2\text{U}) > 1.1 \text{ mol dm}^{-3}$ and $7 < \text{pH} < 10$. At $\text{pH} < 7$ some uric acid was always admixed while at $\text{pH} > 10$ the coprecipitation of a small amount of CaCO_3 could not be avoided even when the samples were prepared in a dry-box under a nitrogen atmosphere. From the precipitation boundary which is positioned at $c(\text{H}_2\text{U}) \sim 8 \cdot 10^{-4} \text{ mol dm}^{-3}$, an approximate value of the solubility product of $\text{Ca}(\text{HU})_2 \cdot 6\text{H}_2\text{O}$ was calculated [Eq. (1)] to be of the order of magnitude of 10^{-10} .

Table 2. Preparative conditions and thermogravimetric and chemical analysis of $\text{Ca}(\text{HU})_2 \cdot 6\text{H}_2\text{O}$ (s)

$c(\text{H}_2\text{U})_{\text{init}}$ (mmol dm^{-3})	$c(\text{Ca})_{\text{init}}$ (mmol dm^{-3})	pH_{init}	TG analysis (%)		Chemical analysis (%)			
			H_2O	purine	Ca	C	H	N
10.0	15.0	7.30	22.07	55.28	8.20	24.92	3.65	23.86
4.0	4.4	7.40	21.23	56.70		24.77	4.00	25.01
10.0	15.0	7.50	22.43	57.94	8.16	24.96	3.56	24.66
calculated values:			22.41	56.88	8.30	24.80	3.76	23.23

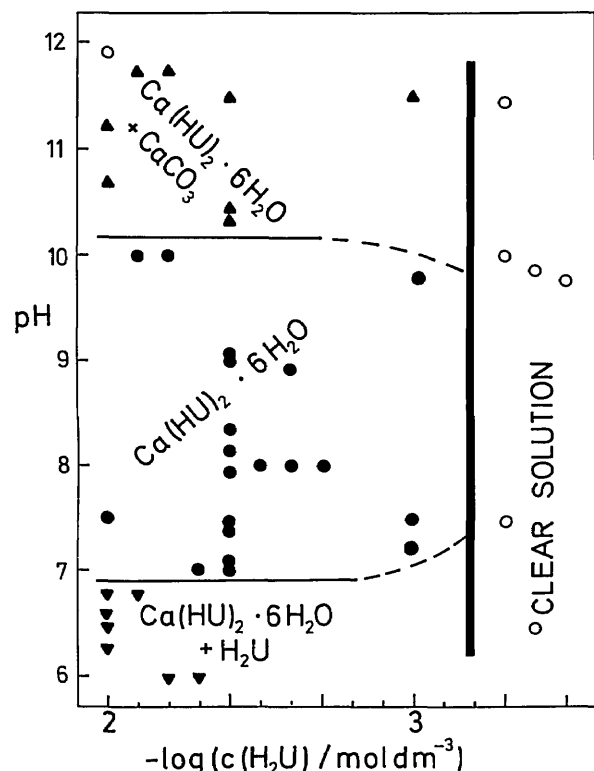


Fig. 2. Precipitation diagram for the system: uric acid–calcium hydroxide–hydrochloric acid–water observed 2 months after sample preparation at 310 K. The data points indicate initial uric acid concentration, $c(\text{H}_2\text{U})$, and pH determined in equilibrated solutions. In all systems initial $c(\text{Ca}) = 1.5 \cdot c(\text{H}_2\text{U})$. The precipitation boundary (thick line) separates clear solutions (o) from the region of precipitates. Phase boundaries (thin lines) separate the region of pure calcium hydrogenurate hexahydrate, $\text{Ca}(\text{HU})_2 \cdot 6\text{H}_2\text{O}$ (●) from the regions of its mixture with CaCO_3 (▲) and uric acid (▼).

3.2 Solubility Products of $\text{Ca}(\text{HU})_2 \cdot 6\text{H}_2\text{O}$

The equilibration time for solubility determinations of $\text{Ca}(\text{HU})_2 \cdot 6\text{H}_2\text{O}$ depended on temperature and pH. For systems at 310 K, $\text{pH} > 7$ and for all systems at 288 and 298 K the equilibration time was 24 h. The systems at 310 K, $\text{pH} < 7.5$ and all systems at 318 K were equilibrated for 3 h to avoid precipitation of uric acid. Preliminary kinetic experiments

monitoring the rate of dissolution of $\text{Ca}(\text{HU})_2 \cdot 6\text{H}_2\text{O}$ into water showed that equilibrium is soon established, i.e., at 288 and 298 K consistent results were obtained between 3 and 24 h while at 310 and 318 K between 20 min and 3 h.

In Table 3 are given the concentrations of soluble urate and calcium, pH, and calculated ionic strengths (a) in reequilibrated systems after 24 h (systems 1 to 6) and (b) in the systems after 3 h equilibration of $\text{Ca}(\text{HU})_2 \cdot 6\text{H}_2\text{O}$ in water (systems 7 to 13), uric acid (systems 14 to 18) and calcium chloride solutions (systems 19 to 22) at the physiological temperature of 310 K. No significant difference between the concentration of total soluble calcium and ionic calcium was detected. The values were in the range of experimental error ($\pm 2.8\%$) indicating that Ca^{2+} is the dominant calcium species in urate solutions and that calcium does not form strong soluble complexes with urate anions. The mean value of total soluble and ionic calcium concentration is taken as equilibrium concentrations, $c(\text{Ca})_{\text{eq}}$. Calculated thermodynamic solubility products, $K_s(I=0)$, listed in Table 3 have an average value of $(5.3 \pm 0.4) \cdot 10^{-10}$. The experimental data obtained at 310 K in reequilibrated (Fig. 3, open circles) and equilibrated systems (Fig. 3, filled circles) are plotted in the form of a chemical potential plot [Eq. (4)] giving a straight line with the slope of 0.505 indicating that in the range of $6.6 < \text{pH} < 10.1$ the solid phase in equilibria with supernatant was $\text{Ca}(\text{HU})_2 \cdot 6\text{H}_2\text{O}$.

In Table 4 are listed the concentrations of all components in solutions equilibrated with $\text{Ca}(\text{HU})_2 \cdot 6\text{H}_2\text{O}$ at 288 K (systems 23 to 27), 298 K (systems 28 to 47) and 318 K (systems 48 to 54). $\text{Ca}(\text{HU})_2 \cdot 6\text{H}_2\text{O}$ was equilibrated in water (systems 23 to 25, 28 to 33, and 48 to 50), uric acid solutions (systems 26 and 27, 34 to 39, and 51 to 54) or calcium chloride solutions (systems 40 to 48). The $K_s(I=0)$ values obtained show differences in the range of experimental error giving an average value of $(7.6 \pm 1.1) \cdot 10^{-11}$ at 288 K, $(1.6 \pm 0.3) \cdot 10^{-10}$ at 298 K, and $(9.8 \pm 0.6) \cdot 10^{-10}$ at 318 K. Chemical

Table 3. Experimental solubility data and calculated K_s values for $\text{Ca}(\text{HU})_2 \cdot 6\text{H}_2\text{O}$ (s) at 310 K

System No. ^a	$c(\text{U})_{\text{eq}}$ (mmol dm ⁻³)	$c(\text{Ca})_{\text{eq}}$ (mmol dm ⁻³)	pH _{eq}	I_{eq} (mmol dm ⁻³)	$K_s \cdot 10^{10}$ ($I=0$)
1	0.741	3.010	10.06	8.60	4.15
2	0.609	2.800	7.95	8.00	5.75
3	0.605	2.970	8.17	8.40	5.93
4	0.563	2.900	7.40	8.40	4.98
5	0.577	2.860	7.76	8.30	5.23
6	0.551	2.890	7.76	8.30	4.81
7	1.110	0.566	7.15	1.68	5.07
8	1.160	0.594	7.14	1.76	5.77
9	1.140	0.609	7.09	1.78	5.68
10	1.160	0.609	6.83	1.78	5.68
11	1.120	0.563	7.16	1.70	5.22
12	1.110	0.583	7.15	1.72	5.20
13	1.120	0.567	7.27	1.69	5.21
14	1.150	0.569	6.65	1.68	5.06
15	1.160	0.592	6.79	1.75	5.49
16	1.190	0.594	6.93	1.77	5.92
17	1.170	0.586	6.87	1.74	5.61
18	1.130	0.548	7.06	1.65	5.05
19	0.246	50.000	6.83	150.10	5.22
20	0.378	10.200	6.92	30.60	5.01
21	0.484	5.280	6.91	15.80	5.37
22	0.773	1.380	6.96	4.14	5.08

^a Systems 1 to 6 were reequilibrated in original supernatants for 24 h. In systems 7 to 13, $\text{Ca}(\text{HU})_2 \cdot 6\text{H}_2\text{O}$ was equilibrated in water. In systems 14 to 18 the initial uric acid concentrations were 0.1, 0.1, 0.08, 0.05, and 0.03 mmol dm⁻³, respectively. In systems 19 to 22 the initial calcium chloride concentrations were 50, 10, 5, and 1 mmol dm⁻³, respectively. Equilibration time for systems 7 to 22 was 3 h.

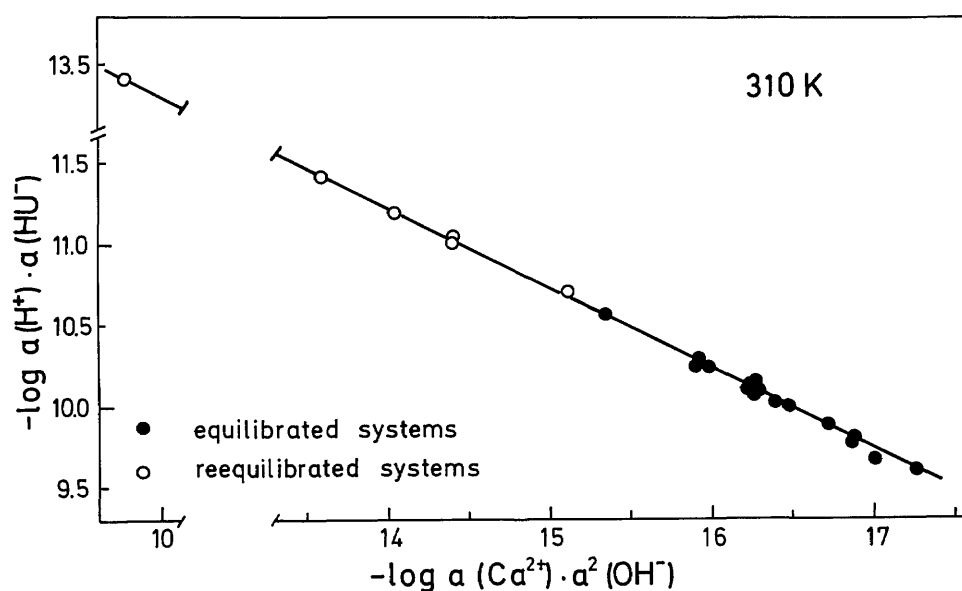


Fig. 3. Potential diagram calculated by using the solubility data for $\text{Ca}(\text{HU})_2 \cdot 6\text{H}_2\text{O}$ at 310 K (Table 3) and dissociation constants of H_2U and H_2O (Table 1). The slope of the straight line is 0.505.

Table 4. Experimental solubility data and calculated K_s values for $\text{Ca}(\text{HU})_2 \cdot 6\text{H}_2\text{O}$ (s) at different temperatures (288, 298, and 318 K)

System No. ^a	T/K	$c(\text{U})_{\text{eq}}$ (mmol dm^{-3})	$c(\text{Ca})_{\text{eq}}$ (mmol dm^{-3})	pH_{eq}	I_{eq} (mmol dm^{-3})	$K_s \cdot 10^{10}$ ($I=0$)
23	288	0.631	0.323	6.53	0.97	0.87
24		0.631	0.328	6.61	0.95	0.86
25		0.579	0.285	6.61	0.84	0.64
26		0.736	0.336	5.93	0.92	0.65
27		0.675	0.312	6.26	0.90	0.76
28	298	0.776	0.393	6.74	0.12	1.62
29		0.736	0.387	6.88	1.13	1.49
30		0.677	0.386	6.96	1.11	1.28
31		0.781	0.391	6.95	1.17	1.71
32		0.727	0.347	6.95	1.05	1.33
33		0.721	0.384	6.68	1.11	1.35
34		0.819	0.397	6.20	1.13	1.36
35		0.935	0.414	6.38	1.23	2.10
36		0.820	0.377	6.69	1.14	1.72
37		0.886	0.391	7.04	1.22	2.22
38		0.777	0.346	7.04	1.08	1.53
39		0.731	0.396	6.60	1.13	1.39
40		0.119	50.000	6.43	150.10	1.08
41		0.115	50.000	6.97	150.10	1.15
42		0.228	10.000	6.72	30.11	1.70
43		0.226	10.000	6.87	30.11	1.72
44		0.239	5.120	6.56	15.35	1.14
45		0.490	1.000	6.98	3.25	1.56
46		0.499	1.230	6.98	3.71	1.87
47	0.496	1.270	6.76	3.78	1.82	
48	318	1.460	0.678	7.29	1.99	9.62
49		1.360	0.719	7.29	2.12	9.47
50		1.420	0.703	7.34	2.10	10.20
51		1.440	0.700	6.90	2.11	10.04
52		1.430	0.624	7.16	1.99	9.12
53		1.360	0.715	7.18	2.11	9.37
54		1.480	0.705	7.15	2.15	10.89

^a In systems 23 to 25, 28 to 33, and 48 to 50, $\text{Ca}(\text{HU})_2 \cdot 6\text{H}_2\text{O}$ was equilibrated in water. In systems 26, 34 to 38, 51 and 54 initial uric acid concentration was 0.1 mmol dm^{-3} and in systems 27, 39, 52, and 53 it was $0.05 \text{ mmol dm}^{-3}$. In systems 40 to 47 initial calcium chloride concentrations were 50, 50, 10, 10, 5, 1, 1, and 1 mmol dm^{-3} , respectively. Equilibration time for systems 23 to 47 was 24 h and for systems 48 to 54, 3 h.

potential plots, showing linear dependence of $-\log a(\text{H}^+) \cdot a(\text{HU}^-)$ vs $-\log a(\text{Ca}^{2+}) \cdot a^2(\text{OH}^-)$ with slopes of 0.483, 0.510, and 0.492 for 288, 298, and 318 K, respectively (Fig. 4), confirmed that the solid phase has a molar Ca/urate ratio of 1:2. The data from equilibrated systems at 310 K (Fig. 3, filled circles) are shown in Fig. 4 for comparison. Solubility of $\text{Ca}(\text{HU})_2 \cdot 6\text{H}_2\text{O}$ increases with increasing temperature.

The solubility products can be determined from the intercepts of the straight lines in the chemical potential plots [Eq. (4), Fig. 4] but with less precision than by direct computation from equilibrium concentrations. Specifically, in the pH range from 6.5 to 8.5 the dominant urate species is HU^- and the calculated values of $a(\text{HU}^-)$ are relatively insensitive to small uncertainties in pH. On the other hand in the potential diagram (Fig. 4), the small changes in pH alter slopes of the straight lines and cause significant differences in intercepts and corresponding K_s values.

3.3 Possible Formation of $\text{Ca}(\text{HU})_2 \cdot 6\text{H}_2\text{O}$ in Urines

From the precipitation diagram shown in Fig. 2 it is possible to conclude that in the physiological range of urinary pH ($5.0 < \text{pH} < 6.5$) coprecipitation of uric acid and $\text{Ca}(\text{HU})_2 \cdot 6\text{H}_2\text{O}$ might be expected while in slightly alkaline urines $\text{Ca}(\text{HU})_2 \cdot 6\text{H}_2\text{O}$ could precipitate as a single solid phase. In the physiological range of total urinary urate and calcium concentrations, $1 < c(\text{U})_{\text{tot}} < 3 \text{ mmol dm}^{-3}$ and $1 < c(\text{Ca})_{\text{tot}} < 4 \text{ mmol dm}^{-3}$ ($c(\text{Ca}^{2+}) \approx 0.5 \cdot c(\text{Ca})_{\text{tot}}$, $I = 0.3 \text{ mol dm}^{-3}$, 310 K) the ion activity product, $IAP = a(\text{Ca}^{2+}) \cdot a^2(\text{HU}^-)$, varies from $7 \cdot 10^{-12}$ to $2 \cdot 10^{-9}$. Supersaturation with respect to precipitation of $\text{Ca}(\text{HU})_2 \cdot 6\text{H}_2\text{O}$ ($S = IAP/K_s$) varies from 0.01 to 3.8. It is obvious that these urines are undersaturated or slightly supersaturated with respect to precipitation of $\text{Ca}(\text{HU})_2 \cdot 6\text{H}_2\text{O}$ and spontaneous precipitation of this salt would not be expected. At higher supersaturations,

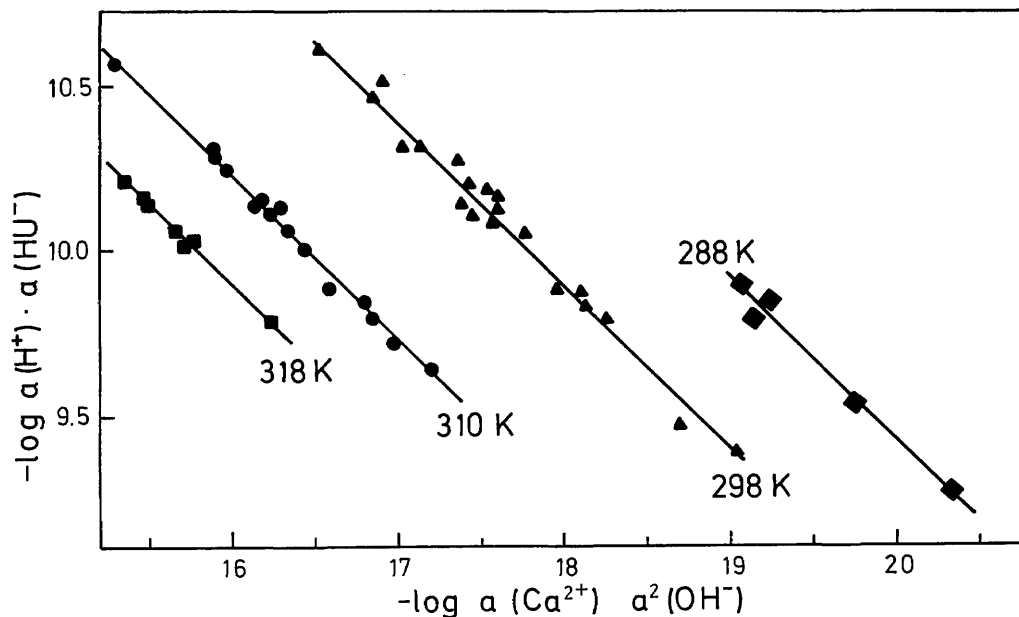


Fig. 4. Potential diagram calculated by using the solubility data for $\text{Ca}(\text{HU})_2 \cdot 6\text{H}_2\text{O}$ (Table 4) and dissociation constants of H_2U and H_2O (Table 1). The slopes of the straight lines are 0.483 (288 K), 0.510 (298 K), and 0.492 (318 K). The results determined in equilibrated systems at 310 K are given for comparison (slope of 0.505).

eventually, coprecipitation or overgrowth of $\text{Ca}(\text{HU})_2 \cdot 6\text{H}_2\text{O}$ on previously formed uric acid crystals may be possible. The conditions for precipitation of $\text{Ca}(\text{HU})_2 \cdot 6\text{H}_2\text{O}$ exist in urines of patients with both hyperuricosuria and hypercalciuria.

4. Conclusions

The thermodynamic solubility products, K_s , of $\text{Ca}(\text{HU})_2 \cdot 6\text{H}_2\text{O}$ have the values of $(7.6 \pm 1.1) \cdot 10^{-11}$ at 288 K, $(1.6 \pm 0.3) \cdot 10^{-10}$ at 298 K, $(5.3 \pm 0.4) \cdot 10^{-10}$ at 310 K, and $(9.8 \pm 0.6) \cdot 10^{-10}$ at 318 K. In the physiological range of urinary concentrations of urate and calcium, and pH, spontaneous precipitation of $\text{Ca}(\text{HU})_2 \cdot 6\text{H}_2\text{O}$ would not be expected, while in urines of patients with high concentrations of constituent ions (pathological conditions) the formation of $\text{Ca}(\text{HU})_2 \cdot 6\text{H}_2\text{O}$ is possible.

Acknowledgments

The financial support by the Ministry of Science, Technology and Informatics of Croatia, by the National Institute of Standards and Technology,

Gaithersburg, MD under Grant No. PN 776 and by the Commission of the European Communities Directorate General XII under the Programme of International Cooperation is gratefully acknowledged.

5. References

- [1] K. Lonsdale, *Science* **159**, 1199 (1968).
- [2] K. Lonsdale and P. Mason, *Science* **152**, 1511 (1966).
- [3] J. L. Meyer, J. H. Bergert, and L. H. Smith, *Invest. Urol.* **14**, 115 (1976).
- [4] P. G. Koutsoukos, C. Y. Lam-Erwin, and G. H. Nancollas, *Invest. Urol.* **18**, 178 (1980).
- [5] F. L. Coe, R. L. Lawton, R. B. Goldstein, and V. Tembe, *Proc. Soc. Expl. Biol. Med.* **149**, 926 (1975).
- [6] C. Y. C. Pak and L. H. Arnold, *Proc. Soc. Expl. Biol. Med.* **149**, 930 (1975).
- [7] L. C. Herring, *J. Urol.* **88**, 545 (1962).
- [8] M. Berenyi, G. Liptay, A. Babics, and L. Erdey, *Zeitschr. Urol.* **6**, 361 (1967).
- [9] W. Dosch, *Fortschr. Urol. Nephrol.* **17**, 240 (1981).
- [10] J. E. Seegmiller, *Arthritis Rheumat.* **8**, 714 (1965).
- [11] O. Sperling, O. Kedem, and A. de Vries, *Rev. Franc. Etudes Clin. Biol.* **11**, 40 (1966).
- [12] W. R. Wilcox, A. Khalaf, A. Weinberger, J. Kippen, and J. R. Klinenberg, *Med. Biol. Eng.* **10**, 522 (1972).

- [13] C. Y. Lam, G. H. Nancollas, and S. J. Ko, *Invest. Urol.* **15**, 473 (1978).
- [14] E. Mentasti, C. Rinaudo, and R. Boistelle, *J. Chem. Eng. Data* **28**, 247 (1983).
- [15] V. Babić-Ivančić, H. Füredi-Milhofer, W. E. Brown, and T. M. Gregory, *J. Crystal Growth* **83**, 581 (1987).
- [16] D. J. Allen, G. Milosovich, and A.M. Mattocks, *Arthritis Rheumat.* **8**, 1123 (1965).
- [17] W. Dosch and A. Matzke, *Zur Kristallchemie der Urate*, in *Pathogenese und Klinik der Harnsteine X*, W. Vahlensieck and G. Gasser, eds., Steinkopf, Darmstadt (1984) pp. 279-289.
- [18] H. Füredi-Milhofer, V. Babić-Ivančić, O. Milat, W. E. Brown, and T. M. Gregory, *J. Crystal Growth* **83**, 572 (1987).
- [19] P. Carmona, *Solid State Chem.* **55**, 293 (1984).
- [20] Z. Kopajtić, Ph.D. Thesis, University of Zürich, Switzerland, 1985.
- [21] C. Y. Lam-Erwin and G. H. Nancollas, *J. Crystal Growth* **53**, 215 (1981).
- [22] H. S. Harned and R. A. Robinson, *Trans. Faraday Soc.* **36**, 973 (1940).
- [23] H. S. Harned and B. B. Owen, *The Physical Chemistry of Electrolytic Solutions*, 3rd ed., Reinhold Publ. Corp., New York (1958).
- [24] R. H. Stokes and R. A. Robinson, *Electrolyte Solutions*, Butterworth and Co., London (1959).
- [25] W. E. Brown, *Solubilities of Phosphates and Other Sparingly Soluble Compounds*, in *Environment Phosphorus Handbook*, E. M. Griffith, A. Beeton, J. H. Spencer, and D. T. Michell, eds., Wiley & Sons, New York (1973) pp. 203-239.
- [26] W. E. Brown, T. M. Gregory, and H. Füredi-Milhofer, *J. Crystal Growth* **83**, 588 (1987).
- [27] N. Brničević, V. Babić-Ivančić, and H. Füredi-Milhofer, *J. Inorg. Biochem.* **43**, 771 (1991).

About the authors: V. Babić-Ivančić, H. Füredi-Milhofer, N. Brničević, and M. Marković are scientists at Rudjer Bošković Institute, Zagreb, Croatia, working on physicochemical aspects of pathological mineralization. M. Marković is also a guest scientist at the American Dental Association Health Foundation, Paffenbarger Research Center, NIST. The National Institute of Standards and Technology is an agency of the Technology Administration, U.S. Department of Commerce.

The NIST SPIDER, A Robot Crane

Volume 97

Number 3

May-June 1992

**James Albus,
Roger Bostelman, and
Nicholas Dagalakis**

National Institute of Standards
and Technology,
Gaithersburg, MD 20899

The Robot Systems Division of the National Institute of Standards and Technology has been experimenting for several years with new concepts for robot cranes. These concepts utilize the basic idea of the Stewart Platform parallel link manipulator. The unique feature of the NIST approach is to use cables as the parallel links and to use winches as the actuators. So long as the cables are all in tension, the load is kinematically constrained, and the cables resist perturbing forces and moments with equal stiffness to both positive and negative loads. The result is that the suspended load is constrained with a mechanical stiffness determined by the elasticity of the cables, the suspended weight, and the geometry of the mechanism. Based on these concepts, a revolutionary new type of robot crane, the NIST SPIDER (Stew-

art Platform Instrumented Drive Environmental Robot) has been developed that can control the position, velocity, and force of tools and heavy machinery in all six degrees of freedom (x, y, z , roll, pitch, and yaw). Depending on what is suspended from its work platform, the SPIDER can perform a variety of tasks. Examples are: cutting, excavating and grading, shaping and finishing, lifting and positioning. A 6 m version of the SPIDER has been built and critical performance characteristics analyzed.

Key words: cables; kinematically constrained; parallel link manipulator; robot cranes; six degrees of freedom; six meter model; Stewart platform; work platform.

Accepted: May 7, 1992

Contents

1. Introduction	373
2. Objective	374
3. Structure and Control	374
4. Comparison to Conventional Cranes	379
5. Applications	379
6. Limits of Workspace Study	380
6.1 Mathematical Model	380
6.2 Condition #1	382
6.3 Condition #2	382
7. Experiments Performed	383
8. Summary and Conclusions	383
9. References	384

1. Introduction

A new crane design utilizing six cables to suspend a load platform was first developed by the National Institute of Standards and Technology in the early 1980s. A Defense Advanced Research Projects Agency (DARPA) sponsored program on robot crane technology produced the design, development and testing of three different sized prototypes to determine the performance characteristics of this proposed robot crane design. A description of the overall DARPA program and the results of this research are presented in [1]. Initial testing of these prototypes showed that this design results in a stiff load platform [2,3]. This platform

(see Fig. 1) can be used in typical crane operations, or as a robot base, or a combination of both. Applications of this new crane design in the construction industry are illustrated in Fig. 2.

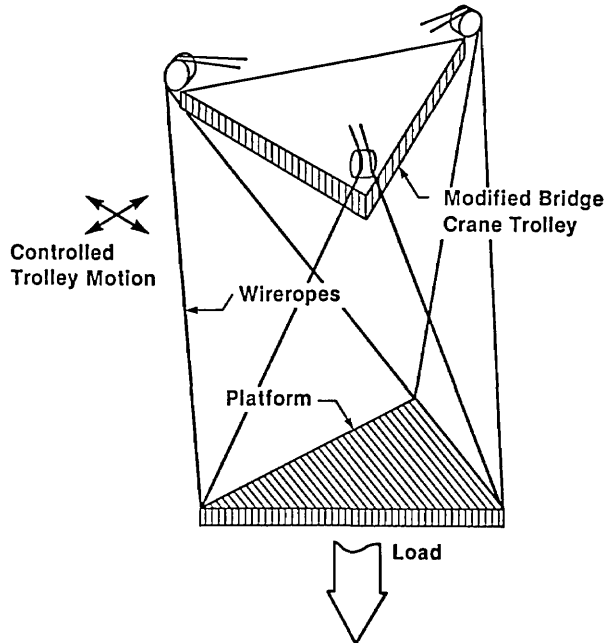


Fig. 1. Design concept for improving stiffness of crane suspension mechanisms.

In response to the oil fires set in Kuwait during the Persian Gulf War, NIST adapted its robot crane technology for assisting in extinguishing oil well fires. A system called the NIST Oil Well Fire Fighting Robot (NOWFFR) was designed and constructed. This robot is described in a video tape and a NIST internal working document. A photograph of the NOWFFR is shown in Fig. 3.

Early in 1991, the NOWFFR design was modified for applications related to nuclear and toxic waste site cleanup. The new robot design is called the SPIDER (Stewart Platform Instrumented Drive Environmental Robot). The SPIDER is light weight and easily assembled. The SPIDER can be made mobile by attaching vehicles to the feet so that it can be driven over rough terrain. A conceptual diagram of the SPIDER is shown in Fig. 4.

Two models of the SPIDER have been designed and constructed. A 2 m model has been used to test mobility issues. A 6 m model has been used to test lifting and load positioning parameters and to analyze the size and shape of the work volume.

2. Objective

The objective of this paper is to report on the design, development and evaluation of the SPIDER. The primary function of the SPIDER is to lift, maneuver, and position large loads with precise control of position and force in all six degrees of freedom.

The SPIDER consists of a stable platform supported by six cables suspended from three points on a fixed or mobile octahedral structure. The six cables are arranged to kinematically constrain the stable platform such that its stiffness is determined by the tensile elasticity of the cables. Maximum stiffness is maintained so long as perturbing forces and/or torques are below a threshold determined by the weight of the load. For forces or torques above that threshold, one or more cables will go slack, and stiffness will drop to that generated by pendulum forces of the load on the cables remaining taut.

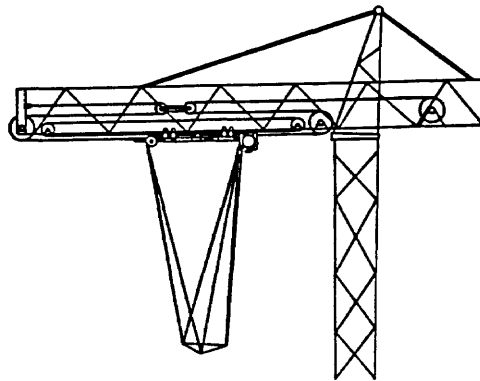
When all six cables are in tension, the stable platform is kinematically constrained, and there exists a known mathematical relationship between the lengths of the six cables and the position and orientation of the platform. The theory of this mathematical relationship has been known for many years. The theory was first embodied in a Stewart platform for testing tires in the 1950s [4], and applied to aircraft flight simulators during the 1960s and 1970s. It was applied to cable driven manipulators by Landsberger [5,6] and to cranes by NIST in the 1980s [1].

On the SPIDER, the lengths of the six cables are controlled by six winches. These are controlled and coordinated by a computer. Input commands from a six-axis joystick enable an operator to control the motion of the stable platform in all six degrees of freedom (x , y , z , roll, pitch, and yaw). The operator can thus maneuver the stable platform, and whatever load or tool that is attached to it, over a large working volume.

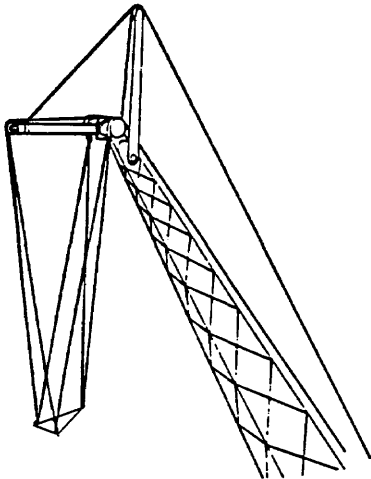
The three support points of the octahedron are carried by three vehicles for mobility. Coordination of vehicle track motions to accomplish steering and velocity commands provided by an operator is also done by computer.

3. Structure and Control

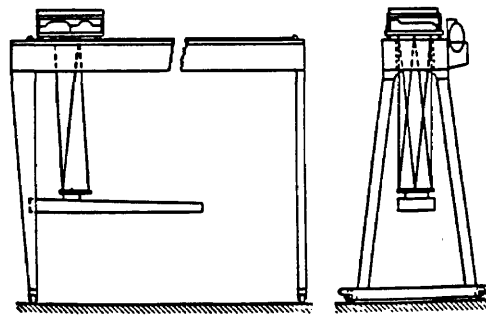
The framework of the SPIDER is a six legged structure resting on three support points. The legs are 6 m aluminum tubes that are 10 cm in diameter



a) Tower Crane



b) Boom Crane



c) Gantry Bridge Crane (with extended reach)

Fig. 2. Stabilized platform concept applied to various crane designs.

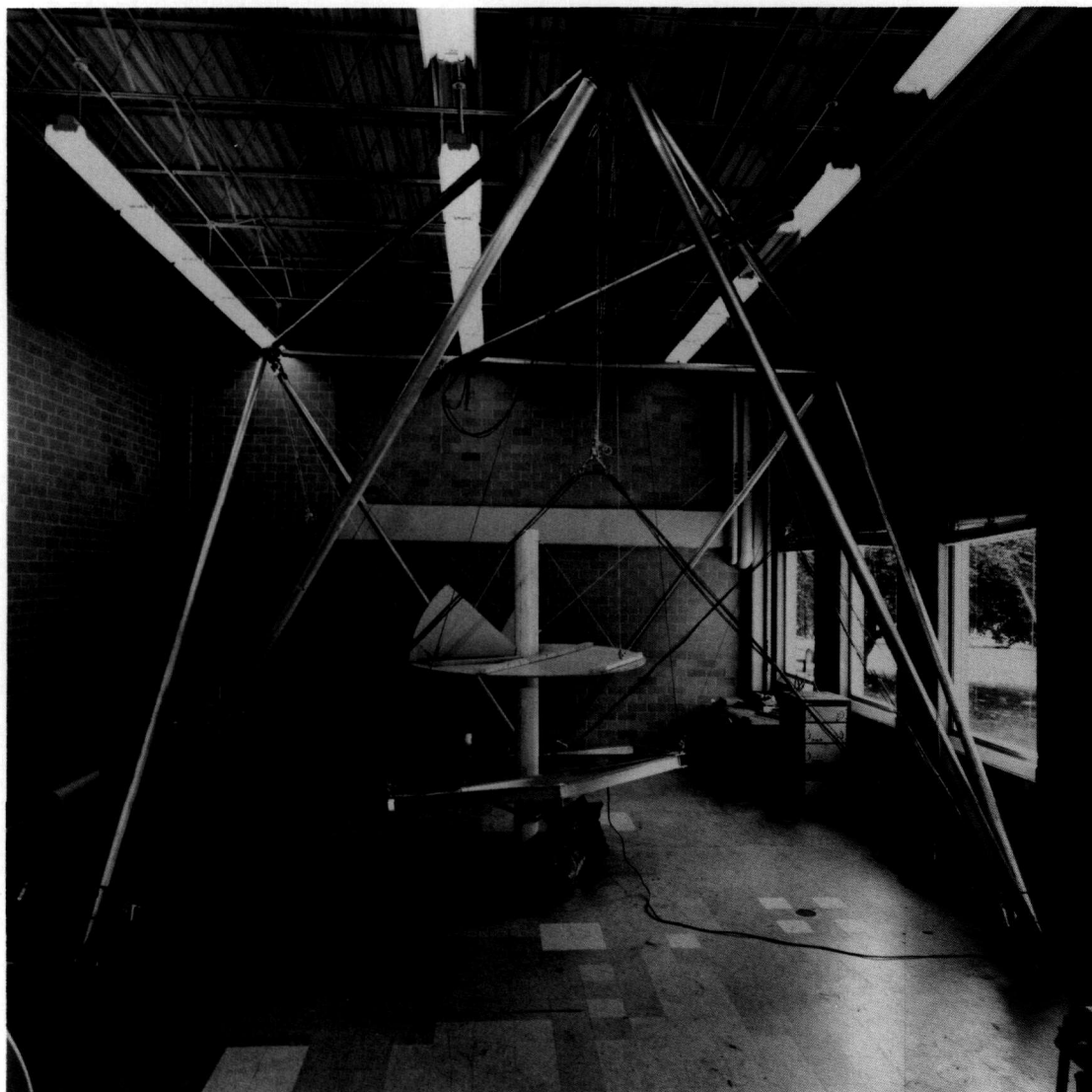


Fig. 3. Photograph of the NOWFFR before it was modified to become the SPIDER. Centered is a heat shield/chimney and a chain saw attached to the platform and ready to cut an oak log.

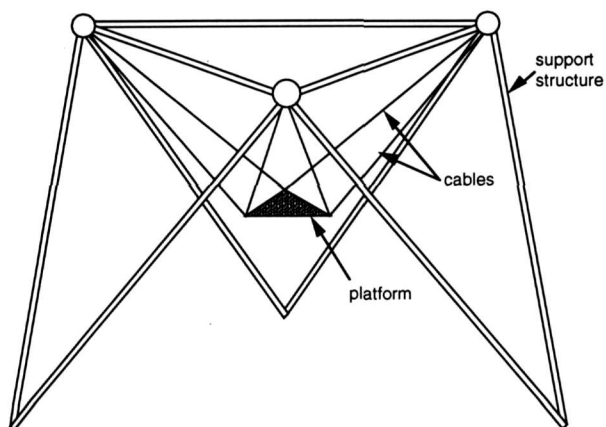


Fig. 4. The SPIDER geometry.

and constructed in an octahedron geometry. These can be seen in Fig. 3, which is a photograph of the NOWFFR taken before it was modified to become the SPIDER. The top of the SPIDER structure consists of a triangle. Each vertex of the triangle supports two cables. Together, the six cables support a lower work platform. The connecting joints at the vertices consist of ball and socket joints. Due to its octahedron geometry, all forces are directed through points at the vertices. As a result there are no bending or twisting moments generated by the load. Each member of the structure is always in pure compression or tension except for supporting its own weight. The SPIDER structure thus provides near maximum strength and stiffness possible

for any given mass of structural material.

The lower work platform is supported by six braided steel cables 5 mm in diameter. The length of each cable is controlled by a winch having a 455 kg load rating. Figure 5 shows the winches. The cables run from the winches up and over pulleys at the vertices of the upper triangle, and back down to the

lower work platform. By controlling the six winches, an operator can maneuver the lower work platform in six degrees of freedom. The work platform is made of aluminum I-beams. It can be a variety of sizes. Studies at NIST have shown that a 2 to 1 ratio of the size of the upper triangle to the lower platform is the most stiff for lateral force loading [2].

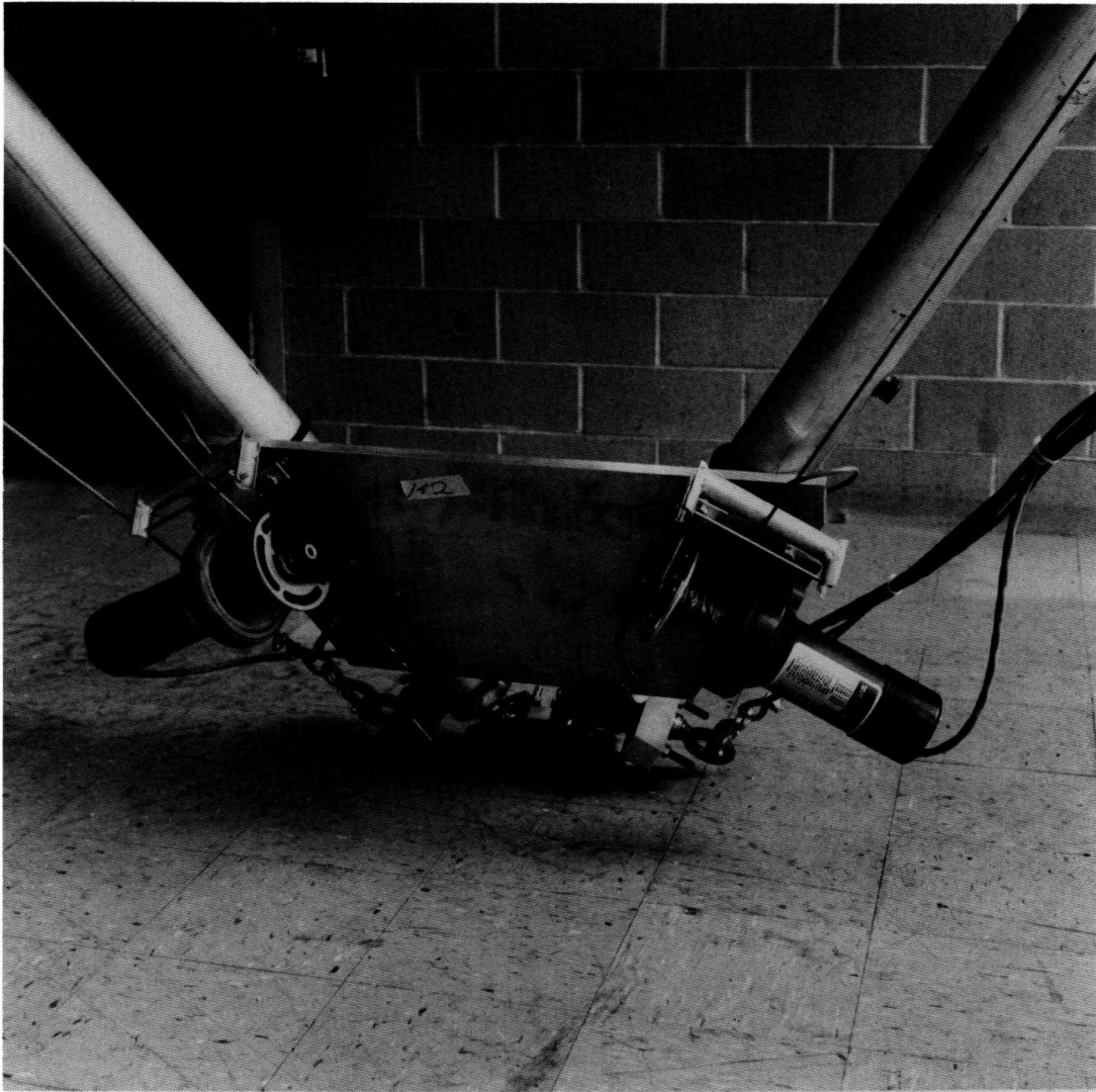


Fig. 5. One of three pairs of winches used to maneuver the platform.

The joystick used to control the SPIDER is a Stewart Platform with linear potentiometers as shown in Fig. 6. By orienting this joystick so that the potentiometers are roughly parallel to the SPIDER cables, the control mode can be master-slave rate control. In this mode, the velocity of each winch is controlled by the displacement of its corresponding potentiometer. Over a limited range wherein the cables and potentiometers remain roughly parallel, the SPIDER motion can be controlled directly by the potentiometers without a computer. A diagram of this control mode is shown in Fig. 7. The joystick potentiometers generate analog voltages for amplifiers that control the winches. This is called the Manual mode.

The SPIDER also has a Computed-Manual mode. In this mode the joystick signals are switched to send analog voltages from the joystick to a computer. Joystick potentiometers signals are fed into an analog-to-digital (A/D) board embedded in the computer. From these signals the computer calculates the joystick input position and orientation and translates it to SPIDER command cable lengths. Feedback is received from cable length and force sensors located near the winches. This enables closed loop position, velocity, and force control. Cable travel encoders generate phase quadrature signals for an encoder input board embedded in the computer. Cable tension sensors are input into an A/D board in the computer. Command signals are

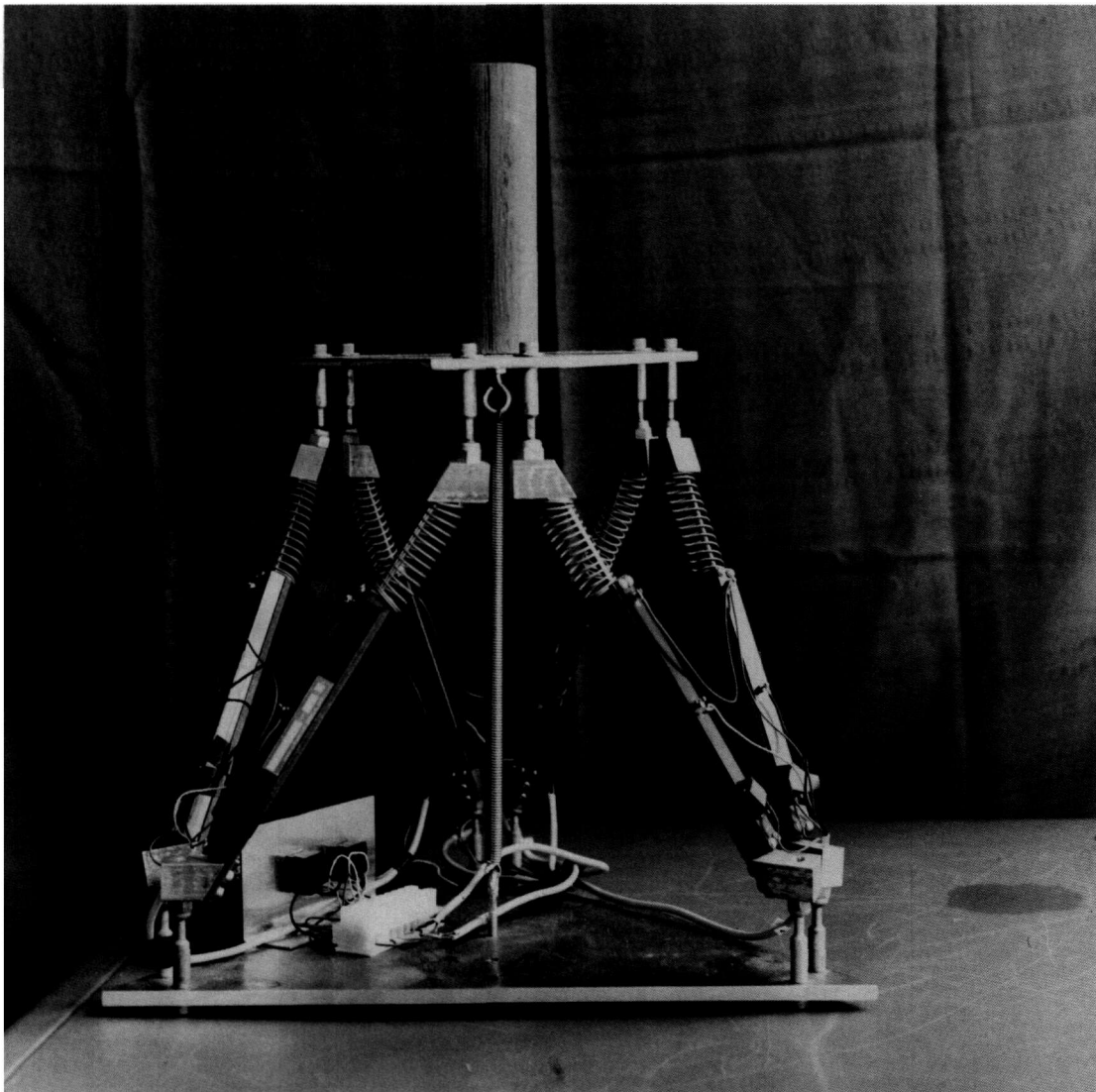


Fig. 6. Stewart platform joystick used as operator interface to drive the lower platform.

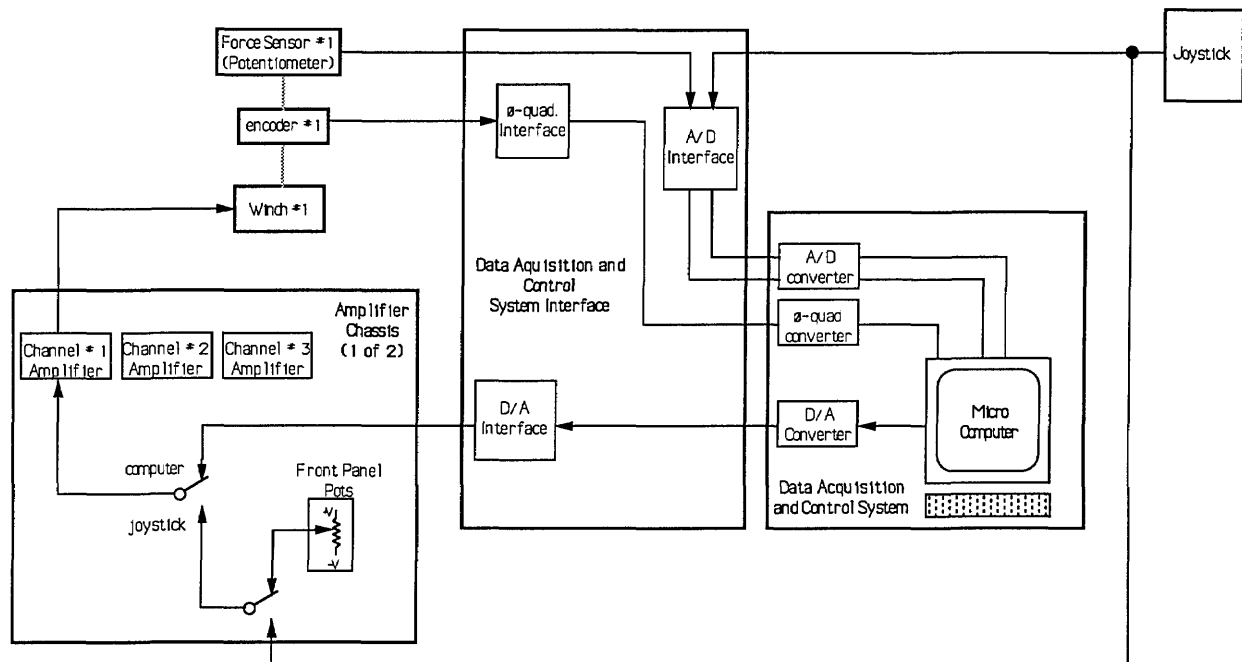


Fig. 7. Control system architecture for the SPIDER showing one of six channels.

output from the computer via a digital to analog (D/A) board and sent to the winch amplifiers.

Control algorithms being developed for the SPIDER include forward and reverse kinematics that are necessary to allow trajectory control of the lower platform. With trajectory control, the work platform could be made to follow a particular path while the computer interprets joystick information to control the speed of the platform.

4. Comparison to Conventional Cranes

Existing cranes of many different types from many manufacturers, are able to lift comparable loads, but cannot stabilize the loads in rotation or sway. Under ideal conditions, a highly skilled crane operator can provide some measure of oscillation damping. However, for precise orientation, a crew of riggers is needed to manually stabilize the load from rotating and swinging and to manually guide the load into its final desired position.

Existing cranes, even with expert operators, cannot prevent perturbations such as wind from causing the load to sway, in some cases by more than a meter. Novice operators of conventional cranes may have difficulty in preventing heavy loads from colliding with objects in the environment. Existing cranes provide little or no load stabilization against rotations, and have no means of controlling forces or torques on the load.

The principal advantage of the SPIDER is that it provides sufficient control to allow even a novice operator to position a load without sway to within a few millimeters in x , y , and z , and to control orientation without oscillation to within 1° in roll, pitch, and yaw. Force sensors on the SPIDER winch mechanisms could also allow the operator (with computer assistance) to control forces and torques on a load after it comes into contact with the environment. The control provided by the SPIDER could thus reduce the size of the crew needed to manually position loads from three or four, to zero or one.

An additional advantage of the SPIDER is its high lift-to-weight ratio. Due to its octahedron geometry, the SPIDER requires no counter weight and experiences no twisting or bending moments. As a result, it can lift at least five times its own weight. This is significantly more than any robot or crane in current use.

5. Applications

The principal applications of the SPIDER are expected to be lifting and positioning objects or power tools weighing up to a ton. Depending on what is suspended from its work platform, the SPIDER could perform a variety of tasks that are not possible by conventional cranes. For example,

For cutting:

The SPIDER could manipulate a variety of saws (chain saw, wire saw, or disc saw), rotary cutting tools (router, milling tool, grinding tool), abrasive jet tools (water jet, air jet), flame cutters, or chisels (jack hammer, sculpting chisel, etc.) for cutting concrete, steel, wood, or stone. The SPIDER can produce large forces with accuracies sufficient for many types of machining operations, including milling, routing, drilling, grinding, and polishing. SPIDER motions could be controlled manually, or by a computer such as currently used for numerically controlled machine tools.

For excavating and grading:

The SPIDER could manipulate digging devices (ditching or trenching machines, digging tools, augers, scrapers) precisely over the ground in either a manual or computer controlled mode. Dirt, stone, concrete, or asphalt could be removed from a large volume with great precision. The robot can easily maneuver loads of several tons. This implies that the SPIDER work platform could carry a gasoline or diesel engine, power transmission system, and tooling for excavating and grading. The SPIDER could also carry a large bucket for removing soil and loading it in trucks or conveyors. SPIDER motions could be controlled manually, or automatically based on data bases generated by computer aided design systems.

For shaping and finishing:

The SPIDER could manipulate grinders, polishers, buffers, paint sprayers, sandblasters, and welding torches over large objects (ship hulls, structural steel, castings and weldments, concrete structures). It can apply controlled amounts of force and resist perturbations in all directions. Motions could be controlled manually, or automatically from computer data base models of objects.

For lifting and positioning:

The SPIDER could be fitted with a variety of gripping devices to lift and precisely position heavy loads such as concrete or steel beams and pillars. The SPIDER can exert controlled forces to mate and seat loads and can resist perturbations such as wind and inertial forces. Precision motions of 2 mm and 0.5° of rotation can easily be achieved while maneuvering large loads.

For flexible fixturing:

The SPIDER work platform is stiff enough to serve as a fixture for holding parts during assembly or construction operations. Parts weighing up to a

ton can be held rigidly to resist or exert lateral forces equivalent to half the weight of the load. The SPIDER can also resist or exert torques.

For transporting manipulators:

The SPIDER stable platform can be used as a stable mobile base to support robotic or teleoperated manipulators. For example, manipulator arms mounted on the SPIDER can be used for handling toxic or radioactive waste or for cleaning-up waste sites. The mobility of the SPIDER support structure allows it to position itself over a waste site while keeping its support wheels away from the contaminated soil.

For fighting oil well fires:

The robot could be used to position a chimney and fire shield, to clear debris and excavate around the well head, and to manipulate tools and valves to extinguish the fire and bring the well under control.

6. Limits of Workspace Study

The term "limits of the workspace" here is meant to refer to those poses of the robot lower platform at which the tension in one or more of the suspension cables become zero. An undesirable result of this situation is that the robot controller loses control over a corresponding number of degrees of freedom.

6.1 Mathematical Model

The basic structure of the robot crane, which consists of the cable support system, is shown in Fig. 8 for the resting steady state position. The overhead support and the suspended platform are represented by two equilateral triangles. In this position both triangles are assumed to be horizontal with their centers of gravity lying on the vertical axis z . The overhead triangle is assumed to be fixed in space and has three vertices located at

$$\begin{aligned}\bar{A}: & (-b, -b\sqrt{3}/3, -h) \\ \bar{B}: & (b, -b\sqrt{3}/3, -h), \\ \bar{C}: & (0, 2b\sqrt{3}/3, -h).\end{aligned}\tag{1}$$

with respect to a Cartesian coordinate frame (x,y,z) , centered at the center of gravity of the lower triangle, when it is positioned at its steady-state, resting-state home pose (see Fig. 8). $2b$ is the length of the side of the overhead triangle and 2α is

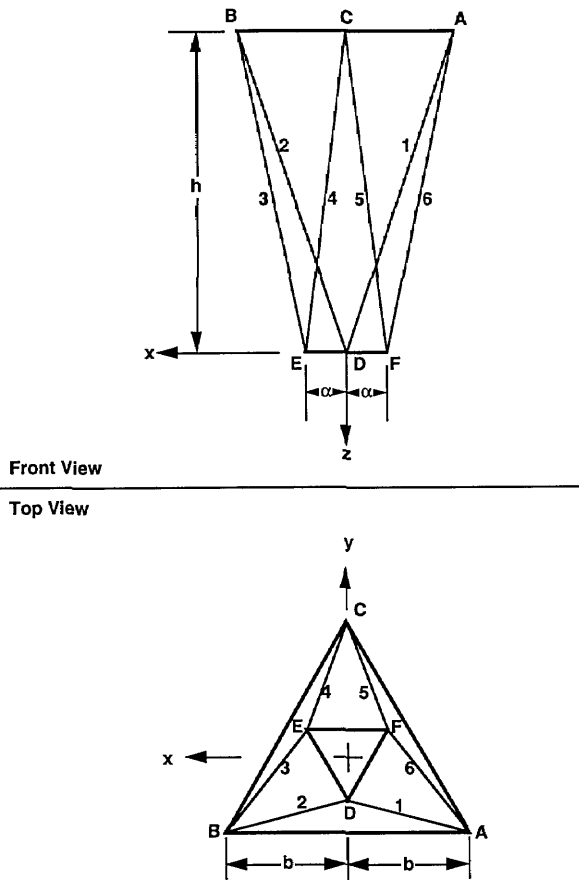


Fig. 8. Robot crane cable support structure.

the length of the side of the lower triangle. The height h is the vertical distance between the two triangles.

The lower triangle, before it is displaced, has three vertices located at

$$\begin{aligned} \bar{D} &: (0, -2a\sqrt{3}/3, 0), \\ \bar{E} &: (a, a\sqrt{3}/3, 0) \\ \bar{F} &: (-a, a\sqrt{3}/3, 0) \end{aligned} \tag{2}$$

with respect to the same coordinate frame.

Let the lower triangle undergo a rigid body motion characterized by three displacements, u_x, u_y, u_z and three successive rotations performed in the following sequence: first, rotation by an angle ϕ about z -axis, then Θ about x -axis, and then Ψ about y -axis. Then it was shown in [1] that after the end of the motion the new coordinates of the vertices of the lower platform are

$$\begin{aligned} \bar{D}' &: (-2aQ_{12}\sqrt{3}/3 + u_x, -2aQ_{22}\sqrt{3}/3 + u_y, -2aQ_{32}\sqrt{3}/3 + u_z), \\ \bar{E}' &: (aQ_{11} + aQ_{12}\sqrt{3}/3 + u_x, aQ_{21} + aQ_{22}\sqrt{3}/3 + u_y, aQ_{31} + aQ_{32}\sqrt{3}/3 + u_z), \\ \bar{F}' &: (-aQ_{11} + aQ_{12}\sqrt{3}/3 + u_x, -aQ_{21} + aQ_{22}\sqrt{3}/3 + u_y, -aQ_{31} + aQ_{32}\sqrt{3}/3 + u_z). \end{aligned} \tag{3}$$

Where Q_{ij} is the i th row, j th column element of matrix Q

$$\bar{Q} = \begin{bmatrix} \cos\Psi \cos\phi - \sin\Psi \sin\Theta \sin\phi & -\cos\Theta \sin\phi & \sin\Psi \cos\phi + \cos\Theta \sin\Theta \sin\phi \\ \cos\Psi \sin\phi + \sin\Psi \sin\Theta \cos\phi & \cos\Theta \cos\phi & \sin\Psi \sin\phi - \cos\Psi \sin\Theta \cos\phi \\ -\sin\Psi \cos\Theta & \sin\Theta & \cos\Psi \cos\Theta \end{bmatrix}$$

The vectors \bar{l}_n' ($n = 1, \dots, 6$) defining the new position of the wires can be found from Eqs. (1) and (3) and are expressed as

$$\begin{aligned} \bar{l}_1' &= \bar{A} - \bar{D}' = (-b + 2aQ_{12}\sqrt{3}/3 - u_x, -b\sqrt{3}/3 + 2aQ_{22}\sqrt{3}/3 - u_y, -h + 2aQ_{32}\sqrt{3}/3 - u_z) \\ \bar{l}_2' &= \bar{B} - \bar{D}' = (b + 2aQ_{12}\sqrt{3}/3 - u_x, -b\sqrt{3}/3 + 2aQ_{22}\sqrt{3}/3 - u_y, -h + 2aQ_{32}\sqrt{3}/3 - u_z) \\ \bar{l}_3' &= \bar{B} - \bar{E}' = (b - aQ_{11} - aQ_{12}\sqrt{3}/3 - u_x, -b\sqrt{3}/3 - aQ_{21} - aQ_{22}\sqrt{3}/3 - u_y, -h - aQ_{31} - aQ_{32}\sqrt{3}/3 - u_z) \\ \bar{l}_4' &= \bar{C} - \bar{E}' = (-aQ_{11} - aQ_{12}\sqrt{3}/3 - u_x, 2b\sqrt{3}/3 - aQ_{21} - aQ_{22}\sqrt{3}/3 - u_y, -h - aQ_{31} - aQ_{32}\sqrt{3}/3 - u_z) \\ \bar{l}_5' &= \bar{C} - \bar{F}' = (aQ_{11} - aQ_{12}\sqrt{3}/3 - u_x, 2b\sqrt{3}/3 + aQ_{21} - aQ_{22}\sqrt{3}/3 - u_y, -h + aQ_{31} - aQ_{32}\sqrt{3}/3 - u_z) \\ \bar{l}_6' &= \bar{A} - \bar{F}' = (-b + aQ_{11} - aQ_{12}\sqrt{3}/3 - u_x, -b\sqrt{3}/3 + aQ_{21} - aQ_{22}\sqrt{3}/3 - u_y, -h + aQ_{31} - aQ_{32}\sqrt{3}/3 - u_z) \end{aligned}$$

The balance of forces acting on the lower platform requires that

$$\vec{f} + \sum_{n=1}^6 \vec{f}_n = 0 \tag{6}$$

where \vec{f} is the external force applied at the center of gravity of the platform. \vec{f} is equivalent to \vec{W} for this case. The directions of the wire tensions \vec{f}_n are given by the corresponding vectors of Eq. (5).

The balance of moments acting on the lower platform requires that

$$\begin{aligned} \vec{m} + \vec{QD} \times (\vec{f}_1 + \vec{f}_2) + \vec{QE} \times (\vec{f}_3 + \vec{f}_4) \\ + \vec{QF} \times (\vec{f}_5 + \vec{f}_6) = 0 \end{aligned} \tag{7}$$

where \vec{m} is the external moment applied upon the lower platform. \vec{m} is zero for the workspace limit study and the only externally applied force is the single load of weight W suspended from the centroid of the lower platform.

Two conditions under which two of the cables always become loose for any value of the weight W have been identified.

6.2 Condition #1

Figure 9 shows the position of the lower platform under which the tensions in two of its suspension cables (2 and 3) go to zero. For this condition to occur the vector of the weight W must cross a vertical plane through one of the suspension lines AC or AB or BC. These suspension lines are defined by the three suspension points A, B, and C. From each of these points two suspension cables originate. So each suspension line supports four cables. For example, in the case of line AC shown in the Fig. 9, cables 1, 4, 5, 6 all intersect a vertical plane that includes AC and only these four cables are in tension.

The sum of the moments of all the cable tensions about K, which is the point at which the vector of the weight W intersects a vertical plane that includes the suspension line AC (see Fig. 9) is

$$\vec{KD} \times (\vec{f}_1 + \vec{f}_2) + \vec{KE} \times (\vec{f}_3 + \vec{f}_4) + \vec{KF} \times (\vec{f}_5 + \vec{f}_6) = 0. \tag{8}$$

The projections of these moment vectors on AC can be calculated by multiplying with U_{ac} which is the unit vector defining the orientation of AC.

$$\begin{aligned} \{U_{ac}(\vec{KD} \times \vec{f}_2 + \vec{KE} \times \vec{f}_3)\} + \{U_{ac}(\vec{KF} \times (\vec{f}_5 + \vec{f}_6) \\ + \vec{KD} \times \vec{f}_1 + \vec{KE} \times \vec{f}_4)\} = 0. \end{aligned} \tag{9}$$

But

$$\{U_{ac}(\vec{KF} \times (\vec{f}_5 + \vec{f}_6) + \vec{KD} \times \vec{f}_1 + \vec{KE} \times \vec{f}_4)\} = 0. \tag{10}$$

Since U_{ac} is orthogonal to the vector inside the parenthesis. Thus

$$\{\vec{U}_{ac}(\vec{KD} \times \vec{f}_2 + \vec{KE} \times \vec{f}_3)\} = 0. \tag{11}$$

The only way for Eq. 11 to be true is if $\vec{f}_2 = \vec{f}_3 = 0$, or cables 1, 2 and 3, 4 to be horizontal or cables 2 and 3 to cross the suspension line AC. Since the controller will never allow any cables to become horizontal or cross a suspension line, $\vec{f}_2 = \vec{f}_3 = 0$ is the only possible solution. This has to be true for any W and feasible platform orientation.

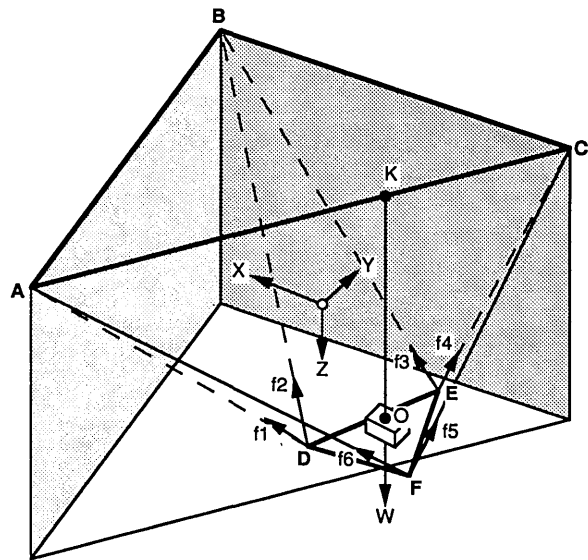


Fig. 9. Condition #1—work-volume edge detection.

6.3 Condition #2

Figure 10 shows another position of the lower platform under which the tensions in two of its suspension cables go to zero and the corresponding cables become loose (cables 3 and 6). In this case the four-cables crossing line GHLM is an imaginary one defined by the intersection of the planes defined by the two pairs of the active cables (1, 2 and 4, 5). In the case of the Fig. 10, plane ADB and FEC. As soon as the vector of W crosses that line cables 3 and 6 become loose. The explanation is the same given in Sec. 6.2.

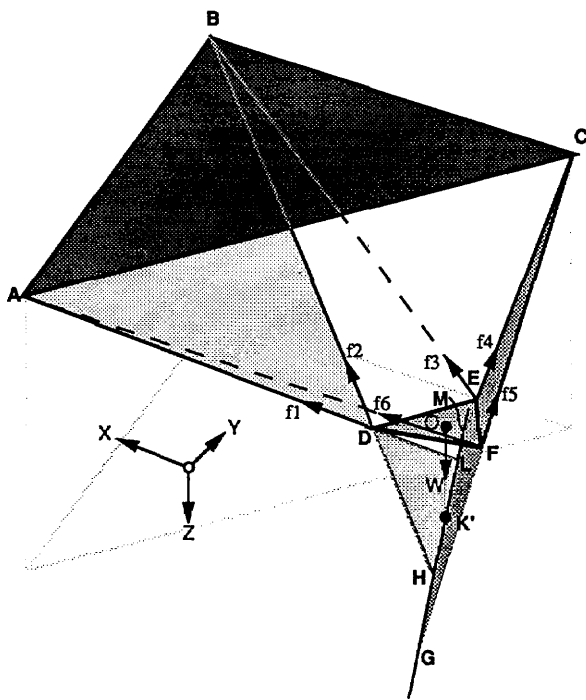


Fig. 10. Condition #2—work-volume edge detection.

7. Experiments Performed

Experiments were done on the SPIDER to measure payload, work volume, and platform-movement precision. A weight of 455 kg (1000 lb) was maneuvered by the SPIDER platform while in manual mode. The load was carried to the limits of the work volume until cables began to go slack.

As discussed in Sec. 4, two conditions whereby cables begin to go slack can be shown mathematically. As the cables begin to go slack, a point on the edge of the workvolume is defined. Experiments to define this volume were done to verify the mathematics of this phenomena.

Cable loosening conditions #1 and #2 were tested for total platform weights of 68 and 455 kg. The platform was moved to cover a quarter of the workspace at an arc of 90°. For condition #2, strings were attached to the cables to extend their length and locate the approximate position of the four-cables crossing line and its intersection with a plumb-line suspended from the centroid of the platform.

A cable loosening computer simulation program has also been developed which is being used to search for the locus of the platform poses satisfying condition #2.

Another experiment that was performed involved the platform-movement precision and stability. A chain saw was attached to the work platform (see Fig. 11) at a 30° angle from the vertical axis and with the tip of the chain saw blade at the center of gravity of the work platform. The saw was attached to a 3 mm thick steel plate that acted as a leaf-spring. While in the manual mode, depth of cut to within 1 mm could be made in a solid oak log. Deep cuts could also be made with ease either with the blade tangent to, or perpendicular to the oak log surface. With the stability of the platform, little vibration was seen on the chain saw or the steel leaf-spring plate even while driving the tip of the chain saw blade directly into the oak log.

8. Summary and Conclusions

The SPIDER robot is a variation of the robot crane design presented in previous reports. Theoretical, computer, and experimental studies of the possible use of this type of robot are given. A preliminary investigation of the limits of its work-space and the current version of its controller are discussed. Several tests were performed to verify the theoretically predicted limits of the work-space.

Work volume measurements verified that cables go slack due to conditions 1 and 2. During this experiment, a payload of 455 kg was carried through the work volume with ease. No strain on the winches was observed while picking up such a load.

The SPIDER can be used for a number of general tasks:

- cutting
- excavating and grading
- shaping and finishing
- lifting and positioning
- flexible fixturing
- transporting manipulators

These capabilities can be targeted for a variety of specific applications such as: fighting oil well fires or hazardous waste site inspection and clean-up.

A number of advantages of the SPIDER over current technology are:

- rigid support and precise maneuverability of large loads
- remote positioning of tools and equipment
- executing precise motions with tools and equipment to accomplish complex tasks
- high lift-to-weight ratio
- resistance to environmental perturbations
- accurate control of loads by a novice operator
- reduced crew size



Fig. 11. Chain saw mounted on a “leaf-spring” steel plate that is attached to the platform. Note the cuts in the oak log beneath the saw.

Future research on SPIDER will include integrating more advanced sensing capability, such as machine vision, and additional mechanical analysis and testing. The long range goal is to build a full-scale working prototype jointly with an industrial partner.

Acknowledgments

The authors would like to acknowledge the efforts of the following people who worked on the SPIDER: Charles Giauque, Andrew McCullough, Wendell Wallace, Tom Wheatley, Tsung-Ming

Tsai, and Roger Kilmer. Only with their combined efforts could the SPIDER have been built and tested for demonstration in the short period of time available.

9. References

- [1] N. G. Dagalakis, J. S. Albus, K. R. Goodwin, J. D. Lee, T. Tsai, H. Abrishamian, and R. V. Bostelman, Robot Crane Technology Program—Final Report, NIST Technical Note 1267, Natl. Inst. Stand. Technol., Tech. Note 1267, July 1989.
- [2] N. G. Dagalakis, J. S. Albus, B. L. Wang, J. Unger, and J. D. Lee, Stiffness Study of a Parallel Link Robot Crane for

Shipbuilding Applications, Trans. ASME J. Offshore Mechanics Artic Eng. 111, (3), 183-193 (1989).

- [3] J. Unger and N. G. Dagalakis, Optimum Stiffness Study for a Parallel Link Robot Crane Under Horizontal Force, Proceedings of the Second International Symposium on Robotics and Manufacturing Research, Education and Applications, Albuquerque, NM, November 16-18, 1988.
- [4] D. Stewart, A Platform with Six Degrees of Freedom, Proc. Inst. Mechanical Eng. Part I, 180 (15), 371-386 (1965-1966).
- [5] S. E. Landsberger, Design and Construction of a Cable-Controlled Parallel Link Manipulator, Master's Thesis, Dept. of Mechanical Engineering, Massachusetts Institute of Technology, September 1984.
- [6] S. E. Lansdberger and T. B. Sheridan, A New Design for Parallel Link Manipulators, Proc. Sys. Man. and Cybernetics Conf., Tucson, AZ, November 1985, pp. 812-814.

About the authors: Dr. James S. Albus is Chief of the Robot Systems Division (RSD), Manufacturing Engineering Laboratory at NIST. RSD has a staff of approximately 50 people involved in research on real-time control systems, sensory processing, world modeling and simulation for advanced robotics, and automated manufacturing applications. Mr. Roger V. Bostelman is a Electronics Engineer in the systems Integration Group of the Robot Systems Division, Manufacturing Engineering Laboratory at NIST. Dr. Nicholas Dagalakis is a Mechanical Engineer in the Performance Measures Group of the Robot Systems Division, Manufacturing Engineering Laboratory at NIST. The National Institute of Standards and Technology is an agency of the Technology Administration, U.S. Department of Commerce.

Conference Report

WORKSHOP ON CHARACTERIZING DIAMOND FILMS Gaithersburg, MD February 27-28, 1992

Report prepared by

Albert Feldman

National Institute of Standards and Technology,
Gaithersburg, MD 20899

Charles P. Beetz

Advanced Technology Materials,
7 Commerce Dr.,
Danbury, CT 06810

Michael Drory

Crystallume,
125 Constitution Dr.,
Menlo Park, CA 94025

and

Sandor Holly

Rockwell International,
6633 Canoga Ave.,
Canoga Park, CA 91304

1. Introduction

A workshop was held at NIST on February 27-28, 1992 to discuss specific topics deemed important to the characterization of diamond films

made by chemical vapor deposition (CVD) and to address the need for standards in diamond technology. The workshop was held as a follow-up to a recommendation in a recent report assessing diamond technology in Japan [1]. The audience targeted for this workshop was the producers and potential users of CVD diamond technology in the United States. University scientists were invited as experts in properties measurements. There were 35 participants in the workshop.

The workshop consisted of two components, technical presentations by active researchers on topics of the most immediate relevance to commercial applications and presentations by companies describing their needs for standards.

Rather than choose a wide variety of topics for discussion, we focussed on two technical topics, the measurement of thermal conductivity or thermal diffusivity for heat dissipation applications, and the measurement of mechanical properties of diamond for cutting tool applications. These properties are important for other applications as well. The topics were selected on the basis of responses to a questionnaire sent to potential participants in the workshop. Presentations describing the NIST Advanced Technology Program and NIST facilities that might be useful to diamond researchers were also given.

After the workshop, an evaluation form was sent to all registrants. The purpose of the form was to determine the usefulness of the workshop, the desire for further workshops, and the need for standards related activities. The results of this questionnaire will be included in a NIST Internal Report to be distributed to workshop participants.

The sections that follow contain summaries of the three main sessions of the workshop. The principal conclusions to be drawn from the workshop include the following:

- There is a need to standardize characterization methods so that experimental data, measured at different sites by different workers, may be meaningfully compared.
- There is a need for specimens with well characterized properties. The first priority identified was a need for specimens to measure thermal conductivity or thermal diffusivity in interlaboratory round-robin comparisons. Development of a Raman standard reference material would also be useful for assessing diamond quality.
- Standards for mechanical measurements would be premature at present. Only a limited number of measurements of specific properties, such as fracture toughness and hardness, have been made. Because of the great hardness of diamond, mechanical measurements are difficult to make and difficult to interpret.
- Other workshops should be held at intervals of about 1 year, focusing on other topics, such as optical and electrical properties.
- Working groups dealing with standards for specific topical areas should be established, possibly under the auspices of a standards organization such as ASTM.
- NIST has an important role to play in coordinating and facilitating the development of standards for diamond technology and in developing standard reference materials.

2. Thermal Properties Measurement

The session on thermal properties consisted of eight speakers presenting different measurement techniques.

The first paper was given by John Graebner from AT&T Bell Laboratories. He gave a brief review of the physical mechanisms responsible for thermal conductivity in diamond and then discussed measurements of thermal conductivity he has made on natural single crystal diamonds and on CVD diamond films. Results of thermal conductivity measurements obtained with three different techniques were presented. Dr. Graebner showed that the thermal conductivity varied through the thickness dimension of a CVD diamond film; the bottom surface, the surface where film growth began, had one fourth the thermal conductivity of the top surface. Moreover, the thermal conductivity was anisotropic; the thermal conductivity for heat flow parallel to the specimen surfaces was lower than the thermal conductivity for heat flow

perpendicular to the specimen surfaces. In a film 300 μm thick the thermal conductivity near the top surface was found to be $22 \text{ W} \cdot \text{cm}^{-1} \cdot \text{K}^{-1}$, which is comparable to the value for high quality single crystal diamonds. By modeling the dependence of the thermal conductivity on grain size, he predicted thermal conductivity of $25\text{--}28 \text{ W} \cdot \text{cm}^{-1} \cdot \text{K}^{-1}$ for 1 mm sized grains, an interesting result because these values are unexpectedly large.

The second speaker was Jan Vandersande from the Jet Propulsion Laboratory, who discussed the temperature dependence of the thermal conductivity of white natural diamonds. Thermal diffusivity measurements were made from room temperature to 1000 K by means of a flash lamp measurement technique. The room temperature thermal conductivity was $23 \text{ W} \cdot \text{cm}^{-1} \cdot \text{K}^{-1}$ and at 1200 °C was $5 \text{ W} \cdot \text{cm}^{-1} \cdot \text{K}^{-1}$. This technique can also be used to measure the specific heat. As an aside, Dr. Vandersande demonstrated that due to instrumentation limitations, the true electrical resistivity of diamond can be much larger than measurements would indicate.

David Cahill from the University of Illinois discussed measuring thermal conductivity by an ac measurement technique, called the 3-omega method. In this method, a thin metal wire is deposited onto the diamond surface. The wire with electrical resistance, R , acts both as the heat source and as the thermometer. An alternating current, I , produces resistive heating, I^2R ; the resultant temperature rise in the specimen produces a change in resistance of the wire. This change in resistance is a measure of the temperature. The technique is called the 3-omega method because the measurements are made at the third harmonic of the ac current frequency. This technique is immune to the effects of thermal radiation and is well suited for measurements both on bulk specimens or on thin films. Dr. Cahill measured the thermal conductivity of a range of carbon based materials, including C_{60} ; the values spanned four orders of magnitude.

Ronald Tye, a consultant to Sinku-Riko, discussed a commercially available instrument that uses a modified ac calorimetry method based on optical heating to measure both the thermal diffusivity and the heat capacity of thin films. Dr. Tye showed results for diamond films and for standard samples of nickel, silicon, alumina, and stainless steel.

Donald Morelli of the General Motors Research Laboratories showed how thermal conductivity measurements can be used to study defects in diamond. He reviewed the sources of error in the

classic steady state method of measuring thermal conductivity. Results of thermal conductivity measurements conducted over a range of temperatures down to cryogenic temperatures on films deposited by plasma assisted CVD and hot filament CVD were reported. Although the films prepared by the two methods were alike in almost all respects, the films prepared by the hot filament method showed an anomalous behavior at low temperature that has not yet been explained.

P. K. Kuo of Wayne State University discussed the measurement of the thermal diffusivity of diamond by the method of photothermal deflection. In this technique, a probe laser beam skimming the surface of the specimen is deflected by refractive index gradients that occur in the air above the specimen due to heating from a thermal wave propagating in the specimen. Results were reported for diamond films down to 5 μm thick and for synthetic single crystal diamonds about 3.5 mm thick. Values of thermal diffusivities ranged from less than 1 to 9.2 $\text{cm}^2 \cdot \text{s}^{-1}$. Dr. Kuo also discussed a modification to the technique in which the probe beam passes directly through the crystal under measurement.

Grant Lu from the Norton Company discussed the requirements for a measurement technique that could be used effectively as a process monitor or a quality control monitor. First he described the converging thermal wave technique that he uses to measure thermal diffusivity. Then he discussed the results of a thermal conductivity round-robin, in which diamond samples taken from a contiguous section of a 10 cm diameter diamond plate were sent to several laboratories for thermal conductivity measurements. Each laboratory used a different method of measurement. The values of thermal conductivity displayed considerable scatter, generally ranging from 12.3 to 16.7 $\text{W} \cdot \text{cm}^{-1} \cdot \text{K}^{-1}$ with one result greater than 20 $\text{W} \cdot \text{cm}^{-1} \cdot \text{K}^{-1}$. The cause of the scatter in the data was discussed but not resolved.

A. Feldman from NIST discussed the use of photothermal radiometry for measuring the thermal diffusivity of diamond. Two different geometries for making the measurement were discussed, one using a laser heating beam with a cylindrically symmetric Gaussian profile and another using a laser heating beam with a cylindrically symmetric ring profile which results from placing an axicon lens into the beam. The results of numerical simulations for the phase and magnitude of the surface temperature as a function of the chopping frequency of the laser were presented. He

also discussed the importance of knowing the laser beam characteristics and the importance of having the sample precisely focussed on the detector.

3. Mechanical Properties

Characterizing the mechanical properties of CVD diamond requires that several broad topical areas be explored. These include elastic properties, plastic properties, and fracture properties.

In the case of a composite system, such as diamond/silicon, interface properties are an additional consideration. Examples of elastic properties to be examined include Young's modulus and Poisson's ratio. The hardness is a primary measure of plastic behavior, while fracture toughness characterizes the fracture behavior of a material. In this workshop, each broad area of mechanical behavior was briefly considered for the purpose of assessing the status of testing methods and practices in preparation for standards. As described below, several areas of mechanical characterization of CVD diamond are generally unexplored, requiring considerably more attention in coming years.

Of the mechanical properties, the elastic behavior of CVD diamond has received the most attention by researchers because of the potential benefits diamond brings to window applications. Recent work on the elastic properties of CVD diamond was presented by C.A. Klein of Raytheon in which attention was directed toward the elastic constants of polycrystalline diamond derived from single crystal values. Dr. Klein emphasized the considerable range in measured values of Young's modulus obtained by different researchers. He pointed out the need for careful sample description and careful analysis of the test method. In addition, he pointed out that the Poisson's ratio should be 0.07 rather than 0.2, the latter value being often cited in the literature.

Considerable work has been done on the plastic behavior of CVD diamond. Presentations by C. V. Cooper of United Technologies and C. J. McHargue of the University of Tennessee discussed the use of nanoindentation to obtain the hardness of CVD diamond. The dependence of hardness on process variables, such as the amount of methane in the deposition feed gas, were discussed. Dr. Cooper discussed the experimental difficulties caused by surface roughness. Dr. McHargue discussed the experimental difficulties associated with the choice of indenter geometry. Dr. McHargue also pointed out the necessity of

relating a particular test procedure to a specific definition of hardness.

The fracture behavior of CVD diamond was discussed in several of the presentations. J. J. Mecholsky of the University of Florida and P. Klocek of Texas Instruments discussed the measurement of the *film* fracture toughness by means of a surface analysis technique, while M. D. Drory discussed an indentation method. Professor Mecholsky's method showed considerable potential for determining the fracture toughness for a variety of specimen geometries, without the need for special specimen preparation.

M. D. Drory discussed quantifying adhesion through the measurement of *interface* fracture toughness. In particular, a first-order analysis was presented for determining interface toughness from a brale indentation measurement. The test was applied to diamond on relatively ductile substrates, such as cemented carbide. Considerably more work is needed to develop adhesion tests suitable to diamond.

4. The Need for Standards

There are several good reasons to establish standards for the evolving field of CVD diamond film technology. One of the purposes of this workshop was to identify the needs for standards in industry. Representatives of six companies agreed to discuss their views on this subject. The speakers were J. W. Mitchell of AT&T Bell Laboratories, M. D. Drory of Crystallume, K. Gray of Norton Diamond Films, S. Holly of Rockwell International, P. Klocek of Texas Instruments, and C. J. Robinson of the Raytheon Company. All of the companies are currently conducting CVD diamond film research. While some of the companies are commercial producers of the material, others are users of CVD diamond and are applications oriented.

The presentations described the current methods of characterizing diamond films used by these companies and the importance of the measurements to quality assurance of the CVD diamond material as related to a variety of company specific applications. The most important application areas discussed were thermal (heat sinks), optical (infrared windows and domes), tribological, and electronic.

All of the presenters agreed on the value of standards to meet performance criteria in different applications. There is a need to standardize the characterization methods so that experimental

data, measured at different sites by different workers, may be meaningfully compared. To that end, a discussion began on the value of round-robin type tests, where the same sample is measured by different laboratories, often using different measuring methods. The importance of thorough documentation of the methods used in these measurements was emphasized. In fact, the question of what "thorough documentation" means directly emphasized the need for standards, the focus of this workshop.

It became obvious during these discussions that different applications require different types of measurements. There was also a general consensus that measurements procedures bridging different disciplines are needed. Because of the interdisciplinary requirements of the technology, the activities of workers with different areas of expertise will require coordination. These workshops provide such a forum.

It may be practical or it may even be necessary to form specialty groups to formulate standards in separate application areas. Development of standards would start with the definition of simple concepts, such as the meaning of "high quality diamond" and the interpretation of a particular characterization, such as a Raman spectrum or a thermal conductivity measurement.

In order for the industrial community to derive immediate benefits from these standardization activities it will be important to promote exchange of information through meetings and publications. It was also proposed that a data base of CVD diamond material properties, based on accepted "standardized" methods, be established. The data base would require updating on a continual basis.

There was general agreement during the discussions in this session, that focussing on just one characteristic at a time was most valuable. The previous day's session on thermal properties, which contained technical papers describing methods of measuring thermal conductivity of CVD diamond, was an excellent example of the value and necessity of focusing on a single characteristic. Agreement was reached among many workshop participants, that future workshops on standardization should highlight other characteristics, such as optical or electrical properties.

A pertinent final presentation in this session was made by E. S. Etz of NIST who discussed development of a Standard Reference Material for Raman spectroscopy of CVD diamond [2]. It was generally agreed that such a standard would be useful. Questions to be considered are: how many

specimens would be needed, how should the specimens be obtained, what specimen dimensions are needed, and how extensively should the specimens be characterized by other methods?

5. References

- [1] A. Feldman and L. H. Schwartz, eds., U.S. Assessment of the New Diamond Technology in Japan, Natl. Inst. Stand. Technol. Special Publication 807.
- [2] E. S. Etz, in Applications of Diamond Films and Related Materials, Y. Tzeng, M. Yoshikawa, M. Murakawa, and A. Feldman, eds., Elsevier Science Publishers B. V. (1991).

News Briefs

General Developments

Inquiries about News Briefs, where no contact person is identified, should be referred to the Managing Editor, Journal of Research, National Institute of Standards and Technology, Administration Building, A635, Gaithersburg, MD 20899; telephone: 301/975-3572.

NEW WAYS NEEDED TO TEST FIRE SAFETY OF WIRING

Most electrical wire and cable tests tell little or nothing about their performance during a fire or whether they would pose a danger to building occupants, NIST researchers say. To get a better picture, the researchers recommend using techniques that measure physical properties (such as the rate at which a material releases heat and the amount of smoke and toxic gas produced) in conjunction with computer modeling. In the first phase of a study for the National Electrical Manufacturers Association, more than 100 standard tests and laboratory studies used in the United States and abroad were examined. In the next phase, physical property measurements will be used with NIST's HAZARD I computer model to evaluate wire and cable products. A report, *Fire Performance of Wire and Cable: Reaction-to-Fire Tests—A Critical Review of the Existing Methods and of New Concepts* (NIST Technical Note 1291), is available for \$26 prepaid from the National Technical Information Service, Springfield, VA 22161. Order by PB 92-141563.

NEW "FREEWARE" COMPUTES SIGNAL FREQUENCIES

Chemists, physicists, and astronomers have long used complex mathematical equations to make sense of their observations. When their observations fall into random, fluctuating patterns—like

ocean waves or temperature changes—a mathematical operation called the Fourier transform is especially helpful. This type of analysis breaks the patterns into sine waves with varying frequencies, amplitudes, and phases. The Fourier transform, named for the French mathematician who invented it in 1807, enables scientists to determine the amplitude and phase at each sine wave frequency. Commercially available software can perform Fourier transforms rapidly, but details cannot be changed by the user. However, a NIST engineer is distributing his own program as freeware to enable the user to better understand the details of the transform and its accuracy. Spectrum V 1.0 is available with a manual and source code so the user can modify it as desired. It is written in FORTRAN for IBM-PC or compatible computers. To request a copy of Spectrum, contact David E. Hess, Rm. 105, Fluid Mechanics Building, NIST, Gaithersburg, MD 20899, 301/975-5937, fax: 301/258-9201, Email: Hess@ENH.NIST.GOV.

REPORT OFFERS GUIDELINES ON FTAM IMPLICATIONS

The Government Open Systems Interconnection Profile, Federal Information Processing Standard 146-1, specifies that federal agencies acquiring File Transfer, Access, and Management (FTAM) systems procure products that conform to international standard ISO 8571. But which FTAM implementation will best suit a user's function and performance requirements? NIST offers help in a new report produced by agency scientists. The document compares procurement of FTAM products to buying a new car. Using this analogy, the authors walk the reader through each step of the FTAM evaluation process. The report contains a tutorial on FTAM and a detailed section describing many functions potentially available in FTAM implementations (override or access

passwords, for example). Also included is an extensive appendix containing suggested FTAM experiments, a glossary, and abbreviations. Guidelines for the Evaluation of File Transfer, Access, and Management Implication (NIST Special Publication 500-196), is available for \$19 (print) or \$9 (microfiche) prepaid from the National Technical Information Service, Springfield, VA 22161. Order by PB 92-126580/AS.

DO IRREGULAR PIPES AFFECT FLOW MEASUREMENTS?

Small inaccuracies in meter measurements can translate into million-dollar-a-day losses in the custody transfer of fuels and other valuable chemical fluid products. Ideally, flow meters are installed on long, straight pipes for the most accurate readings. But pipes, whether for water, natural gas, or chemical products, do not always follow ideal configurations. As part of a consortium with flow meter manufacturers and flow meter users, NIST researchers are assessing how placing flow meters near elbows, tees, and other bends affects their performance. Two new reports that document this research are available. The first is Tube Bundle Effects (NISTIR 4751), available from the National Technical Information Service, Springfield, VA 22161 for \$17 (print) or \$9 (microfiche) prepaid. Order by PB 92-149855. The second publication, TEE Used As An Elbow Configuration (NISTIR 4753), is available from NTIS for \$19 (print) or \$9 (microfiche) prepaid. Order by PB 92-149848.

INSULATION PROGRAM COVERS ENTIRE BUILDING ENVELOPE

The NIST National Voluntary Laboratory Accreditation Program (NVLAP) for thermal insulation materials (TIM) has been expanded to cover the integrity of the entire building envelope. The new thermal insulation and building envelope materials program (TIB) now includes test methods for thermal insulation, windows, doors, seals and sealants, and other materials that contribute to the energy performance of a building. Eleven test methods were added to the TIM program at the request of an independent testing laboratory accredited by NVLAP. Other appropriate fields and test methods for building envelope materials may be added to the program under NVLAP procedures. For information on the expanded TIB program, contact Lawrence S. Galwin, Rm. A124, Building 411, NIST, Gaithersburg, MD 20899, 301/975-4016, fax: 301/926-2884.

TWENTY-SEVEN GRANTS ANNOUNCED FOR ATP'S 2ND YEAR

Commerce Secretary Barbara Hackman Franklin on April 21 announced the second set of grants under the Commerce Department's Advanced Technology Program (ATP). The NIST-administered grants to private industry are designed to stimulate research and development of cutting-edge, generic technologies with significant commercial promise. Twenty-seven new programs were selected for funding under the ATP, including proposals in advanced materials, biotechnology, computing, electronics, and high-temperature superconductivity. The awards will provide approximately \$25 million in first-year grants to initiate nearly \$190 million in R&D programs over the next 5 years. More than half of the cost will be paid by sponsoring firms.

PROGRAM ANNOUNCED FOR PRECISION CASTING OF ALLOYS

A cooperative research and development program to improve the casting of metal alloys commonly used in the aerospace industry has been proposed by NIST in cooperation with the Aerospace Industries Association and the National Center for Advanced Technology. The goal is to plan and undertake research on precision casting so that the planning, research, and technology transfer can be coordinated and brought quickly to manufacturers. The consortium will be a cooperative, distributed effort by industry, universities, and other government agencies. Research will be carried out in-house by consortium members as well as by NIST. Companies should be prepared to invest adequate resources and be firmly committed to the goal of developing new casting technology. Participation in the program will require a \$10,000 annual contribution per year to cover administrative costs (not required by university participants) and in-kind research contributions to the consortium. For information, contact H. Thomas Yolken, Office of Intelligent Processing of Materials, B344 Materials Building, NIST, Gaithersburg, MD 20899, 301/975-5727.

3-D COMPUTER MODEL PREDICTS OIL FIRE "FOOTPRINTS"

A new simulation model developed by NIST fire researchers and mathematicians predicts in three dimensions the airborne concentration of smoke particles billowing off major oil fires. The model also calculates the unique smoke "footprint"—the distribution of smoke particles falling to the

ground—for fires of varying sizes and occurring under different wind conditions. The model is part of a larger project to find better ways to rapidly clean up large oil spills. One possible solution is to burn the spilled oil. With funding from the Minerals Management Service, the U.S. Coast Guard, and the American Petroleum Institute, NIST researchers are studying what happens during burning, what is left on the water after the oil has burned, and what goes into the air. This project aims to give local authorities the information on distribution of smoke and oil residue they need to decide if burning an oil spill would cause less environmental damage than other clean-up options.

WOOD PRODUCTS INDUSTRY DEFINES FEDERAL ROLE

Private-sector panelists from a NIST/industry workshop recently made several recommendations for an active federal role assisting in conformity assessment activities in order to gain acceptance of U.S. products in international markets such as the European Community (EC). Government, said the panel, should serve as a clearinghouse for information on conformity assessment requirements in the EC; establish a wood products sector advisory committee to assist the development of U.S. negotiating positions with the EC; take an active role in accrediting U.S. programs to satisfy EC directives; negotiate with the EC on the scope and authority of EC notified bodies to subcontract product testing and quality assessment to qualified U.S. testing and inspection agencies; and assist industry in developing a national accreditation program for testing and certification. The panel's report, Conformity Assessment Workshop on Wood Products (NISTIR 4771), is available from the National Technical Information Service, Springfield, VA 22161 for \$19 prepaid. Order by PB 92-162544.

NINETY COMPANIES VIE FOR 1992 BALDRIGE AWARD

NIST has announced that 90 companies have applied for the 1992 Malcolm Baldrige National Quality Award. The number includes 31 manufacturing firms, 15 service companies, and 44 small businesses. Last year, 106 companies applied and three won. The award, named for the late Commerce Secretary Malcolm Baldrige, was established by legislation in August 1987. It promotes national awareness about the importance of improving quality management and recognizes quality achievements of U.S. companies—though the award is not for specific products or services. Firms applying must undergo a rigorous examina-

tion. On-site visits for those passing an initial screening will take place in September and will be followed by an announcement and award ceremony in the fall. In previous years, the awards have been presented by the president or vice-president during a ceremony in Washington, DC. The award program is managed by NIST with the active involvement of the private sector. A maximum of two awards may be given annually in each of three categories: manufacturing, service, and small business.

GUNPOWDER "FINGERPRINTS" COULD CATCH CROOKS QUICKER

Efforts to curb violent crime could soon get a boost from NIST scientists who, in collaboration with the National Institute of Justice, are developing a rapid, inexpensive way to prove whether or not a suspect has fired a weapon. The technique, known as micellar electrokinetic capillary electrophoresis (MECE), takes less than 1 h. Current forensic laboratory methods can take days, requiring expensive equipment and dust-free clean rooms. Instruments for MECE cost less and tests could be done in most major police labs, says a NIST chemist. To perform the test, a police officer would lift gunshot residue from a suspect's hands with masking tape. Investigators would then dissolve residue particles from the tape and pass them through a thin capillary. An electric field forces compounds in the particles to separate, resulting in a unique pattern, or "fingerprint."

TWO MIXTURES COULD REPLACE BANNED REFRIGERANT

NIST researchers say two refrigerant mixtures appear promising as environmentally safe replacements for R22, a refrigerant widely used in residential heat pumps. The Clean Air Act of 1990 calls for hydrochlorofluorocarbons (HCFCs), such as R22, to be phased out starting in 2015. HCFCs belong to a family of chemicals believed to be damaging to the Earth's atmosphere. The two mixtures, named R32/R134a and R32/R152a, do not contain chlorine or bromine, the two main catalysts some believe are destroying the Earth's ozone layer. The researchers used a NIST-developed computer simulation program, called CYCLE11, and a laboratory version of a heat pump to examine how the mixtures would perform in the machine. The NIST study showed that the two mixtures could perform up to 15 percent better than R22. NIST is currently conducting flammability testing to evaluate the one possible drawback, the fact that both mixtures contain at least one flammable component.

COMMENT PERIOD EXTENDED FOR PROPOSED CASE PROGRAM

NIST is extending the deadline for public comments on the proposed conformity assessment systems evaluation (CASE) program from May 26, 1992 to July 24, 1992. The voluntary program is intended as a mechanism to provide federal assurances to the Commission of the European Communities and other governments of the competency of qualified U.S. conformity assessment activities related to laboratory testing, product certification, and quality systems registration. Written remarks about the proposed CASE program must be submitted by July 24, 1992. Comments and requests for information should be sent to Stanley I. Warshaw, director, Office of Standards Services, A306 Administration Building, NIST, Gaithersburg, MD 20899, 301/975-4000, fax: 301/963-2371.

HOW FAST DOES A LEAK LEAK? ASK NIST

A tiny leak can be a huge problem for food packagers, pharmaceutical companies, and aerospace engineers. Minuscule holes in food wrappers or fuel sealers can result in illness, accidents, or even death. For this reason, manufacturers carefully test their packaging and products for the tiniest of leaks. The tests compare leakage from the product against a known leakage rate from a specially designed gas cylinder, known as a "standard leak." Many of these standard leaks have been calibrated in a 6 year old program at NIST. The program began with NIST's involvement in providing leak calibration services at Three Mile Island, where scientists assisted in an investigation of potential leakage from railroad cars carrying waste materials. NIST scientists describe the leak calibration service in a new technical report, NIST Measurement Services: NIST Leak Calibration Service (Special Publication 250-38). Available from the National Technical Information Service, Springfield, VA 22161, 1-800-336-4700. Order by PB 92-149772; for \$19 prepaid.

U.S., ITALY AGREE ON GAS PRESSURE STANDARD

NIST and the Istituto di Metrologia "G. Colonnetti" of the Consiglio Nazionale delle Ricerche, signed an agreement on May 8, 1992, recognizing the equivalency of their national standards for pressure in gas and liquid media as defined by the International System of Units (SI). Based on interlaboratory comparisons, the new agreement marks the eighth equivalency recognition between NIST and Italian national standards laboratories. NIST and

the Istituto di Metrologia also extended an agreement for their temperature scales to cover the range of 13.8 to 1235 K. They have one for length. Also on May 8, NIST and the Istituto Elettrotecnico Nazionale "Galileo Ferraris" (IEN), renewed recognition of their national standards for electrical resistance. NIST and IEN recognize the equivalency of their national standards for luminous intensity, voltage, electrical capacitance, and time. The U.S. and Italy are signatories of the Convention of the Meter and determine their basic units of measurements in accordance with definitions for SI units adopted by the General Conference of Weights and Measures.

GOVERNMENT INVENTIONS NOW AVAILABLE FOR LICENSING

NIST recently announced that the following 10 government-owned inventions are now available for licensing:

- Device and Method for Detection of Compounds Which Intercalate with Nucleic Acids;
- Multiple Memory Self-Organizing Pattern Recognition Network;
- Planar Epitaxial Films of SnO₂;
- Frequency Calibration Standard Using a Wide Band Phase Modulator;
- Nanocomposite Material for Magnetic Refrigeration and Superparamagnetic Systems Using the Same;
- Nitrogenated Metal Alloys Via Gas Atomization;
- Process for the Controlled Preparation of a Composite of Ultrafine Magnetic Particles Homogeneously Dispersed in a Dielectric Matrix;
- Methods of Making and Using Improved Microporous Hollow Fibers, the Improved Hollow Fibers, and Tube Bundles Constructed of the Improved Fibers;
- Diamond-Coated Laminates and Method of Producing Same; and
- Neutron-Absorbing Glass Compositions.

For technical and licensing information on these inventions, contact Bruce E. Mattson, B256 Physics Building, NIST, Gaithersburg, MD 20899, 301/975-3084.

NIST TRAINS USDA QUALITY CONTROL OFFICIALS

The Weights and Measures Program of NIST presented a seminar on Scale Inspection and Testing for officials of the U.S. Department of Agriculture's (USDA) Food Safety and Inspection Service at the Maryland Weights and Measures Laboratory in Annapolis, MD.

The class was presented by NIST to prepare USDA personnel for implementation of new regulations on March 2. These regulations, for the first time, require scales in 12000 meat and poultry plants across the United States and abroad to conform to NIST Handbook 44—Specifications, Tolerances, and Other Technical Requirements for Weighing and Measuring Devices. This action represents a major step towards uniformity in federal and state weights and measures requirements and will provide a higher level of economic protection for purchasers of federally regulated meat and poultry products.

NIST has supported, and continues to provide support to, USDA during the implementation of these important new regulations. To date this support has included:

- development of a field manual on package inspection for use by USDA inspectors in meat and poultry plants (based on NIST Handbook 133, Checking the Net Contents of Packaged Goods);
- surveying the ability of states to respond to requests for technical assistance and contacting states where potential problems have been identified to ensure that scale certification is provided;
- offering guidance to states to help them provide scale certification through voluntary registration programs for service agencies and technicians;
- technical guidance and assistance in responding to inquiries from industry; and
- training in package inspection and device testing procedures.

NIST STAFF DEMONSTRATES 800-FOLD IMPROVEMENT IN OPTICAL FIBER CURRENT SENSOR

NIST scientists recently achieved a new record for minimum detectable current in an optical fiber current sensor and reported the results at the 8th International Optical Fiber Sensor Conference held earlier this year. They measured the minimum

detectable current in their sensor to be 220 nA in a 1 Hz bandwidth. The previous record of 180 μ A in a 1 Hz bandwidth also was held by NIST and reported by a NIST scientist some years ago. The new NIST sensor is based on the Faraday effect in gallium-doped yttrium iron garnet (Ga:YIG), selected by the team as a result of intensive analysis of candidate materials. This material exhibits a much stronger Faraday effect than others, making it inherently possible to measure smaller currents. However, Ga:YIG is not available in large enough pieces that a single sensing element would suffice, and the design accordingly uses four small rods of the material incorporated into an optical path which encloses the conductor.

NIST DEVELOPMENTS PROVIDE IMPETUS FOR TWO START-UPS

Two small entrepreneurial companies have been formed recently as a result of NIST developments in electromagnetic compatibility and electromagnetic interference. In the first instance, a Washington, DC company was established to build standard electric field radiators of NIST design as a result of additional requests for the device from industry that NIST could not meet. Earlier, NIST had supplied several devices to a computer company that had co-sponsored the development, but considerably more were needed.

As a known source of electric field over a frequency range of 30 to 1000 MHz, the NIST standard radiator in the form of a remotely controlled radiating spherical dipole is used in conjunction with an electromagnetic test facility, such as a shielded room or open test site (ground-plane range), to determine the performance of field-measuring instrumentation used in conjunction with the facility. Companies need calibrated field measurements to be sure that tests of products such as computers reliably demonstrate compliance with emissions regulations promulgated by the Federal Communications Commission.

In the second instance, an engineer in the company that provided NIST the thin-film fabrication technology for a broadband 8 mm electric field probe subsequently formed a Denver company to produce it. This became the third U.S. commercialization of the NIST device. The probe uses the principle of a resistively tailored dipole structure to achieve an isotropic response of better than ± 0.3 dB from 100 kHz to 18 GHz and ± 0.2 dB from 1 MHz to 15 GHz for fields between 1 and 1600 V/m.

LASER-ABLATED HIGH-CRITICAL-TEMPERATURE SUPERCONDUCTOR FILMS STUDIED

Using scanning electron and scanning tunneling microscopies, a team of NIST scientists has examined the relationship between deposition parameters and morphology of laser-ablated yttrium-barium-copper oxide films (formula: $\text{YBa}_2\text{Cu}_3\text{O}_{7-\delta}$, where $0 \leq \delta \leq 1$). The work is motivated by the need to understand and control the topography of films of high-critical-temperature superconductors used in practical devices. Because of the extremely short coherence lengths of these superconductors, films made from them must be smooth on a nanometer scale. An additional concern is that surface roughness may increase the difficulty of growing continuous films and lead to micro short-circuits in layered structures.

NIST scientists have studied the morphologies of films deposited under a variety of conditions. They found that the deposition rate appears to determine the film-growth mechanism: in films deposited at relatively fast rates on MgO, they observe island nucleation and growth, while they found screw dislocation growth in films deposited at lower rates. The team also found that substrate temperature during deposition controls the density of the islands that nucleate. More islands nucleate at lower temperatures and, consequently, they are smaller in size than the islands in films grown at higher temperatures. A third finding is that the partial pressure of oxygen during deposition influences the roughness of the films. Smoother films were found to develop under lower oxygen pressures, but these films have the drawback of depressed transition temperatures. The NIST team is collaborating with a group at MIT producing $\text{Bi}_2\text{Sr}_2\text{CaCu}_2\text{O}_{8+\delta}$ films and a group at Stanford producing a-axis $\text{YBa}_2\text{Cu}_3\text{O}_{7-\delta}$ films.

LONGEST RANGE SCANNING TUNNELING MICROSCOPE DEVELOPED

NIST scientists have developed a scanning tunneling microscope (STM) for profiling surfaces with a wide lateral dynamic range. It can zoom from a field of view of 600 μm to a resolution limit of about 1 nm. Therefore, the overall lateral dynamic range is 600000:1. The 600 μm field of view is a world record for long-range scanning with STMs. The instrument combines a commercial STM probe, which has atomic resolution, with a precise piezoelectric motion system for achieving the wide field of view. The instrument has two scanning stages to achieve the lateral dynamic range, the

piezoelectric stack scanner in the base for the long-range mode and the STM tube scanner in the sensor head for the high-resolution mode. The lateral resolution of the system in this mode is vibration limited and is approximately 1 nm. The system operates in air and will soon be enhanced with an atomic force sensor so that insulating surfaces can be inspected as well as electrical conductors. The scientists developed the long-range STM for high-resolution profiling of optical surfaces. It also will be used to test the surface finish of x-ray optics. An article on the long-range STM was published in the April 1992 issue of Review of Scientific Instruments.

WORKSHOP ON SUPERCRITICAL FLUID EXTRACTION HELD AT NIST

Supercritical fluid extraction (SFE) is a promising new technology for the rapid, automatable preparation of samples for analytical measurement. To evaluate the state of the art for this new technique, a 1 day workshop was held recently at NIST. The 50 workshop attendees included experts from academia, instrument companies, private industrial user labs, environmental contract labs, EPA, and NIST. The meeting focused on ways of using SFE to improve measurements associated with the environmental problem of leaking fuel storage and delivery tanks.

In the months prior to the meeting, NIST provided four unknown soil-type samples, as well as instrument calibration solutions, to potential workshop attendees who had agreed to participate in a round robin. Although no SFE conditions were specified for this round robin, a consensus was achieved that confirmed the optimum operating parameters arrived at as a result of NIST research.

The results of the round-robin study and extensive discussions among the participants at the workshop confirmed that SFE is a promising new technology for the rapid, routine analysis of aliphatic hydrocarbons from fuel-contaminated soil. However, more research will be needed to extend the application of SFE to more polar classes of contaminants and/or other sample types.

AUTOMATED CALIBRATION SYSTEM FOR AIR FLOW-RATE CALIBRATIONS

A NIST scientist recently completed the development of an automated data acquisition and control software package for routine air flow-rate calibrations performed at NIST. These calibrations are done using piston or bell "provers," which are accurately calibrated instruments providing direct

measurement of the quantity of displaced fluid. The algorithm, called AIR, written for an IBM compatible-PC using Turbo Pascal 6.0, is highlighted by the use of a graphical user interface, automation of most measurements, real-time data display, and a data throughput of one measurement cycle per second. The user-friendly package is expected to improve the current measurement precision of air flow-rate calibrations up to 0.05 m³/s. This improvement of as much as a factor of two is due to increased data throughput and the ability of the operator to maintain steady-state conditions in the prover by monitoring measurement data in real time. Similar algorithms could be implemented in other primary-calibration facilities. Future plans call for implementation of such techniques to encompass the full range of air flow-rate calibrations at NIST (up to 1.4 m³/s) and to upgrade the current water-flow automated calibration system. The beneficiaries of this development include the aerospace, petrochemical, and electronics instrumentation industries.

MAGNETIC ENGINEERING OF THIN FILMS

The recent discovery of the "giant magnetoresistance (GMR) effect" in magnetic multilayers has stimulated much interest in the antiferromagnetic coupling between magnetic layers, which is associated with the GMR effect. This effect could serve as the basis for producing new, improved non-volatile memory chips, critical to the personal computer industry. Thin films containing layers of cobalt and copper exhibit the largest GMR effect found to date. Selected samples were studied at NIST and found to be nearly polycrystalline (made up of many crystallites). This surprising result raised the question of which crystallite was most important in determining the observed physical properties. Accordingly, several different single-crystal cobalt-copper multilayers were produced and studied. These studies indicated that the (100) crystallites are responsible for the antiferromagnetic coupling. This conclusion suggests that controlling the (100) crystallite concentration in these multilayers will be a way to control the antiferromagnetic coupling and, thus, to engineer the desired values of the antiferromagnetic coupling strength for thin-film device applications.

NIST HOLDS WORKSHOP ON NVLAP IONIZING RADIATION PERSONNEL DOSIMETRY PROGRAM

On March 6, the Ionizing Radiation Division held a workshop to evaluate the impact on NIST pro-

grams of the proposed ANSI N13.11, an update on criteria for testing and performance of personnel dosimeters. The National Voluntary Laboratory Accreditation Program (NVLAP) Personnel Radiation Dosimetry Program, initiated in 1984, provides the basis for the traceability to NIST and national standards for badge dosimeters for 1.3 million U.S. workers in medical, military, and industrial radiation applications. NIST, at the top of the technical hierarchy, provides traceability for dosimetry to the processing community through Battelle Pacific Northwest Laboratories (PNL), which acts under contract to NVLAP. The workshop was attended by representatives of the U.S. Nuclear Regulatory Commission, the Department of Energy, members of the ANSI N13.11 standards-writing subcommittee, Battelle PNL, dosimetry processors, dosimetry users, and NVLAP and NIST technical experts.

GRAVITY ATTRACTS FEDERAL LAB CONSORTIUM FLC AWARD

The FLC is an organization of more than 500 U.S. government laboratories and research centers. Every year it gives up to 30 awards to recognize excellence in technology transfer. This year NIST received two of the awards. One of them was given to a NIST scientist for transferring to industry fundamental optical, electronic, and mechanical technology for the production of instruments for the ultra-precise and absolute measurement of gravity. The scientist's work resulted in not only the transfer of a particular technology but also the creation of a new U.S. industrial firm, AXIS Instruments Co. of Boulder, CO, which specializes in the design and manufacture of high-precision scientific instruments. The scientist has pioneered the development of absolute gravimeters for making fundamental measurements; six of his instruments are being used around the world to detect motions of the Earth's crust and subsurface density changes. Determining the Earth's gravity to the precision of which these instruments are capable—parts per billion—permits measurements of local height relative to the center of the Earth to better than 1 cm! The first two of the new and improved generation of gravity instruments being manufactured by AXIS for NIST will be transferred to NOAA for application in its Global Climate Change Program. They will be used to estimate the range of change of global absolute sea level, and thus to help evaluate models of global warming.

NIST PROJECT EARNS NASA COMMITTEE'S TOP PRIORITY

Almost everything known about the universe is based on the detection and analysis of electromagnetic radiation. The detection of gravitational waves would open an entirely new window on the universe, permitting searches for signals such as gravitational-wave bursts from neutron stars spiraling into supermassive black holes at vast distances. NASA formed the Ad Hoc Committee on Gravitational Physics and Astronomy in 1989 and charged it with identifying "the most important gravitational experiments [in space] that could be carried out within the next twenty years," and distilling "a (prioritized) list of generic technologies that need development." The committee's just-released report summarizes seven proposed scientific measurements and associated technologies, and rates technology development for a space-based gravitational-wave observatory first priority. The observatory could be a laser interferometer with arms $\sim 10^7$ km long orbiting the sun. In the most interesting low-frequency band, not accessible to Earth-based observatories, the goal is to measure changes in the arm lengths to a precision of about one part in 10^{20} in 1 s.

NIST scientists have been working for several years with colleagues at the University of Colorado, and more recently the Jet Propulsion Laboratory, on the conceptual design and error budget for such an observatory. It will take quite exquisite technology, some of it with possible terrestrial applications, including the development of disturbance reduction systems; low-expansion thermal insulation; spacecraft monitoring and control systems; a high-efficiency, long-lifetime laser; and an extremely precise laser-beam steering system.

PATENT ON THE "SHARPEST" STM TIP EVER

Research teams worldwide are racing to improve the potential of the scanning tunneling microscope (STM) for producing ever-smaller semiconductor devices and computer-memory elements. The goal is controlled "nanolithography" of features smaller than 10 nm, and eventually the size of individual atoms. The potential economic impact is enormous, as the structures that are now produced routinely have dimensions of hundreds of nanometers and are normally formed by optical "lithography," i.e., writing fine lines or spots with light. The STM is an attractive new tool for this because it produces a concentrated high electric field when its conducting tip is brought close to a surface, resulting in a

highly localized beam of low-energy electrons. These can stimulate molecules from the surrounding gas to etch or deposit on the surface (a.k.a., chemical vapor deposition, or CVD). The problem is that an STM probe placed close enough (≤ 0.5 nm) to the surface to generate the necessary field leaves precious little space for CVD molecules to diffuse through the gap between probe and sample. Moving the probe back to permit their passage spreads the field and electron beam over a much larger region of the sample, at great cost in resolution. A NIST scientist has just received a patent on the design of a probe end that produces a much "sharper" electron beam spot on the sample with the probe end far enough away from the surface to allow access of the CVD molecules to the desired region. This allows very precise control, essentially single-atom positioning, of reactions with the sample surface.

EXPERT SYSTEM MODULES FOR CHEMICAL PROCESS INDUSTRIES RELEASED

The NACE-NIST Corrosion Data Program, a joint activity of NIST and the National Association of Corrosion Engineers, recently released two more expert system modules in the CHEM•COR series. The CHEM•COR series is a series of personal computer programs designed to provide materials selection and usage advice to chemical process plant managers on the handling and storage of industrial corrosives, primarily hazardous chemicals. The two new modules on hydrogen chloride and chlorine combine with the previously released modules on concentrated sulfuric acid, acetic acid, and formic acid to make up the CHEM•COR series. The NACE-NIST Corrosion Data Program, with the sponsorship of the Materials Technology Institute of the Chemical Process Industries, plans 11 modules for this series.

NIST EXPANDS MICROELECTRONICS PACKAGING EFFORTS

In 1992, NIST expanded its efforts in the area of microelectronics packaging, the structures that connect modern microchips to and protect them from the outside world. Several recent studies have identified the packaging as the component most apt to limit the performance of future microelectronic systems. These new efforts expand upon packaging related work of long standing at NIST on wire bonding and thermal control by NIST scientists.

The expanded NIST efforts primarily concentrate on development or refinement of metrology of the properties of the materials in packaging, preferably in situ and at the micrometer scale, for use in research, design, manufacturing, product quality control, and failure analysis. The efforts are in partial response to needs, desires, and opportunities identified in a NIST workshop in May 1990. NIST efforts include: exploring various approaches such as fluorescence for determining the degree of cure of polymers; attempting to develop a new understanding of the material parameters affecting solderability, i.e., the ability to attach components via solder; developing techniques and procedures for measuring the separate strengths of adherends; exploring the possibility of actually embedding thin film thermocouples in the bodies of the packaging to make direct measurements of the internal temperatures without having to rely on predicted values.

ANIMATION PROGRAM FOR PROCESS SIMULATION

A NIST scientist has developed an animation program that displays interactively the results of his process simulation programs for polymer composite fabrication. The animation program shows the mold filling patterns during liquid molding and displays the resulting pressure distributions. The information is used to optimize mold design and processing parameters. For example, the location of resin injection ports can be changed to ensure that the flow does not prematurely close off regions, thus causing voids, or that flow fronts do not merge to create weak regions in critical places.

The first application of this program was the analysis of simulation results for mold filling of a demonstration part being made by the Automotive Composites Consortium (ACC). The ACC was formed to conduct pre-competitive research promoting the use of polymer composites in structural automotive applications. NIST is cooperating with the ACC by conducting process simulation studies for their demonstration part. In early March, the NIST scientist toured all three ACC members' plants to demonstrate the results of the simulation using the animation program. Representatives of the ACC found the simulations extremely useful and described the animation as a major advance over the alternative methods to study simulation results.

FIRST STATION FOR COLD NEUTRON INELASTIC SCATTERING OPERATIONAL AT NIST

The medium resolution time-of-flight spectrometer, the first of a number of experimental stations at NIST dedicated to inelastic neutron scattering research on materials, became operational in February. This highly flexible instrument, which contains over 100 neutron detectors at 10°-120° scattering angles and a focusing monochromator, allows the investigation of atomic and molecular motions and excitations over a wide range of time and energy in systems as diverse as magnetic materials, catalysts and microporous materials, fullerenes, polymers, and biological molecules. Test experiments already have been carried out studying hardening processes in cements, dynamics of small organic molecules bound in zeolites, and anomalous local diffusion of hydrogen in rare earth metals. This time-of-flight spectrometer, along with five other inelastic scattering stations under development at NIST, will provide U.S. researchers with internationally competitive facilities for the study of low-energy excitations and slow dynamic processes in condensed matter, which are often a key to the properties of chemical, biological, and high-technology materials.

NIST SQL TEST SUITE, VERSION 3.0, RELEASED

On Jan. 2, NIST released NIST SQL Test Suite, Version 3.0, to test conformance to Federal Information Processing Standard (FIPS) 127-1, Database Language SQL. Version 3.0 contains new test cases and includes additional test suites for Embedded Ada and Module Language Ada. The new test cases also are included in the existing embedded and module language test suite types (C, COBOL, FORTRAN, and Pascal) as well as the Interactive SQL test suite.

Use of Version 3.0 of the NIST SQL Test Suite will be required for validation of products after July 1. Certificates will be issued after Jan. 1, 1993, for conforming SQL implementations without deficiencies. Tested implementations will be listed in the Validated Products List, which NIST publishes quarterly as an NISTIR. Government agencies can use this information to confirm that SQL implementations conform to FIPS 127-1.

**PROFESSIONAL/TRADE ORGANIZATION
LABORATORY ACCREDITATION/
DESIGNATION PROGRAMS**

NIST has published a guide to U.S. private-sector laboratory accreditation/designation programs. NIST SP 831, Directory of Professional/Trade Organization Laboratory Accreditation/Designation Programs, provides information on 48 laboratory accreditation and similar programs operated by U.S. private-sector professional and trade organizations. These programs encompass assessments of laboratory capability, designating those entities that are judged to be competent to conduct specific tests or types of testing. Entries in this directory are based primarily on information provided by the organization and reflect the organization's view of its activities. Companion documents in this area are NIST SP 808, Directory of Federal Government Laboratory Accreditation/Designation Programs, and NISTIR 4576, Laboratory Accreditation in the United States, which provide information on similar programs operated at the federal, state, and local government levels and an introductory explanation of the subject of laboratory accreditation.

**NIST HOSTS AND SPONSORS 5TH NATIONAL
CONSORTIUM FOR SPECIALIZED
SECONDARY SCHOOLS OF MATHEMATICS,
SCIENCE, AND TECHNOLOGY**

On March 19-21, NIST was the site for the 5th Annual Conference of the National Consortium for Specialized Secondary Schools of Mathematics, Science, and Technology. Sponsored by NIST and the Montgomery County, MD, Science, Mathematics, and Computer Science Program at Blair High School, the conference attracted approximately 200 teachers from specialized schools around the United States. The meeting began with pre-conference hands-on workshops for the teachers. Five of the workshops were held at NIST: Techniques in Computational Chemistry, Physics, Technology and Superconductors, Scanning Tunneling Microscope Training, and Making Good Use of Networks. Conference sessions were held March 20-21 on such topics as Making Connections between Disciplines; Nontraditional Evaluation Techniques; Product Design Engineering; Group Learning Projects; Telelearning; Gifted and Talented Underachievers; Cooperative Learning in Mathematics; Successful Integration of English, Biology and Technology; and Can Ethics in Science Be Taught? NIST Director John Lyons gave the opening remarks to the conference.

The consortium was formed in April 1988 to meet the needs of educators and students in the growing number of specialized high schools. Its goal is to foster, support, and advance the efforts of those specialized schools whose primary purpose is to attract and prepare students academically for leadership in mathematics, science, and technology.

**UPDATE OF THE NIST/EPA/NIH MASS
SPECTRAL DATABASE COMPLETED**

The NIST Mass Spectrometry Data Center has announced the May 1 release of a major update of the large Mass Spectral Database. The name of this improved database, the NIST/EPA/NIH Mass Spectral Database, emphasizes the inclusion of hundreds of new original spectra determined specifically for the database at NIH. Thousands of copies of this database are used in the data systems of commercial mass spectrometers and in a PC version developed by a NIST scientist.

The update incorporates 8500 new spectra, bringing the total number of compounds represented in the collection to 62500. Many of the new spectra have been acquired by deliberately targeting compounds that are relevant to real-life analyses and acquiring spectra of those compounds through directed determinations or acquisition of special collections.

For the first time, the database is also available in an expanded version, which includes 12500 critically evaluated replicate spectra. Given the known variability of mass spectra, providing replicate spectra can increase the probability of identifying unknown spectra during a library search. The expanded collection has a total of 75000 spectra.

Since the last update in 1990, a large fraction of the spectra in the database have been evaluated manually in an effort to correct or eliminate all poor quality spectra.

The new release of the PC version also includes several new features, including new searching/matching schemes for identifying spectra of unknown chemical compounds.

**UPDATE OF CHEMICAL KINETICS DATABASE
RELEASED**

Version 4.0 of the personal computer Chemical Kinetics Database was released for distribution to the public on April 9. The database, produced and maintained by NIST now includes data on 6900 chemical reactions, with more than 20000 individual data entries. This database is an important tool for modeling combustion systems or chemical

processes occurring in the atmosphere. The data in this database are necessary, for example, in predicting the atmospheric lifetimes of chemicals that may impact on the depletion of the Earth's ozone layer.

This software was designed by a NIST scientist and includes an option that allows users to graphically display plots of rate constants as a function of temperature. These graphs of data from different sources are useful for identifying discrepancies in experimental determinations. The new release includes a major new feature that allows the user to search the database to locate all reactions which result in the formation of a particular chemical product.

NEW ITS-90 BASED DATA FOR THERMOCOUPLES

An international collaborative effort involving national laboratories from eight countries (United States, United Kingdom, The Netherlands, Russia, Korea, Japan, Italy, and China) has produced new data on the electromotive force (emf) of type S thermocouples as a function of temperature on the International Temperature Scale of 1990 (ITS-90). These data were used in deriving a new reference function from -50 to 1768.1 °C (the melting-point temperature of platinum). Also, they were used to compute the differences in temperatures on the ITS-90 and the International Practical Temperature Scale of 1968 (IPTS-68) for the range 630 to 1064 °C. The new estimate of the temperature differences between the scales differs from previously published values by as much as 0.3 at 760 °C. These differences, however, do not in any way affect the definition of the ITS-90.

In addition to measurements on type S thermocouples, NIST and NPL (UK) obtained data on type R and type B thermocouples. NIST scientists made measurements, consulted on the design of the NIST experiment, and analyzed the data of the eight laboratories. Results of these experiments were presented at the 7th International Symposium on Temperature held in Toronto, Canada, April 28-May 1. The new reference function for the type S thermocouples and the new estimate of the differences between temperatures on the ITS-90 and the IPTS-68 will allow reference functions and tables for all ISA letter-designated thermocouples to be incorporated into voluntary standards (e.g., ASTM, ISA, and IEC) for science and industry.

COUNCIL ON IONIZING RADIATION MEASUREMENTS AND STANDARDS (CIRMS) IS ESTABLISHED

Following an organizational meeting at NIST in 1991, and the election of officers early this year, the organizing committee and officers met at NIST on March 31, to establish the Council on Ionizing Radiation Measurements and Standards (CIRMS). The organization represents tens of thousands of users of ionizing radiation engaged in industrial radiation processing, radiation therapy and diagnostics, and radiation protection and control. CIRMS will provide a forum for discussing national ionizing radiation measurement and standards problems, defining and prioritizing needed work in ionizing radiation measurements and standards, disseminating information on written standards, and organizing workshops to advance ionizing radiation technology.

INITIAL OBSERVATIONS OF IML-1 TRIGLYCINE SULFATE CRYSTAL

The first detailed examinations of the triglycine sulfate crystal grown on International Microgravity Laboratory-1, the February space shuttle flight, have now taken place. Diffraction imaging has been carried out on the high-resolution beam line at the National Synchrotron Light Source at Brookhaven National Laboratory.

Initial imaging determined the regularity of the space-grown crystal before it was cut into pieces for infrared detector fabrication and other analysis, procedures that prior work had shown might affect the crystal regularity. Subsequent images of the cut edge of the crystal were then taken to provide information on the extent and nature of the space growth and its relation to the ground-grown seed.

Initial analysis of video data collected indicates that the local acceptance angle for this crystal for highly collimated, monochromatic 8-10 keV x rays is 1-2 arc seconds. This critical measure of crystal regularity is substantially better than that for the best silicon crystals, which are among the most regular crystals known.

NIST ESTABLISHES MEMORANDUM OF UNDERSTANDING (MOU) WITH THE COMMUNICATIONS SECURITY ESTABLISHMENT OF CANADA

In March 1992, NIST and the Canadian Communications Security Establishment established an MOU to pursue technical cooperation in information

security (INFOSEC). The MOU provides a framework for the two governments to facilitate the coordination and development of INFOSEC standards and criteria for the protection of sensitive unclassified data. It also establishes mutual recognition of validation testing and product endorsements performed by either government to ensure compliance with mutually agreed standards and criteria. Forms of cooperation may consist of exchanges of technical information, exchange visits, and other forms of collaborative activities.

NEW PUBLICATION DESCRIBES REFERENCE MODEL (RM) FOR SOFTWARE ENGINEERING ENVIRONMENT (SEE) FRAMEWORKS

Reference Model for Frameworks of Software Engineering Environments (NIST SP 500-201), characterizes an SEE frameworks RM as a conceptual basis for describing and comparing existing SEEs and their components. An SEE deals with information about the software under development, such as specifications and design data, and project resources, such as costs and computer resources. The document was prepared jointly by NIST and the European Computer Manufacturers Association.

Standard Reference Materials

STANDARD REFERENCE MATERIALS 2534 AND 2535—ELLIPSOMETRIC PARAMETERS, Δ AND Ψ , AND DERIVED THICKNESSES AND REFRACTIVE INDEX FOR A SILICON DIOXIDE LAYER ON SILICON

NIST announces the availability of Standard Reference Materials (SRMs) 2534 (25 nm SiO₂) and 2535 (12 nm SiO₂), certified for Δ and Ψ at the vacuum wavelength of $\lambda = 633$ nm using the NIST high-accuracy ellipsometer. They are intended primarily to evaluate the accuracy of ellipsometers but also may be used as an aid in the calibration of other optical thickness-monitoring instruments.

Each SRM unit, consisting of a 77 mm diameter silicon wafer on which a uniform silicon dioxide layer has been grown, is individually certified and bears an identifying serial number. SRMs 2534 and 2535 are the latest additions to the ellipsometric standard series composed of SRMs 2531-2535.

STANDARD REFERENCE MATERIAL 473—OPTICAL MICROSCOPE LINEWIDTH MEASUREMENT STANDARD

NIST announces the availability of Standard Reference Material (SRM) 473, Optical Microscope Linewidth Measurement Standard. SRM 473 is intended for use in measuring linewidths for antireflecting-chromium integrated-circuit photomasks. It consists of patterns of clear and opaque lines with nominal dimensions ranging from 0.5 to 30.0 μm and with line-spacing (pitch) patterns ranging from 2 to 70 μm . These patterns are on a nominal 127 \times 127 \times 2.3 mm quartz substrate. Certified values are given for the clear and opaque linewidths and the center-to-center spacings for one of the eight repeated patterns on the SRM. Each SRM 473 unit is individually certified and bears an identifying serial number.

STANDARD REFERENCE MATERIAL 968a—FAT-SOLUBLE VITAMINS IN HUMAN SERUM

NIST announces the availability of the renewal issue of Fat-Soluble Vitamins in Human Serum Standard Reference Material (SRM) 968a. This SRM is intended for use in validating methods for determining retinol, α -tocopherol, and total β -carotene in human serum and plasma. It also can be used for assigning values to in-house control materials. A unit of SRM 968a consists of six vials, two at each of three concentration levels, of lyophilized human serum. Each vial is to be reconstituted with 1.00 mL of HPLC-quality water.

In addition to certified values for retinol, γ -tocopherol and total (trans plus cis isomer) β -carotene, information values are provided for cholesterol, α -tocopherol, all trans β -carotene, α -carotene, β -cryptoxanthin, lutein, lycopene, and zeaxanthin.

Standard Reference Data

1992 SRD PRODUCTS CATALOG AVAILABLE

The NIST Standard Reference Data Products Catalog 1992, Reliable Evaluated Data for Global Problems (NIST Special Publication 782) provides scientists and engineers with the latest information on more than 65 evaluated data publications and computerized databases available from the NIST Standard Reference Data Program (SRDP) and other sources. For more than 28 years, critically evaluated data have been used to improve design efficiency of chemical processes, identify potential toxic substances in the environment, improve materials durability, and calculate performance of chemical reactors. Data compilations are available in the following areas: analytical chemistry, atomic physics, biotechnology, chemical kinetics, materials properties, molecular structure and spectroscopy, thermodynamics and thermochemistry, thermo-physical properties of fluids, as well as special databases of binary images and structured forms. To obtain a copy of SP 782, send a self-addressed mailing label to SRDP, A320 Physics Building, NIST, Gaithersburg, MD 20899, 301/975-2208.

EIGHT REFRIGERANTS ADDED TO REFPROP DATABASE

A widely used personal computer database for evaluating the performance of alternate refrigerants and refrigerant mixtures now has eight new entries. The Thermodynamic Properties of Refrigerants and Refrigerant Mixtures Database (REFPROP) is an important research tool for refrigeration engineers, chemical and equipment manufacturers, and others looking to replace chlorofluorocarbon and hydrochlorofluorocarbon materials with environmentally acceptable fluids. Version 3.0 of REFPROP can produce tables of the thermodynamic and transport properties of 26 pure refrigerants and refrigerant mixtures with as many as five components. Version 3.0 of REFPROP is available for \$390; owners of a previous version may upgrade for \$100. To order NIST Standard Reference Database 23, REFPROP, contact the Standard Reference Data Program, A320 Physics Building, NIST, Gaithersburg, MD 20899, 301/975-2208, fax: 301/926-0416.

NEW GAS PHASE INFRARED DATABASE AVAILABLE FOR PCs

The infrared absorption spectra of more than 5,300 chemical compounds are in the new NIST/EPA Gas Phase Infrared Database. The database will be particularly helpful for analytical chemists and environmental scientists who employ infrared spectroscopy to identify unknown substances. It is a collection of gas-phase Fourier transform infrared (FT-IR) absorption spectra compiled by NIST in collaboration with the Environmental Protection Agency (EPA). The database was assembled from an archive of 3300 spectra acquired by EPA and approximately 3000 spectra measured at NIST. It has software very similar to the widely used NIST/EPA/NIH Mass Spectral Database. The two databases, mass spectra (MS) and infrared spectra (IR), can potentially be combined for use in so-called "hyphenated" MS-IR instruments. The NIST/EPA Gas Phase Infrared Database, Version 1.0, is available for \$415. It requires MS DOS 2.1 or later, 640K memory, and a color monitor. The database can be ordered from the Standard Reference Data Program, A320 Physics Building, NIST, Gaithersburg, MD 20899, 301/975-2208, fax: 301/926-0416.

NIST BINARY IMAGES OF HANDWRITTEN SEGMENTED CHARACTERS

NIST Special Database 3 is now available from the Standard Reference Data Program. A valuable tool for training recognition systems on a large statistical sample of hand-printed characters, the database consists of over 313000 isolated character images. Of these images, 223125 are digits; 44951 are upper-case; and 45313 are lower-case character images. Each character image has been centered in a separate 128 by 128 pixel region and has been assigned a classification which has been manually corrected so that the error rate of the segmentation and assigned classification is less than 0.1 percent. The database comes in a CD-ROM format and includes image format documentation and example software.

Calendar

July 13-17, 1992

WORKSHOP ON EXPERIMENT DESIGN FOR SCIENTISTS AND ENGINEERS

Location: National Institute of
Standards and Technology
Boulder, CO

Purpose: To discuss and explore the fundamental principles and techniques of efficient experiment design.

Topics: Improving quality and productivity, the role of experiment design, general design problems, designs to assess the effect of an engineering modification, designs to assess and estimate parameter interactions, designs for ferreting out dominant parameters, designs for finding optimal operating conditions, Taguchi-contributions and cautions.

Format: Workshop session/lab.

Audience: Scientists and engineers involved in research and development or manufacturing with a goal of improving quality and productivity.

Sponsor: NIST.

Contact: Eric Lagergren, NIST, A337 Administration Building, Gaithersburg, MD 20899, 301/975-3245.

September 14-17, 1992

4th INTERNATIONAL COLLOQUIUM ON ATOMIC SPECTRA AND OSCILLATOR STRENGTHS FOR ASTROPHYSICAL AND LABORATORY PLASMAS

Location: National Institute of
Standards and Technology
Gaithersburg, MD

Purpose: To bring together users and producers of atomic data in plasma physics to determine needs and useful directions for research.

Topics: Astrophysical data needs, atomic energy levels, wavelengths, ionization energies, lifetimes and transition probabilities, line shapes and splittings, laboratory sources, atomic databases.

Format: General sessions, poster sessions, and a special session in which the major atomic data needs for future space and laboratory programs will be discussed.

Audience: Atomic spectroscopists, astronomers, and laboratory plasma researchers.

Sponsors: NIST, National Aeronautics and Space Administration, Department of Energy, Naval Research Laboratory.

Contact: Jack Sugar, A167 Physics Building, NIST, Gaithersburg, MD 20899, 301/975-3218.

September 15-17, 1992

SYMPOSIUM ON OPTICAL FIBER MEASUREMENTS

Location: National Institute of
Standards and Technology
Boulder, CO

Purpose: To provide a forum for reporting the results of recent measurement research and an opportunity for discussions that can lead to further progress.

Topics: Measurements on fibers, related components, and systems; field and laboratory instrumentation; and standards.

Format: Symposium with contributed and invited papers.

Audience: Scientists and engineers.

Sponsors: NIST, IEEE Lasers and Electro-Optics Society, and the Optical Society of America.

Contact: Douglas Franzen, Div. 814.02, NIST, Boulder, CO 80303, 303/497-3346.

October 28-30, 1992
**SYMPOSIUM ON
OPTICAL MATERIALS
FOR HIGH-POWER LASERS**

Location: National Institute of
Standards and Technology
Boulder, CO

Purpose: To exchange information on the technology and physics of materials for high-energy/high-power lasers.

Topics: New materials, bulk damage phenomena, surface and thin film damage, preparation of optical materials/surfaces and measurements of their properties, design considerations for high-power output systems and fundamental mechanisms of laser-induced damage, and laser interaction with optical materials.

Format: Symposium.

Audience: Industry, government agencies, and academia.

Sponsors: NIST; Center for Research in Electro-Optics and Lasers, University of Central Florida; Department of Energy; Department of Defense; and ASTM.

Contact: Donna Wilson, University of Central Florida, 12424 Research Parkway, Suite 400, Orlando, Fla. 32826, 407/658-6834.

June 27-July 1, 1994
**CONFERENCE ON
PRECISION ELECTROMAGNETIC
MEASUREMENTS—CPEM '94**

Location: Clarion Harvest House Hotel
Boulder, CO

Purpose: To exchange information on a wide range of problems in the area of precise electromagnetic measurements. A number of special sessions on the fundamental constants will be held in anticipation of a new adjustment of the constants scheduled for 1995.

Topics: Direct current and low-frequency measurements; fundamental constants and special standards; time and frequency; rf, microwave, and millimeter-wave measurements; lasers, optical fibers, and optical electronics; superconducting and other low-temperature systems; dielectrics and antennas; automated measurement methods; and advanced instrumentation, including new sensors and novel measurement methods.

Format: General sessions, plenary sessions, and poster sessions.

Audience: Industry, government agencies, and academia. Emphasis is on standards activities and measurement methods.

Sponsors: NIST, IEEE Instrumentation and Measurement Society, Union Radio Scientifique Internationale.

Contact: Donald B. Sullivan, Div. 847, NIST, Boulder, CO 80303, 303/497-3772.